Modeling storm effects on sand wave dynamics

UNIVERSITY OF TWENTE.

G.H.P. Campmans

August 31, 2018

Graduation committee:

prof.dr.ir. G.P.M.R. Dewulf	University of Twente, chairman and secretary
prof.dr. S.J.M.H. Hulscher	University of Twente, supervisor
dr.ir. P.C. Roos	University of Twente, co-supervisor
dr.ir. D. Calvete	Universitat Politècnica de Catalunya, referee
em.prof.dr.ir. H.J. de Vriend	University of Twente, referee
dr.ir. R. Hagmeijer	University of Twente
prof.dr. D. van der Wal	University of Twente
prof.dr. V. van Lancker	Ghent University & Royal Belgian Institute of Natural Sciences
prof.dr. H.E. de Swart	Utrecht University
prof.dr.ir. M. van Koningsveld	Delft University of Technology

presented research in this thesis is carried out at the Water Engineering and Management (WEM) department, Civil Engineering, University of Twente, The Netherlands.

This work is part of the research programme SMARTSEA with project number 13275, which is (partly) financed by the Netherlands Organisation for Scientific Research (NWO).

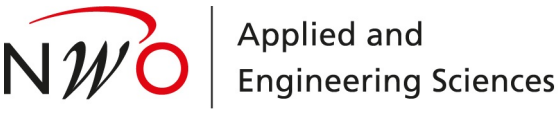

ISBN 978-90-365-4600-3
DOI: 10.3990/1.9789036546003
Cover: Model simulation by G.H.P. Campmans
Printed by: Gildeprint, Enschede.

MODELING STORM EFFECTS ON SAND WAVE DYNAMICS

DISSERTATION

to obtain
the degree of doctor at the University of Twente,
on the authority of the Rector Magnificus
Prof.dr. T.T.M. Palstra,
on account of the decision of the graduation committee,
to be publicly defended
on Friday 31 August 2018 at 14:45

by

Gerhardus Hermanus Petrus Campmans
born on 21 August 1989
in Roosendaal en Nispen, the Netherlands

This dissertation has been approved by:

prof.dr. S.J.M.H. Hulscher	supervisor
dr.ir. P.C. Roos	co-supervisor

‘Tidal waves don’t beg forgiveness’
(Pearl Jam, 2003)

Preface

Na me vier jaar in zandgolven te hebben verdiept, ligt hier nu mijn proefschrift. Hoe interessant zandgolven ook mogen zijn, dit werk heb ik zeker niet kunnen voltooien zonder de steun van velen.

Allereerst wil ik Pieter bedanken voor het begeleiden van mijn promotie. Ik had me geen betere begeleider kunnen wensen! Inhoudelijk had jij altijd sterke input. Meestal zaten we direct op dezelfde golflengte te denken. Letterlijk en figuurlijk... Er was meer dan genoeg ruimte voor minder serieuze zaken, zo is er ook het nodige gegrapt. Mede dankzij jou heb ik hardlopen leren waarderen en hebben we menig lunchpauze rennend doorgebracht. Pieter, bedankt voor al je steun en positiviteit tijdens mijn promotie, vooral tijdens de momenten dat het even niet zo lekker liep. Ik vind het erg leuk om met je samen te werken en ik kijk er naar uit om dit ook in de toekomst te blijven doen.

Suzanne, door de heel directe samenwerking met Pieter, stond jij iets verder van het onderzoek af. Maar tijdens onze meetings was het altijd heel erg duidelijk dat jij erg enthousiast was over het zandgolf onderzoek. Dat onderwerp gaat jou natuurlijk ook extra aan. Ondanks je drukke agenda heb je altijd de tijd gevonden om nuttige feedback te geven op mijn werk. Ik waardeer heel erg hoe jij me je vertrouwen hebt gegeven, zodat ik mijn onderzoek kon doen; ook als het even iets minder gaat. Ik ben erg blij om binnen jouw vakgroep een PostDoc te mogen doen.

Huib, gaande weg mijn promotie traject ben jij betrokken geraakt bij mijn promotie onderzoek. Regelmatig hebben Pieter en ik allerlei lastige problemen aan je voorgelegd. Blijkbaar konden de problemen niet lastig genoeg zijn, want jij wist altijd zinnige suggesties te geven waar wij weer mee verder konden. Op veel vlakken van mijn onderzoek hebben jouw suggesties net voor dat stapje gezorgd waardoor we de onderliggende processen echt leerden begrijpen.

I would like to thank everyone involved in the SMARTSEA project. This research is supported by the Dutch Technology Foundation STW, which is part of the Netherlands Organisation for Scientific Research (NWO), and which is partly funded by the Ministry of Economic Affairs. The project entitled “SMARTSEA: Safe navigation by optimizing sea bed monitoring and waterway maintenance using fundamental knowl-

edge of sea bed dynamics", was granted for the maritime TKI call 2013, on project number 13275. Thanks to SMARTSEA, I was able to do this research. It is in particular during the meetings, that I fully realized the actual need for sand wave research. Thanks to the enthusiasm and constructive feedback, and many practical examples of sand wave problems, I kept motivated to fulfill this research.

Daniel, thank you for hosting me at the Universitat Politècnica de Catalunya. With your help, the computational performance of my nonlinear sand wave model greatly improved. I want to thank you, Albert, Francesca, Nabil and Jaime for a warm welcome in Barcelona. Angels and Rotman, thank you very much for the time that I spent in your apartment in Barcelona. I very much appreciated your hospitality, also that of – the cat – Tully.

Ellis en Sven, ik heb jullie mogen begeleiden tijdens jullie afstudeeropdrachten. Met jullie allebei vond ik het prettig samenwerken. Sven, jouw werk is iets meer een zijpaadje geweest binnen mijn onderzoek en is hier niet terug te vinden, maar het heeft me zeker extra inzichten gegeven. Ellis, jouw werk was direct gerelateerd aan dit onderzoek en heeft er ook toe geleid dat jij mede-auteur bent van een van de artikelen.

To everyone in the WEM department, thank you for the pleasant work environment. I have always enjoyed being part of this group. There were always people around to have a coffee break, talks in the corridor, go for lunch walks or the occasional drinks. I also enjoyed the WEM-outings a lot. Rick, Suleyman, Erik, Olav, Anne, Arjan, Leonardo, Angels and Matthijs, thanks you for being my office-mates! Angels, thank you for all those times that we had discussions that ended up with the white board full of equations and drawings. And thanks for talking about Game of Thrones, programming issues, and going for 'lekkere koffie'. Gràcies! Anke, Joke, Monique en Dorette, dank jullie wel voor al het regelwerk. Regelmatig was ik bij jullie te vinden om een kopje koffie te halen. Bedank voor jullie hulp bij het organiseren van de lunchpraatjes en het vakgroepuitje. John, dankjewel voor al die keren brainstormen over zandgolven; jij vanuit de data analyse kant en ik altijd weer vanuit de model hoek. Joep, jij was altijd wel in voor een kop koffie, lunchwandeling of een daghap. Je hebt me overgehaald om mee te doen aan de Coastal Cycling Tour, dus moest ik snel nog even een racefiets regelen. Als het om sporten gaat, ben jij altijd van de partij. Of het nu gaat om de Estafette Run Borne, lunch runs, een onbenullig lang stuk fietsen of WAMPEX, je bent altijd super fanatiek! Bedankt voor je gezelligheid en steun wanneer het me aan motivatie ontbrak. Johan, bedankt voor het samen trainen voor de halve marathon, de vele lunch wandelingen en het samen racefietsen. Jij kan dingen als geen ander relativeren, en dat heb ik af en toe wel nodig gehad. Anouk, mede door jouw fanatisme voor sporten heb ik meegedaan aan Ride for the Roses en de UT-triatlon. Dankjewel voor al die keren dat we hebben hardgelopen, gefietst en gezwommen. Samen met Joep, Pieter, Anouk, Koen, Johan, Michiel en Juliette heb ik vele lunchpauzes ingevuld met hardlopen. Iets wat ik gaande weg mijn promotie onderzoek erg ben gaan waarderen. Het hielp me mijn hoofd leeg te maken en weer met frisse energie verder te gaan. Naast het hardlopen zijn er ook de nodige

kilometers per racefiets afgelegd samen met Johan, Joep, Anouk, Michiel en Pepijn. Koen en Daan, dank jullie wel voor het bezoek aan Peking na ECSA in Shanghai!

Tijdens mijn studie en het eerste jaar van mijn promotie heb ik met veel plezier bij 'Etje' gewoond. Ik heb nog regelmatig met velen van jullie contact. Zo nu en dan bij de Molly's op vrijdagavond. Gerwin, Liz Daniel en Judith bedankt voor de avonden waarop we samen aten en de series 'Wie is de mol?', 'The Walking Dead' of 'Game of Thrones' keken. Arthur en JW bedankt voor de wandelingen samen. Maar hoe kan ik het over Etje hebben en het niet over kampvuur(tjes?) hebben. Ik heb heel erg genoten van de tijd bij Etje!

Team Delta Yankee, bedankt voor alle gezellige klus avonden. Natuurlijk jammer dat we er achter kwamen dat onze Ka8 meer werk nodig had, dan we hadden gehoopt. Het klussen aan ons vliegtuig ben ik echt leuk gaan vinden. Het heeft me een stuk beter geleerd hoe ons vliegtuig eigenlijk in elkaar zit.

Steeksleutels, het is alweer een hele tijd geleden dat we samen aan de studie werktuigbouwkunde zijn begonnen. Samen hebben we regelmatig gezellig biertjes gedronken, spelletjes gespeeld, op de racefiets rondgefietst, gepubquized en BBQ's gehouden. En niet te vergeten, samen op wintersport! Heel erg bedankt!

Fleur, ik ben heel erg blij dat ik jou heb leren kennen! Dankjewel voor jouw steun tijdens het afronden van mijn promotie. Ik kan altijd mijn verhaal bij jou kwijt, en jij kan als geen ander mijn gedachten bij het werk weghalen. Hopelijk dat we nog lang samen mogen zijn.

Pap en mam, super bedank dat jullie er altijd voor me zijn. Zonder jullie steun had ik dit nooit kunnen doen. Liesbeth, Harm en Anja, jullie ook super bedankt!

Summary

Sand waves are wavy bed patterns that are observed in sandy shallow seas. They have wavelengths of hundreds of meters and heights of up to 10 meters. Sand waves are dynamic, meaning that their height can change and they can migrate up to tens of meters per year. The combination of shallow water, large crest height and their dynamical character implies that a good understanding of sand waves is required for various human activities at seas such as the North Sea. This will help improve surveying and dredging policies required for navigation safety. Other activities that benefit from a better understanding are placement of pipelines and cables and the construction of wind farms.

Sand waves are generated by the interaction between the sandy seabed and the tidal current. Undulations in the seabed affect the current such that tidally averaged circulation cells transport sediment towards the crest. On the other hand, gravity tends to favor downslope sediment transport towards the trough. It is the competition between these two processes that determines the formation of sand waves. Next to the forming mechanism there are various other factors affecting sand wave dynamics. Observations show that sand wave height reduces and their migration rate increases during periods of stormy weather compared to calm conditions. The aim of this research is to understand how storms affect sand wave dynamics.

Wind waves and wind-driven currents are the storm-related processes investigated in this thesis. Two new process-based idealized sand wave models have been developed that include these storm processes. The first model is based on linear stability analysis to systematically investigate the initial formation stage. To investigate the effect of storm processes on finite-amplitude sand wave dynamics a second model has been developed, which is fully nonlinear.

With the linear stability model it is found that wind waves decrease the growth rate and increase the preferred wavelength of sand waves. Although wind waves in this model do not induce migration on their own, they do enhance migration caused by other processes. Wind-driven currents particularly affect sand wave migration. By breaking the – in the model – symmetrical tidal current, sand waves migrate in the direction of the residual current. Wind-driven flow can both increase and decrease the growth of sand waves, depending on wind direction and the Coriolis effect.

By combining typical North Sea wave and wind conditions (corresponding to the Euro Platform) with the linear stability model, using a statistical weighted averaging method, it is found that storms mainly affect sand wave migration. Also a seasonality

in sand wave migration is found. During winter, when stormy conditions occur more often, migration is larger compared to during summer.

Using the nonlinear sand wave model, the evolution towards equilibrium is investigated. Wind waves reduce the equilibrium height and enhance the migration speed caused by wind-driven currents. Wind-driven currents result in asymmetrical sand wave shapes and migration in the direction of their steepest slope. Migration decreases with increasing sand wave height. Simulations of the evolution from randomly distributed small perturbations towards a fully grown sand wave field (for different wave and wind conditions) display larger sand waves overtaking smaller ones. This shows that sand waves interact with each other in complicated ways. Finally, it is found that the intermittent occurrence of storms and fair-weather conditions can lead to a dynamic equilibrium, were sand waves tend to grow towards the equilibrium states corresponding to fair-weather and stormy conditions, but due to limited adaptation time sand waves never reach those equilibrium states. Even short periods of storms can already significantly affect sand wave dynamics.

This research provides process-based support for the influence of storms on sand wave dynamics, as found earlier by observational studies. Furthermore, the two newly developed sand wave models can be used for applications such as sand mining, nautical dredging, wind farms and pipelines.

Samenvatting

Zandgolven zijn golvende bodempatronen die in ondiepe zandige zeeën voorkomen. Deze patronen hebben golflengtes van enkele honderden meters en kunnen tot 10 meter hoog worden. Ze zijn bovendien dynamisch, dat wil zeggen dat hun hoogte kan veranderen en ze kunnen migreren met snelheden tot ongeveer tientallen meters per jaar. Door de combinatie van ondiep water, grote kamhoogte en dynamisch gedrag is het voor allerlei toepassingen, in bijvoorbeeld de Noordzee, van belang goed te weten hoe deze bodemvormen zich gedragen. Hiermee kunnen meetcampagnes en baggerstrategieën voor de scheepvaart efficiënter gepland worden. Andere toepassingen, die baat hebben bij een beter begrip van de zeebodem, zijn het leggen van pijpleidingen en kabels en het aanleggen van windparken.

Zandgolven worden gevormd door de interactie tussen de zandige zeebodem en de getijstroming. De golvende bodem beïnvloedt de stroming zodanig dat er getijgemiddelde circulatiecellen ontstaan die zand van de trog naar de kam transporteren. Omgekeerd zorgt zwaartekracht ervoor dat zand de neiging heeft van kam naar de trog te verplaatsen. De competitie tussen deze twee processen bepaalt of zandgolven ontstaan. Naast dit vormende mechanisme zijn er tal van andere factoren die een rol spelen in de dynamiek van zandgolven. Uit metingen blijkt dat zandgolven lager worden en sneller migreren tijdens periodes met meer stormen. Het doel van dit onderzoek is te begrijpen hoe stormen invloed hebben op zandgolfdynamica.

De stormprocessen die in dit werk onderzocht worden zijn windgolven en windgedreven stroming. Twee nieuwe geïdealiseerde proces-gebaseerde zandgolfmodellen zijn ontwikkeld waarin deze stormprocessen zijn meegenomen. Het eerste is gebaseerd op lineaire stabiliteitsanalyse om de initiële ontwikkelingsfase van zandgolven systematisch te onderzoeken. Om de invloed van stormen op zandgolven van eindige hoogte te kunnen onderzoeken is daarnaast een tweede volledig niet-lineair zandgolfmodel ontwikkeld.

Met het lineaire stabiliteitsmodel is gevonden dat windgolven de groei van zandgolven verminderen en de voorkeursgolflengte langer maken. Hoewel golven hier zelf geen migratie veroorzaken versterken golven migratie als deze wordt veroorzaakt door andere processen. Windgedreven stroming heeft met name invloed op de migratie van zandgolven. Doordat de stroming asymmetrisch wordt migreren de zandgolven in de richting van de reststroming. Wind kan de groei van zandgolven zowel versterken als verzwakken, afhankelijk van de windrichting en het Coriolis effect.

Door golf- en windcondities die typisch zijn voor de Noordzee te combineren met

het lineaire stabiliteitsmodel via een statistisch gewogen middelingsprocedure, blijkt vervolgens dat stormen met name van invloed zijn op de migratiesnelheid. Ook is er seizoensafhankelijkheid gevonden. Tijdens winter periodes zijn er relatief vaak stormen, waardoor de migratie van zandgolven tijdens de winter gemiddeld groter is dan de kalmere zomerperiodes.

Met het niet-lineaire zandgolf model is daarna de ontwikkeling naar evenwichten onderzocht. Windgolven verlagen de evenwichtshoogte en versterken het migratie-effect door windgedreven stroming. Windgedreven stroming leidt tot asymmetrische vormen en migratie in de richting van de steilste helling. Zandgolfmigratie neemt af met zandgolfhoogte. Bij de ontwikkeling vanuit kleine verstoringen van de zeebodem naar een volgroeid zandgolfveld (onder verschillende golf- en wind-condities) blijkt dat juist de grotere zandgolven de kleinere zandgolven inhalen. Dit laat zien dat zandgolven onderling ingewikkelde interacties aangaan. Ten slotte is gevonden dat afwisselende periodes van storm en rustig weer resulteren in een dynamisch evenwicht waar zandgolven afwisselend richting de evenwichtstoestanden tijdens storm en rustig weer veranderen, maar deze nooit bereiken door de beperkte aanpassingstijd. Zelfs korte periodes van storm hebben al behoorlijke invloed op zandgolfdynamiek.

Dit onderzoek biedt vanuit een modelleringsperspectief inzicht in de invloed van stormen op zandgolfdynamiek die eerder al uit observaties bleek. Daarnaast kunnen de twee ontwikkelde zandgolfmodellen gebruikt worden voor toepassingen zoals zandwinning, baggerwerkzaamheden, windparken en pijpleidingen.

Contents

Chapter 1

Introduction

1.1 Tidal sand waves

Tidal sand waves are sandy bed forms observed in tidally dominated shallow seas around the world (Terwindt, 1971; Aliotta and Perillo, 1987; Katoh et al., 1998; Bokuniewicz et al., 1977; Harris, 1989; Barnard et al., 2006; Harvey, 1966; Santoro et al., 2004; Zhou et al., 2018), see Figure 1.1. They are dynamical bed forms that have wavelengths of several hundreds of meters, heights of several meters and can migrate up to tens of meters per year. A typical sand wave field is shown in Figure 1.2. Especially since sand waves are dynamic, detailed knowledge of their behavior is required for various human activities in shallow seas. For example, sand waves may pose a hazard to navigation (Dorst et al., 2011, 2013), pipelines and cables as well as to the foundation of wind farms and gas/oil platforms (Németh et al., 2003). Data analysis, modeling techniques and their combination can be used to gain insight in sand wave dynamics.

Sand waves are formed by the interaction of the tidal flow with a sandy seabed. Hulscher (1996) explained sand waves as an instability of the seabed subject to tidal flow. Next to tidal flow other physical processes affect sand wave dynamics. This thesis focuses on the effects of storms, i.e. wind waves and wind-driven flow, on sand wave dynamics.

The remainder of this chapter contains the background of sand wave dynamics (Section 1.2) followed by the knowledge gap (Section 1.3), research aim (Section 1.4), research questions (Section 1.5) and methodology (Section 1.6). Finally, an outline of the thesis is presented (Section 1.7).

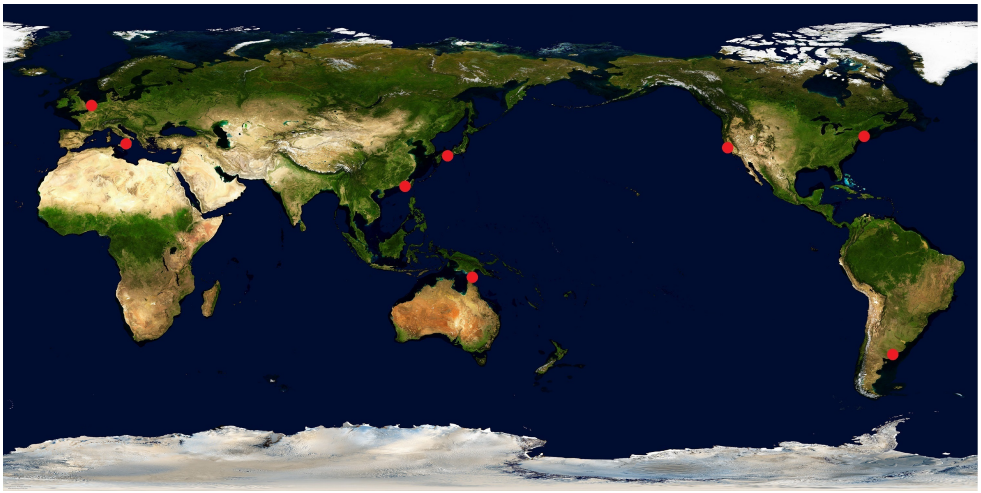

Figure 1.1: The world map with locations where sand wave surveys took place (red dots, references in main text). This is not a complete list of survey locations. Image after worldmapsonline.com.

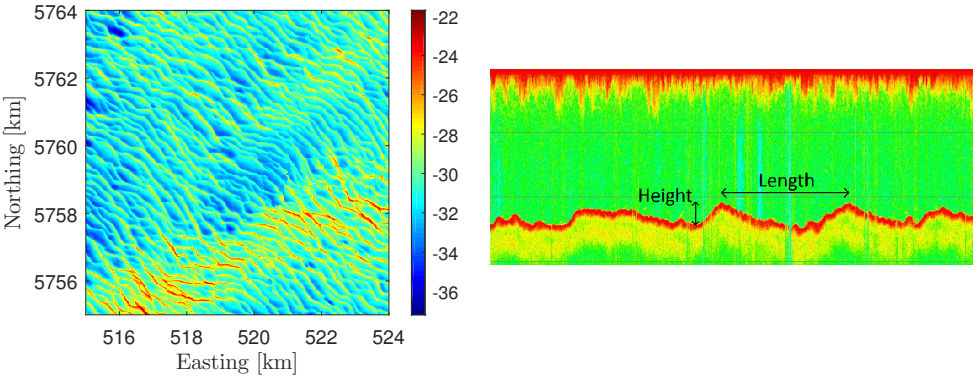

Figure 1.2: Left: bathymetric chart showing a typical sand wave field in the North Sea near the Euro platform (depth in m). Right: echosounder image from the Grådyb tidal inlet, field measurements made by the author during the summer school Coastal and Estuarine Morphodynamics 2014, Skallingen Laboratory, University of Copenhagen at Ho – Blåvand, Denmark. The tidal sand waves observed have an approximate length and height of 100 m and 2 m respectively. The colors indicate the intensity of the reflected acoustic signal from the water column. Red: high intensity, blue/green: low intensity. The sound is mostly reflected by the bed and by water surface distortions.

1.2 Background

1.2.1 Physical setting and processes

Sand waves are found in many tidally dominated shelf seas. These shelf seas formed by submersion of lowlands due to sea level rise. Shelf seas are characterized by shallow water of typically tens to hundred meters deep in between land and the oceans, where water depths are typically kilometers. In these shallow waters the hydrodynamic processes are mainly tidal waves, that are generated in the oceans driven by the gravitational effects of the moon and the sun, and propagate into shallow seas. Additionally meteorological processes such as wind-driven flow, wind waves and storm surges play a role. If the hydrodynamic forces acting on an individual sediment grain at the seabed are strong enough, it will be set in motion. Just above the critical threshold to mobilize sediment, grains will start to slide, role and jump in frequent contact with the seabed. This mode of transport is termed bed load sediment transport (e.g. Van Rijn, 1990). If the hydrodynamic forces increase even further, a sediment grain may become entrained in the turbulent flow, which brings it higher up in the water column where it may travel over much longer distances. This mode of transport is termed suspended load (e.g. Van Rijn, 1990). Spatial variations in sediment transport causes the seabed to change. In turn, changing seabed topography affects the hydrodynamic motion and thus forms a closed loop of processes that affect each other. This loop, known as the morphodynamic loop, is schematically shown in Figure 1.3. The time scale of the bed evolution at which sand waves form is in the order of months to years, much longer than that of the tidal motion which is typically half a day.

In this complicated system where various physical processes interact, it turns out that in specific conditions a flat seabed is unstable. This means that wavy perturbations in the seabed – through the morphodynamic loop – experience positive feedback that makes those perturbations grow in amplitude. This positive feedback explains various bed forms, such as tidal sand waves (Hulscher, 1996), shoreface-connected ridges (Trowbridge, 1995), sand banks (Huthnance, 1982), megaripples and ripples (Blondeaux, 1990). These marine bed forms – which may co-exist in space and time – all have in common that they form rhythmic wavy patterns, but they differ in their spatial and temporal scales as well as their formation mechanisms.

1.2.2 Process-based modeling

In process-based modeling the physical processes are formulated mathematically in order to simulate the morphodynamic system. These mathematical descriptions often follow from physical laws, expressed in terms of partial differential equations supplemented with appropriate boundary conditions. Using these models sand wave dynamics can be investigated.

Within process-based modeling two types exist: A complex modeling approach (e.g., Borsje et al., 2013; Van Gerwen et al., 2018) and an idealized modeling approach. Both modeling approaches have their own advantages and disadvantages.

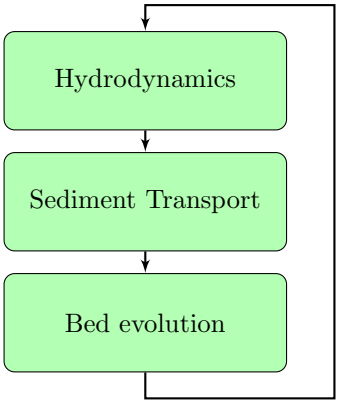

Figure 1.3: The morphodynamic loop, showing interactions among hydrodynamics, sediment transport and bed evolution. The three elements in morphodynamical systems interact forming a closed loop, which may result in complicated feedback mechanisms.

Complex models are aimed at producing quantitatively accurate results for specific model problems and are often used for engineering applications. However, these models typically require much computing time, which restricts their use to a limited number of model runs within available time. Idealized models on the other hand are typically far less demanding on computational time, but give less accurate quantitative results. These models can be used to systematically explore the effect of various processes qualitatively. These two model types both serve their own purposes and should be used in combination: an idealized model to explore which processes are relevant, and subsequently a complex model to obtain quantitatively accurate results for the identified conditions of interest (e.g. Hommes et al., 2007).

Linearized process-based sand wave models can be used to analyze the small-amplitude behavior, non-linear models to analyze the finite-amplitude dynamics. Next to process-based modeling, data driven models exist based on empirical laws (Knaapen and Hulscher, 2002; Knaapen, 2005; Dorst et al., 2009) and cellular automata type models exist based on a set of rules (Knaapen et al., 2013). This thesis uses an idealized modeling approach to explore the effects of storms on sand wave dynamics. The following sections will briefly introduce linear stability analysis and nonlinear modeling approaches in a sand wave context.

Linear stability analysis

After formulating the process-based model, different techniques exist to obtain insight into the solution of the mathematical model. One method is linear stability analysis (Dodd et al., 2003), based on a linearization of the mathematical problem around a so-called basic state. In sand wave models this linearization of the system, denoted

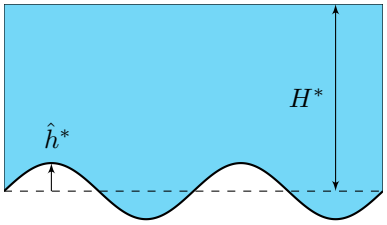

Figure 1.4: Definition sketch (side view) of a sand wave topography with amplitude $\hat{h}^*$ at the seabed of a shallow sea with a mean water depth H^*.

as φ^*, is done with respect to seabed topography h^*, which is written as

$$h^* = \varepsilon h_1 H^*, \qquad \varepsilon \equiv \frac{\hat{h}^*}{H^*} \ll 1. \tag{1.1}$$

Here, ε is defined as the ratio of the seabed amplitude $\hat{h}^*$ and the mean water depth H^* (see Figure 1.4), h_1 is the seabed perturbation shape. The parameter ε needs to be small for linear stability analysis to be applicable. The scaled state of the morphodynamic system's state φ is expanded in the small parameter ε, according to

$$\varphi = \varphi_0 + \varepsilon\varphi_1 + \mathcal{O}(\varepsilon^2). \tag{1.2}$$

Provided that ε is sufficiently small and expansion terms φ_n are of equal order of magnitude, higher order terms φ_2, φ_3, etc. can be neglected to accurately describe the system φ in the regime of small bed-form amplitudes. The zero-order term φ_0 is termed the basic state and represents the morphodynamic system in a flat seabed situation. The first-order term φ_1 is the linear response of the system to seabed perturbations of shape h_1 and is termed the perturbed state. The basic state can be solved independently of the perturbed state by setting $\varepsilon = 0$. For the perturbed state, we analyze Fourier modes as these turn out to be the eigenmodes of the system. This leads to a solution of the form

$$h_1 = \exp(\omega^* t^*)\cos(k_x^* x^* + k_y^* y^* - |\mathbf{k}^*| c_{\mathrm{mig}}^* t^*), \tag{1.3}$$

with topographic wave numbers k_x^* and k_y^*, the elements of the topographic wave vector $\mathbf{k}^*$. By solving the perturbed state problem for given topographic wave numbers and a set of model parameters, the feedback of the morphodynamic system on the seabed perturbation is expressed in a growth rate ω^* and migration rate c_{mig}^*. The flat seabed is termed stable if all possible perturbations decay, i.e. have a negative growth rate. If some mode exists with a positive growth rate, this mode will grow in amplitude, and the basic state is unstable. The fastest growing mode (FGM) is considered the dominant bed form and its four key properties are wavelength $L_{\mathrm{FGM}}^* = 2\pi/|\mathbf{k}_{\mathrm{FGM}}^*|$, crest orientation $\theta_{\mathrm{FGM}} = \arctan(k_y^*/k_x^*)$, migration speed $c_{\mathrm{mig,FGM}}^*$ and growth rate ω_{FGM}^*.

By applying linear stability analysis, sand waves have been explained as free instabilities of the flat seabed subject to tidal flow (Hulscher, 1996). The instability is

caused by the hydrodynamic response to wavy undulations in the seabed. This generates tidally averaged circulation cells that tend to transport sediment from the trough towards the crest. The counteracting mechanism is gravity, which favors downslope sediment transport.

Later, Hulscher's (1996) work was extended regarding the hydrodynamic solution method (Gerkema, 2000; Besio et al., 2003) and various physical mechanisms. For example, sand wave migration can be caused by pressure- or wind-driven residual currents (Németh et al., 2002) and by tidal asymmetry (Besio et al., 2004). Alternatively, Blondeaux and Vittori (2005a,b) refined the turbulence model and included suspended load sediment transport. Other extensions deal with the effects of grain-size variations (Roos et al., 2007; Van Oyen and Blondeaux, 2009), biota (Borsje et al., 2009) and non-erodible bed layers (Blondeaux et al., 2016). Systematic comparison between the properties of observed sand waves and those of the FGM has been carried out by Hulscher and Van den Brink (2001), Van der Veen et al. (2006) and Van Santen et al. (2011). Importantly, all of the above studies are limited to small-amplitude seabed topographies only.

Nonlinear modeling

To analyze sand wave dynamics in their finite amplitude, i.e. beyond the small-amplitude regime, nonlinear models are required. These models no longer make use of a small-parameter expansion, as given in equation (1.2), but instead directly solve the system φ using various numerical techniques. The model equations are discretized both in space and time using finite differences or the finite-volume method and are solved in time by numerical integration or spectral methods. Due to accuracy and stability criteria the computational times required for these type of models may become quite long. Due to computational time limitations nonlinear models are often restricted to 2D-vertical (2DV) model domains, whereas linear stability models often consider 3D model domains. Model outcomes describe the evolution of sand waves in their finite-amplitude regime, enabling investigation of sand wave shapes and their equilibrium height.

Németh et al. (2007) investigated sand wave height, shape and migration. Van den Berg et al. (2012) developed a sand wave model where he used a spectral method for the temporal variations in the flow, in order to investigate sand wave variation on large model domains. A case study compared this model with field data (Sterlini et al., 2009). All of these studies were able to describe equilibrium sand wave profiles on a domain with a length in the order of hundreds of meters and horizontally periodic boundary conditions. Van Gerwen et al. (2018) used the model Delft3D (Lesser et al., 2004) to model sand waves of finite amplitude. Shortcomings of these type of models are generally that the sand wave height is overpredicted by far and that the wavelength of the bed forms keeps increasing for larger model domains, especially at long time scales.

1.2.3 Storm-related processes

Despite the strong emphasis on tide-dominated conditions in earlier studies, various observational and modeling studies indicated that storms affect sand wave dynamics. Below we review observational studies showing that the sand wave height, migration, asymmetry and patterns are affected by storms.

Height One of the most important effects of storms on sand wave dynamics is the reduction in sand wave height. Observations before and after storm events showed that especially the crests of sand waves flattened, and smaller scale bed forms such as megaripples were lowered or completely obliterated (Terwindt, 1971; Langhorne, 1982; Houthuys et al., 1994; Van de Meene et al., 1996; Van Dijk and Kleinhans, 2005). Regarding long-term effects, Terwindt (1971) observed that the sand wave height in the North Sea depends on the frequency of occurrence of storm events. In summer, during fair weather conditions, the sand wave height increased, whereas in winter storms occur more frequently and the crests where eroded. He explained this by the fact that, during storms, surface waves produce sufficiently high orbital velocities to erode the sand wave crests.

Migration Sand wave observations show a range of migration rates; in many cases the net displacements that were observed are 0 – 10 m/yr (Terwindt, 1971; Fenster et al., 1990; Lanckneus and De Moor, 1991). Others observed much larger migration rates of 40 – 270 m/yr (Jones et al., 1965; Ludwick, 1971; Bokuniewicz et al., 1977; Harris, 1989; Buijsman and Ridderinkhof, 2008), sometimes in the same study area (Bokuniewicz et al., 1977). Based on these observations, Fenster et al. (1990) hypothesized that storms may significantly affect sand wave migration. In the Adolphus Channel (Australia), Harris (1989) observed significant migration speeds that reversed direction due to a change of wind direction during the monsoon season. In the Dover Strait, Le Bot et al. (2000) found that sand waves during 1992 – 1995 migrated in a direction opposite to the long-term trend, which they ascribe to variations in wind conditions. In the same area, Idier et al. (2002) observed tidal cycles without flow reversal during stormy weather. Using linear stability analysis, Németh et al. (2002) showed that wind-driven flow, in addition to a symmetrical tidal flow, is able to induce sand wave migration.

Asymmetry Next to the significant and reversed migration, Harris (1989) observed that also the asymmetry of sand waves was reversed during the monsoon season.

Pattern structure Passchier and Kleinhans (2005) observed 3D flat topped sand waves covered by 3D megaripples during seasonal storms on the shoreface. The megaripples on top of the sand waves are active during stormy conditions. Further offshore, 2D sand waves are observed covered by 2D megaripples. Multiple seasonal storm events of low intensity did not have a measurable effect on sand wave morphology. Van Dijk and Kleinhans (2005) explain the difference in sand wave morphology at the two North Sea sites due to the difference in the relative importance of tidal currents and wave activity near the seabed.

1.3 Knowledge gap

As pointed out in Section 1.2.2, all present-day sand wave models include the tidal current to explain sand wave dynamics. In addition to the tide, the effects of various other processes have already been investigated in sand wave models. However, sand wave models still tend to overestimate sand wave height, suggesting that some mechanisms are not properly included or other mechanisms are overlooked. As shown in Section 1.2.3, observations show that storms affect sand wave dynamics, which may lower sand wave heights and affect migration. Combining the observation that sand wave height is typically overestimated by current models – in which storms are absent – and the observational studies showing that storms may lower sand waves suggests that storm processes can be important to better understand sand wave dynamics. However, the influence of storm processes on sand wave dynamics has not yet been investigated systematically.

1.4 Research aim

The aim of this research is to gain insight in the effects of storms, in this thesis defined as wind waves and wind-driven flow, in addition to a background tidal current on sand wave dynamics. Since observations show that storms may be an important factor on sand wave dynamics, and clear insight into storm processes is still lacking.

1.5 Research questions

Based on the research aim, three research questions are formulated:

Q1. What is the effect of storm processes on small-amplitude sand waves?

Q2. What is the effect of a site-specific wave and wind climate on sand wave dynamics?

Q3. What is the effect of storm processes on finite-amplitude sand waves?

1.6 Methodology

1.6.1 Idealized process-based modeling

To answer the research questions, presented in Section 1.5, we choose idealized modeling techniques because they are able to isolate the effects of processes and to systematically analyze their effect. The idealized modeling approach aims to capture the most important mechanisms for sand wave dynamics in an adequate way. By leaving out extra complexity, this enables deeper qualitative analysis of the important processes, quantitative validation with field data becomes hard through simplifications in the

idealized approach. We believe that our idealized modeling approach can be justified by the research aim, that is identifying the qualitative effect of storm processes on sand wave dynamics. To answer the research questions we develop and apply two such models. Firstly, we explore the effects of storms on small-amplitude sand wave dynamics using linear stability analysis. Secondly, we develop a nonlinear model to further analyze storm effects on finite-amplitude sand wave dynamics.

1.6.2 Approach per research question

The research questions from Section 1.5 are further detailed below.

Q1 To answer the first research question, we develop a sand wave model based on linear stability analysis. We include, next to tidal flow, both wind waves and wind-driven flow in arbitrary directions. The first research question addresses the effect of continuous wave and wind conditions on sand wave dynamics. Here we will focus on the effect of storms on sand wave growth, migration, preferred wavelength and orientation. We investigate the potential effect of waves and wind on sand wave dynamics, but do not take the actual occurrence of waves and wind into account.

Q2 To answer the second research question, the linear model developed for the first research question is used to further investigate the effect of an actual site-specific storm climate, i.e. taking into account that wave and wind conditions have a certain probability to occur. The probability of wave and wind conditions follow from 20 years of measurements at the Euro platform in the North Sea. By combining the model results and the probability of wave and wind conditions the effect of a storm climate is analyzed.

Q3 To investigate finite-amplitude sand wave dynamics, i.e. beyond their small-amplitude regime, a new nonlinear model is developed, extending the model developed in Q1. Using this nonlinear sand wave model we investigate the effect of wave and wind conditions on finite-amplitude sand wave dynamics. Storm effects are analyzed for both the evolution towards equilibrium and the equilibrium sand wave dynamics. Finally, we also investigate the effect of a synthetically generated storm sequence to identify the effect of the intermittent nature, i.e. alternating periods with storms and periods of fair-weather, of storm occurrence on sand wave dynamics.

1.7 Outline of the thesis

The thesis is structured as follows: In Chapter 2 research question **Q1** will be addressed by formulating the linear stability model and investigating the effects of waves and wind on the sand wave formation stage. Chapter 3 addresses research question **Q2** by combining the developed linear stability model with actual wave and wind data to analyze the effect of a storm climate on small-amplitude sand wave dynamics. Next, Chapter 4 addresses research question **Q3** by formulating the nonlinear

sand wave model and investigating the effect of waves and wind on sand wave evolution towards equilibrium. Finally, Chapter 5 contains the discussion and conclusions, respectively.

Chapter 2

Modeling the influence of storms on sand wave formation: A linear stability approach*

Abstract

We present an idealized process-based morphodynamic model to study the effect of storms on sand wave formation. To this end, we include wind waves, wind-driven flow and, in addition to bed load transport, suspended load sediment transport. A linear stability analysis is applied to systematically study the influence of wave and wind conditions on growth and migration rates of small-amplitude wavy bed undulations. The effects of the wind and waves of various magnitudes and directions are investigated. Waves turn out to decrease the growth rate of sand waves, because their effect on the downhill gravitational transport component is stronger than their growth-enhancing effect. The wind wave effect is strongest for wind waves perpendicular to the tidal current. In the case of a symmetrical tidal current, wind-driven flow tends to breach the symmetry, thus causing sand wave migration. Wind effects on sand wave behavior are strongly influenced by the Coriolis effect, in magnitude as well as direction. Next to bed load transport, suspended load also has a growing and a decaying mechanism, being the perturbed flow and the perturbed suspended sediment concentration respectively. The decaying mechanism outcompetes the growing mechanism for bed forms with shorter wavelengths. Wind waves increase the growth rate due to suspended load, but this is outcompeted by the reduction in growth rate

*This chapter is published as Campmans, G.H.P., P.C. Roos, H.J. de Vriend, and S.J.M.H. Hulscher (2017). Modeling the influence of storms on sand wave formation: A linear stability approach, *Continental Shelf Research*, **137** 103-116, http://dx.doi.org/10.1016/j.csr.2017.02.002

by wind waves due to bed load transport. We conclude that storms significantly influence sand wave dynamics in their formation stage.

2.1 Introduction

Tidal sand waves are dynamic large-scale rhythmic bed forms observed in many tide-dominated shallow seas that have a sandy seabed (Terwindt, 1971; McCave, 1971), for instance in the North Sea as shown in Figure 2.1. They have wavelengths of 100–800 m and heights of several meters. Sand waves can migrate up to tens of meters per year (Van Dijk and Kleinhans, 2005), and are formed at a time scale of 1–10 yrs.

The behavior of sand waves is of practical interest because they tend to interfere with navigation, cables, and pipelines. Efficient and sustainable use of the North Sea requires generic knowledge of sand wave dynamics.

Process-based morphodynamic models have been developed to improve our understanding of sand wave dynamics (e.g., see the overview by Besio et al., 2008). Tidal ridges as well as sand waves have been explained as free instabilities of the morphodynamic system via linear stability analysis (Hulscher, 1996). The instability is caused by the hydrodynamic response to wavy undulations in the seabed. In the case of sand waves, this generates tidally averaged circulation cells that tend to transport sediment from the trough towards the crest. The counteracting mechanism is gravity, which favors downslope sediment transport. The fastest growing mode (FGM) is considered the dominant bed form and its four key properties are wavelength, crest orientation, migration speed (zero for symmetrical cases studies by Hulscher (1996)) and growth rate.

Later, Hulscher's (1996) work was extended regarding the hydrodynamic solution method (Gerkema, 2000; Besio et al., 2003) and various physical mechanisms. For example, sand wave migration can be caused by pressure- or wind-driven residual currents (Németh et al., 2002) and by tidal asymmetry (Besio et al., 2004). Alternatively, Blondeaux and Vittori (2005a,b) refined the turbulence model and included suspended load sediment transport. Other extensions deal with the effects of grain-size variations (Van Oyen and Blondeaux, 2009), biota (Borsje et al., 2009) and non-erodible

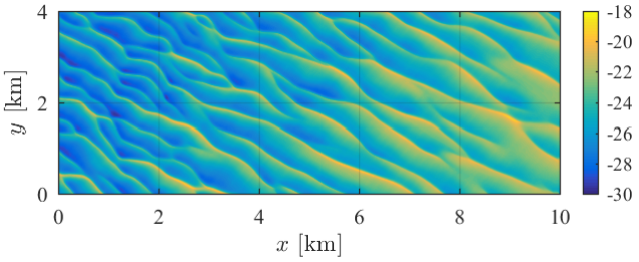

Figure 2.1: Sand wave pattern in the North Sea (data from Royal Dutch Navy). Colors indicate the bed level relative to LAT [m]. The y-axis points northward.

bed layers (Blondeaux et al., 2016). Systematic comparison between the properties of observed sand waves and those of the FGM has been carried out by Hulscher and Van den Brink (2001), Van der Veen et al. (2006) and Van Santen et al. (2011). Other studies extended the linear models towards the nonlinear regime, e.g. connecting to the formation of tidal sandbanks (Komarova and Newell, 2000), three-dimensional sand wave patterns (Blondeaux and Vittori, 2009), or focusing on equilibrium shapes and heights of sand waves (Németh et al., 2007; Sterlini, 2009; Van den Berg et al., 2012). Also complex numerical simulation models have been applied, e.g. to an isolated artificial sand wave (Tonnon et al., 2007) or aimed at reproducing results from idealized stability models in connection to turbulence (Borsje et al., 2013) and suspended load (Borsje et al., 2014).

Observations show a significant influence of storms on sand wave dynamics. For example, sand wave heights are reduced during stormy periods (Terwindt, 1971; Langhorne, 1982; Houthuys et al., 1994; Van de Meene et al., 1996; Van Dijk and Kleinhans, 2005). Furthermore, McCave (1971) explained the decreasing sand wave heights towards the coast by an increased importance of wind waves and suggested that wave action prevents the development of sand waves even closer to the coast. In Long Island Sound (U.S.A.), Fenster et al. (1990) observed hardly any migration after a period of fair weather, whereas Bokuniewicz et al. (1977) observed a significant migration rate in the same area. Fenster et al. (1990) suggested that storms may play a major role in the migration of sand waves. In the Adolphus Channel (Australia), Harris (1989) observed significant migration speeds that reverse direction due to a change of wind direction during the monsoon season. In the Dover Strait, Le Bot et al. (2000) found that sand waves during 1992-1995 migrated in a direction opposite to the long-term trend, which they ascribe to variations in wind conditions. In the same area, Idier et al. (2002) observed tidal cycles without flow reversal during stormy weather. Finally, by looking at the internal structure of sand waves in the same region, Ferret et al. (2010) found a formation periodicity in the range of 4 to 18 years, which coincides with tidal cyclicities and variability of storm activity in northern Europe.

Despite the above observations, storm-related processes have not been investigated systematically in a process-based sand wave model. In this paper we will address the question to what extent wave and wind effects need to be taken into account in sand wave formation models and, if so, what are the most important mechanisms. To this end, we present a three-dimensional idealized sand wave model to systematically investigate the influence of storm-related processes on sand wave dynamics in the formation stage. Herein, we include three storm-related processes: (*i*) wind waves, (*ii*) wind-driven flow and (*iii*) suspended sediment transport. In doing so, we have typical North Sea conditions in mind, with wave heights of 1–10 m and wind speeds up to 30 m s^{-1} (Weisse and Günther, 2007). The main innovation is that we systematically analyze these processes (both separately and in combination) and, further, that we allow the wind and waves to come from an arbitrary direction with respect to the tidal current.

The paper is structured as follows. Section 2.2 gives the model formulation and Section 2.3 describes the scaling and solution procedures. In Section 2.4 the model

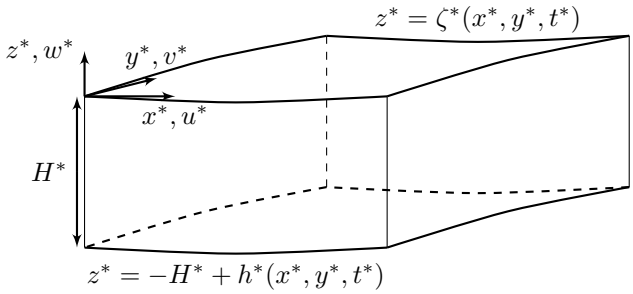

Figure 2.2: Definition sketch of the model geometry showing: 3D coordinate system and velocity components, The mean water depth H^*, topographic undulations represented by h^* and the free surface elevation by ζ^*.

results on the individual processes and the combined effects are presented and the mechanisms are explained. Finally, Section 2.5 and 2.6 contain the discussion and conclusion, respectively.

2.2 Model formulation

2.2.1 Geometry

Consider tidal flow (typical velocity U^* and frequency σ^*) in an offshore part of a shallow shelf sea far away from coastal boundaries. We adopt a coordinate system $\mathbf{x}^* = (x^*, y^*, z^*)^T$ where the vertical coordinate z^* is pointing upward, and $z^* = \zeta^*$ denotes the free surface level. Unscaled quantities are denoted by an asterisk. The sea bed is located at $z^* = -H^* + h^*$, where H^* is the mean water depth and h^* is the sea bed topography which depends on the horizontal coordinates x^* and y^*. Figure 2.2 schematically shows the model geometry.

2.2.2 Hydrodynamics

Currents module Conservation of mass and momentum is expressed by the three-dimensional shallow-water equations:

$$\boldsymbol{\nabla}^* \cdot \mathbf{u}^* = 0, \tag{2.1}$$

$$\frac{\partial \mathbf{u}_\mathrm{h}^*}{\partial t^*} + \mathbf{u}^* \cdot \boldsymbol{\nabla}^* \mathbf{u}_\mathrm{h}^* + f^* \left[\mathbf{e}_z \times \mathbf{u}^*\right]_\mathrm{h} = -g^* \boldsymbol{\nabla}_\mathrm{h}^* \zeta^* + A_\mathrm{v}^* \frac{\partial^2 \mathbf{u}_\mathrm{h}^*}{\partial {z^*}^2}. \tag{2.2}$$

Here, $\mathbf{u}^* = (u^*, v^*, w^*)^T$ is the flow velocity vector, g^* the gravitational acceleration, $f^* = 2\Omega^* \sin\phi$ the Coriolis parameter (with $\Omega^* = 7.292 \cdot 10^{-5}$ rad/s the angular frequency of the Earth's rotation and latitude ϕ), $\mathbf{e}_z$ the unit vector in z^*-direction, A_v^* the vertical eddy viscosity, which is assumed constant and uniform,

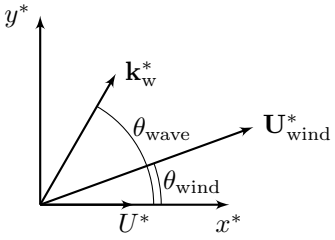

Figure 2.3: Definition sketch (top view) of the tidal current U^*, the wind velocity vector $\mathbf{U}_{\mathrm{wind}}^*$ and wave vector $\mathbf{k}_{\mathrm{w}}^*$ (in the direction in which the waves propagate). Although the depth-averaged tidal flow can be in arbitrary direction, in our model simulations it is always chosen aligned with the x-axis.

$\boldsymbol{\nabla}^* = (\frac{\partial}{\partial x^*}, \frac{\partial}{\partial y^*}, \frac{\partial}{\partial z^*})^T$ the nabla operator and the subscript $_{\mathrm{h}}$ denotes the horizontal (x^*- and y^*-) components of the vector.

The corresponding boundary conditions at the free surface ($z^* = \zeta^*$) are

$$w^* = \frac{\partial \zeta^*}{\partial t^*} + \mathbf{u}_{\mathrm{h}}^* \cdot \boldsymbol{\nabla}_{\mathrm{h}}^* \zeta^*, \quad A_{\mathrm{v}}^* \frac{\partial \mathbf{u}_{\mathrm{h}}^*}{\partial z^*} = \frac{\boldsymbol{\tau}_{\mathrm{wind}}^*}{\rho^*}. \tag{2.3}$$

Here, $\boldsymbol{\tau}_{\mathrm{wind}}^*$ is the wind-induced shear stress vector, and ρ^* is the water density. The wind-induced shear stress is given by

$$\boldsymbol{\tau}_{\mathrm{wind}}^* = \rho_{\mathrm{a}}^* C_d |\mathbf{U}_{\mathrm{wind}}^*| \mathbf{U}_{\mathrm{wind}}^*, \tag{2.4}$$

where $\mathbf{U}_{\mathrm{wind}}^*$ is the horizontal wind velocity vector at 10 m above the sea surface, C_d is a friction factor (e.g., Makin et al., 1995) and ρ_{a}^* is the air density. The boundary conditions at the seabed ($z^* = -H^* + h^*$) are

$$w^* = \frac{\partial h^*}{\partial t^*} + \mathbf{u}_{\mathrm{h}}^* \cdot \boldsymbol{\nabla}_{\mathrm{h}}^* h^*, \quad \frac{\boldsymbol{\tau}^*}{\rho^*} \equiv A_{\mathrm{v}}^* \frac{\partial \mathbf{u}_{\mathrm{h}}^*}{\partial z^*} = S^* \mathbf{u}_{\mathrm{h}}^*. \tag{2.5}$$

Here, S^* is a slip parameter and $\boldsymbol{\tau}^*$ the bed shear stress due to currents. The constant eddy viscosity in combination with the partial slip boundary condition, i.e. the simplest possible turbulence closure, is capable of capturing the most important processes for the formation of sand waves (Hulscher, 1996).

The tidal current in the model is forced by a spatially uniform yet time-dependent free surface gradient, such that the flow over a flat bed attains prescribed depth-averaged values. These values include: major axis of the current amplitude, ellipticity (the ratio of the minor and major axes), direction and phase. Although our model allows for arbitrary tidal flow, in the presented results (in Section 2.4) the depth averaged M2 tidal current is always chosen to be aligned with the x^*-axis. Wind-driven flow is driven by a prescribed wind velocity $\mathbf{U}_{\mathrm{wind}}^*$, assumed steady on the tidal time scale and blowing in the direction θ_{wind} with respect to the x^*-axis, as shown in Figure 2.3.

Wave parameterization Wind waves are included to capture the increased shear stress at the bed. The combined shear stress, $\boldsymbol{\tau}^*_{\mathrm{cw}}$, due to both currents and waves is written as

$$\boldsymbol{\tau}^*_{\mathrm{cw}} = \boldsymbol{\tau}^* + \boldsymbol{\tau}^*_{\mathrm{w}}, \tag{2.6}$$

where $\boldsymbol{\tau}^*$ is the current-induced shear stress from Eq.(2.5) and $\boldsymbol{\tau}^*_{\mathrm{w}}$ the wave induced shear stress. Adopting this linear composition, we intentionally ignore possible non-linear enhancement (Soulsby et al., 1993). The wave-induced shear stress is given by a quadratic stress relation

$$\boldsymbol{\tau}^*_{\mathrm{w}} = \frac{1}{2}\rho^* f^*_{\mathrm{w}} |\mathbf{u}^*_{\mathrm{w}}| \mathbf{u}^*_{\mathrm{w}}, \tag{2.7}$$

where f^*_{w} is a friction factor (Nielsen, 1992). Moreover, $\mathbf{u}^*_{\mathrm{w}}$ is the near-bed wave velocity, based on linear wave theory (e.g. Mei, 1989), given by

$$\mathbf{u}^*_{\mathrm{w}} = \frac{\mathbf{k}^*_{\mathrm{w}}}{|\mathbf{k}^*_{\mathrm{w}}|} \frac{\sigma^*_{\mathrm{w}} H^*_{\mathrm{wave}} \cos(\sigma^*_{\mathrm{w}} t^*)}{2\sinh(|\mathbf{k}^*_{\mathrm{w}}| H^*)}. \tag{2.8}$$

Here σ^*_{w} is the angular frequency, $\mathbf{k}^*_{\mathrm{w}} = (k^*_{\mathrm{w},x}, k^*_{\mathrm{w},y})^T$ the wave vector and H^*_{wave} the wave height. The magnitude of the wave vector is determined by the dispersion relation, given by

$${\sigma^*_{\mathrm{w}}}^2 = g^* |\mathbf{k}^*_{\mathrm{w}}| \tanh(|\mathbf{k}^*_{\mathrm{w}}| H^*), \tag{2.9}$$

and the direction θ_{wave} with respect to the x^*-axis, as shown in Figure 2.3, is imposed externally. In this model we ignore shoaling, refraction, diffraction and Doppler shifts due to currents. This implies that our model cannot distinguish between waves propagating in opposite directions.

2.2.3 Sediment transport

Bed load Bed load sediment transport is described by a general transport formula:

$$\mathbf{q}^*_{\mathrm{b}} = \alpha^*_{\mathrm{b}} |\boldsymbol{\tau}^*_{\mathrm{cw}}|^{\beta_{\mathrm{b}}} \left(\frac{\boldsymbol{\tau}^*_{\mathrm{cw}}}{|\boldsymbol{\tau}^*_{\mathrm{cw}}|} - \lambda^* \boldsymbol{\nabla}^*_{\mathrm{h}} h^* \right), \tag{2.10}$$

where $\mathbf{q}^*_{\mathrm{b}}$ is the volumetric bed load sediment flux, α^*_{b} a bed load coefficient, λ^* a bed-slope correction parameter and β_{b} the exponent expressing the nonlinearity of the sediment transport in this power law (typically $\beta_{\mathrm{b}} = 1.5$). The critical shear stress for initiation of sediment motion is ignored.

Suspended load Suspended sediment transport is described by an advection-diffusion equation, given by

$$\frac{\partial c^*}{\partial t^*} + \mathbf{u}^* \cdot \boldsymbol{\nabla}^* c^* - w^*_{\mathrm{s}} \frac{\partial c^*}{\partial z^*} = A^*_{\mathrm{v}} \frac{\partial^2 c^*}{\partial {z^*}^2}. \tag{2.11}$$

Here, c^* is the volumetric suspended sediment concentration and w_{s}^* is the settling velocity. The vertical sediment diffusivity is assumed to be equal to the vertical eddy viscosity, A_{v}^*. The corresponding boundary condition at the free surface ($z^* = \zeta^*$), stating zero normal flux through the interface, is given by

$$c^* w_{\mathrm{s}}^* + A_{\mathrm{v}}^* \frac{\partial c^*}{\partial z^*} = 0. \tag{2.12}$$

At the sea bed ($z^* = -H^* + h^*$) the vertical sediment flux satisfies

$$c^* w_{\mathrm{s}}^* + A_{\mathrm{v}}^* \frac{\partial c^*}{\partial z^*} = D^* - E^*, \tag{2.13}$$

where $D^* = w_{\mathrm{s}}^* c^*$ is a deposition function and $E^* = w_{\mathrm{s}}^* c_{\mathrm{ref}}^*$ is a pick-up function, both evaluated at the sea bed $z^* = -H^* + h^*$. Simplifying Van Rijn (2007), the reference concentration, c_{ref}^*, is modeled as a power law of the combined bed shear stress, given by

$$c_{\mathrm{ref}}^* = \left\langle \alpha_{\mathrm{s}}^* |\boldsymbol{\tau}_{\mathrm{cw}}^*|^{\beta_{\mathrm{s}}} \right\rangle_{\mathrm{w}}, \tag{2.14}$$

where α_{s}^* is the suspended load coefficient, β_{s} an exponent (typically $\beta_{\mathrm{s}} = 1.5$) and $\langle\cdot\rangle_{\mathrm{w}}$ denotes wave averaging. In this model waves only affect the pick-up of sediment; the wave-averaged reference concentration is used in the advection-diffusion equation. Also here, the critical shear stress is ignored.

Without loss of generality, the reference height for sediment pick-up is assumed to coincide with the height of the partial slip boundary condition in Eq.(2.5), i.e. $z^* = -H^* + h^*$.

2.2.4 Bed evolution

The evolution of the bed, due to both bed load and suspended load transport, is described by

$$(1-p)\frac{\partial h^*}{\partial t^*} = -\boldsymbol{\nabla}_{\mathrm{h}}^* \cdot \mathbf{q}_{\mathrm{b}}^* + D^* - E^*, \tag{2.15}$$

where p is the void fraction of the sediment in the sea bed (typically $p = 0.4$). To analyze different growth mechanisms due to suspended load in Section 2.4, we reformulate the bed evolution equation in terms of horizontal suspended sediment fluxes according to

$$(1-p)\frac{\partial h^*}{\partial t^*} = -\boldsymbol{\nabla}_{\mathrm{h}}^* \cdot \mathbf{q}_{\mathrm{b}}^* - \boldsymbol{\nabla}_{\mathrm{h}}^* \cdot \mathbf{q}_{\mathrm{s}}^* - S_s^*, \tag{2.16}$$

where, $\mathbf{q}_{\mathrm{s}}^*$ is the depth-integrated horizontal suspended load flux vector, given by

$$\mathbf{q}_{\mathrm{s}}^* = \int_{-H^*+h^*}^{\zeta^*} c^* \mathbf{u}_{\mathrm{h}}^* \mathrm{d}z^* \tag{2.17}$$

and $S_s^* = \int_{-H^*+h^*}^{\zeta^*} \frac{\partial c^*}{\partial t^*} \mathrm{d}z^*$ is the instantaneous storage term of suspended sediment in the water column, which vanishes when averaging over a time-periodic solution.

Table 2.1: Overview of model parameters and their typical values.

Model parameter	Symbol	Typical values	Reference value†	Unit
Topographic wave number	K^*	0.008 – 0.06	0.01	rad m^{-1}
Water depth	H^*	15 – 40	30	m
Tidal current velocity (M2)	U^*	0.3 – 0.8	0.5	m s^{-1}
Tidal frequency (M2)	σ^*	$1.41 \cdot 10^{-4}$	$1.41 \cdot 10^{-4}$	rad s^{-1}
Wind wave frequency	σ^*_{w}	0.3 – 2.1	1.05	rad s^{-1}
Wave friction factor	f^*_{w}	0.1	0.1	-
Gravitational acceleration	g^*	9.81	9.81	m s^{-2}
Vertical eddy viscosity	A^*_{v}	0.025 – 0.09	0.04	m^2 s^{-1}
Slip parameter	S^*	$0 - \infty$	0.01	m s^{-1}
Slope correction factor	λ^*	1 – 2	1.5	-
Latitude	ϕ	-90 – 90	52	$^\circ$
Coriolis parameter	f^*	$1.15 \cdot 10^{-4}$	$1.15 \cdot 10^{-4}$	rad s^{-1}
Tidal ellipticity (M2)	ϵ_{M2}	0 – 1	0.1	-
Sediment grain size	d^*	200 – 500	350	μm
Settling velocity	w^*_{s}	0.026 – 0.072	0.052	m s^{-1}
Bed load exponent	β_{b}	1 – 2	1.5	-
Suspended load exponent	β_{s}	1 – 2	1.5	-
Bed load coefficient	α^*_{b}	–	$1.56 \cdot 10^{-5}$	$m^{\beta_{\mathrm{b}}+2} s^{2\beta_{\mathrm{b}}-1} kg^{-\beta_{\mathrm{b}}}$
Suspended load coefficient	α^*_{s}	–	$1.05 \cdot 10^{-4}$	$m^{\beta_{\mathrm{s}}} s^{2\beta_{\mathrm{s}}} kg^{-\beta_{\mathrm{s}}}$

†Unless stated otherwise, these values are used in Section 2.4.

2.3 Solution method

2.3.1 Scaling procedure

The model equations are now scaled to find the relative importance of each of the terms in the equations and to identify non-dimensional parameters. Let us first elaborate on the water level gradient term in Eq.(2.2). This term is written as the superposition of two separate terms

$$-g^*\boldsymbol{\nabla}^*_{\mathrm{h}}\zeta^* = -\mathbf{F}^* - g^*\boldsymbol{\nabla}^*_{\mathrm{h}}\tilde{\zeta}^* \tag{2.18}$$

each associated with a different length scale: (i) the length scale of the tidal wave, and (ii) the length scale of the sand waves. At the scale of sand waves the tidal wave is considered spatially uniform. Therefore, the forcing is spatially uniform $\mathbf{F}^* = (F^*_x, F^*_y)^T$. The water level gradient in response to topographic undulations is represented by $-g^*\boldsymbol{\nabla}^*_{\mathrm{h}}\tilde{\zeta}^*$.

The coordinates are scaled as follows:

$$\begin{aligned} \mathbf{x}^* &= (x/K^*, y/K^*, H^*z)^T, \\ t^* &= t_{\mathrm{w}}/\sigma^*_{\mathrm{w}} = t/\sigma^* = T^*_{\mathrm{m}} t_{\mathrm{m}}, \end{aligned} \tag{2.19}$$

where x,y and z are dimensionless coordinates and K^* is the topographic wave number. Here, we tentatively choose H^* as vertical length scale. As we will see further below, this is acceptable for the flat bed flow problem (termed basic flow) because the water depth is of the same order as the Stokes depth $\sqrt{2A^*_{\mathrm{v}}/\sigma^*}$. However, the

vertical scale for the perturbed flow over an undulating bed is much smaller; we will discuss this in Section 2.5.2. In the morphological problem three time scales play a role: (i) the wind wave time scale $1/\sigma^*_{\rm w}$, (ii) the tidal time scale $1/\sigma^*$ and (iii) the morphodynamic time scale $T^*_{\rm m}$. This introduces three time coordinates: $t_{\rm w}$, t and $t_{\rm m}$ for the wave, tide and morphological time scales, respectively. The morphological time scale $T^*_{\rm m}$ is given by

$$T^*_{\rm m} = \min(T^*_{\rm m,b}, T^*_{\rm m,s}), \tag{2.20}$$

which equals the shortest time scale induced by either bed load $T^*_{\rm m,b}$ or suspended load $T^*_{\rm m,s}$, given by

$$\begin{aligned} T^*_{\rm m,b} &= (1-p)H^*/(K^*\alpha^*_{\rm b}(\rho^*U^*H^*\sigma^*)^{\beta_{\rm b}}),\\ T^*_{\rm m,s} &= (1-p)/(K^*U^*\alpha^*_{\rm s}(\rho^*U^*H^*\sigma^*)^{\beta_{\rm s}}). \end{aligned} \tag{2.21}$$

Next, the dependent quantities are scaled according to:

$$\begin{aligned} &\mathbf{u}^* = (U^*u, U^*v, U^*H^*K^*w)^T, && \boldsymbol{\tau}^* = \rho^*U^*H^*\sigma^*\boldsymbol{\tau},\\ &\mathbf{q}^*_{\rm b} = \alpha^*_{\rm b}(\rho^*U^*H^*\sigma^*)^{\beta_{\rm b}}\mathbf{q}_{\rm b}, && h^* = H^*h,\\ &\mathbf{q}^*_{\rm s} = H^*U^*\alpha^*_{\rm s}(\rho^*U^*H^*\sigma^*)^{\beta_{\rm s}}\mathbf{q}_{\rm s}, && \tilde{\zeta}^* = {U^*}^2/g^*\zeta,\\ &c^* = \alpha^*_{\rm s}(\rho^*U^*H^*\sigma^*)^{\beta_{\rm s}}c, \end{aligned} \tag{2.22}$$

with U^* the depth-averaged tidal flow amplitude. An overview of the model parameters, as well as the used default values, is shown in Table 2.1.

In scaled form the currents module becomes:

$$\boldsymbol{\nabla}\cdot\mathbf{u} = 0, \tag{2.23}$$

$$\frac{\partial \mathbf{u}_{\rm h}}{\partial t} + r\mathbf{u}\cdot\boldsymbol{\nabla}\mathbf{u}_{\rm h} + f\left[\mathbf{e}_z\times\mathbf{u}\right]_{\rm h} = -r\boldsymbol{\nabla}_{\rm h}\zeta - \mathbf{F} + A_{\rm v}\frac{\partial^2\mathbf{u}_{\rm h}}{\partial z^2}. \tag{2.24}$$

Here $r = U^*K^*/\sigma^*$ is the Keulegan-Carpenter number, $f = f^*/\sigma^*$ the scaled Coriolis parameter, $\mathbf{F} = \mathbf{F}^*/(U^*\sigma^*)$ the scaled forcing term and finally $A_{\rm v} = A^*_{\rm v}/(H^{*2}\sigma^*)$ the scaled vertical eddy viscosity parameter.

The scaled free surface boundary conditions ($z = 0$) are

$$w = 0, \qquad A_{\rm v}\frac{\partial \mathbf{u}_{\rm h}}{\partial z} = \boldsymbol{\tau}_{\rm wind}, \tag{2.25}$$

where we have used that $\frac{{\rm Fr}^2}{r} = 2.4\cdot10^{-5} \ll 1$ and $\frac{{\rm Fr}^2}{r^2} = 6.8\cdot10^{-7} \ll 1$, such that the boundary condition can effectively be applied at $z = 0$ and the vertical velocity vanishes at the free surface. Here, ${\rm Fr} = U^*/\sqrt{g^*H^*}$ is the Froude number. The scaled sea bed boundary conditions ($z = -1 + h$) are

$$w = \mathbf{u}_{\rm h}\cdot\boldsymbol{\nabla}_{\rm h}h, \qquad \boldsymbol{\tau} \equiv A_{\rm v}\frac{\partial \mathbf{u}_{\rm h}}{\partial z} = S\mathbf{u}_{\rm h}, \tag{2.26}$$

where $S = S^*/(H^*\sigma^*)$ is the scaled slip parameter. The scaled form of the combined shear stress is

$$\boldsymbol{\tau}_{\mathrm{cw}} = \boldsymbol{\tau} + \boldsymbol{\tau}_{\mathrm{w}}, \tag{2.27}$$

where the scaled wind-induced shear stress formulation becomes

$$\boldsymbol{\tau}_{\mathrm{w}} = \frac{1}{2} f_{\mathrm{w}} |\mathbf{u}_{\mathrm{w}}| \mathbf{u}_{\mathrm{w}}. \tag{2.28}$$

Here $f_{\mathrm{w}} = f_{\mathrm{w}}^* U^* / (H^* \sigma^*)$ is the scaled wave friction factor. The scaled near-bed wave velocities are given by

$$\mathbf{u}_{\mathrm{w}} = \frac{1}{2} H_{\mathrm{wave}} \frac{\mathbf{k}_{\mathrm{w}}}{|\mathbf{k}_{\mathrm{w}}|} \frac{\cos(t_{\mathrm{w}})}{\sinh(|\mathbf{k}_{\mathrm{w}}|)}, \tag{2.29}$$

where $H_{\mathrm{wave}} = H_{\mathrm{wave}}^* \sigma_{\mathrm{w}}^* / U^*$ is the scaled wave height and $\mathbf{k}_{\mathrm{w}} = \mathbf{k}_{\mathrm{w}}^* H^*$ the scaled wave vector. The scaled dispersion relation is given by ${\sigma_{\mathrm{w}}^*}^2 H^* / g^* = |\mathbf{k}_{\mathrm{w}}| \tanh(|\mathbf{k}_{\mathrm{w}}|)$.

The scaled wave-averaged bed load transport formula becomes

$$\mathbf{q}_{\mathrm{b}} = \left\langle |\boldsymbol{\tau}_{\mathrm{cw}}|^{\beta_{\mathrm{b}}} \left(\frac{\boldsymbol{\tau}_{\mathrm{cw}}}{|\boldsymbol{\tau}_{\mathrm{cw}}|} - \lambda \boldsymbol{\nabla}_{\mathrm{h}} h \right) \right\rangle_{\mathrm{w}}, \tag{2.30}$$

where $\lambda = \lambda^* H^* K^*$ is the scaled slope correction factor and $\langle \cdot \rangle_{\mathrm{w}}$ denotes wave averaging. The scaled suspended sediment transport model becomes

$$\frac{\partial c}{\partial t} + r \mathbf{u} \cdot \boldsymbol{\nabla} c - w_{\mathrm{s}} \frac{\partial c}{\partial z} = A_{\mathrm{v}} \frac{\partial^2 c}{\partial z^2}, \tag{2.31}$$

where $w_{\mathrm{s}} = w_{\mathrm{s}}^* / (H^* \sigma^*)$ is the scaled settling velocity. The boundary conditions at the free surface ($z = 0$) and at the bed ($z = -1 + h$) are respectively:

$$\begin{aligned} w_{\mathrm{s}} c + A_{\mathrm{v}} \frac{\partial c}{\partial z} &= 0, \\ w_{\mathrm{s}} c + A_{\mathrm{v}} \frac{\partial c}{\partial z} &= w_{\mathrm{s}} (c - c_{\mathrm{ref}}), \end{aligned} \tag{2.32}$$

where we have used that $\frac{\mathrm{Fr}^2}{r} = 2.4 \cdot 10^{-5} \ll 1$, such that the surface boundary condition can effectively be applied at $z = 0$. The scaled reference concentration is

$$c_{\mathrm{ref}} = \left\langle |\boldsymbol{\tau}_{\mathrm{cw}}|^{\beta_{\mathrm{s}}} \right\rangle_{\mathrm{w}}. \tag{2.33}$$

Finally, the scaled bed evolution equation is given by

$$\frac{\partial h}{\partial t_{\mathrm{m}}} = -\mu_{\mathrm{b}} \boldsymbol{\nabla}_{\mathrm{h}} \cdot \langle \mathbf{q}_{\mathrm{b}} \rangle_{\mathrm{t}} - \mu_{\mathrm{s}} \boldsymbol{\nabla}_{\mathrm{h}} \cdot \langle \mathbf{q}_{\mathrm{s}} \rangle_{\mathrm{t}}, \tag{2.34}$$

where the coefficients $\mu_{\mathrm{b}} = T_{\mathrm{m}}^* / T_{\mathrm{m,b}}^*$ and $\mu_{\mathrm{s}} = T_{\mathrm{m}}^* / T_{\mathrm{m,s}}^*$ depend on the morphological time scales due to bed load and suspended load as introduced in Eq.(2.20). Because the tidal time scale is small compared to the morphological time scale, only the tidally averaged sediment transport, denoted by $\langle \cdot \rangle_{\mathrm{t}}$, effectively contributes to the bed evolution.

The group of dimensionless numbers obtained in the scaling procedure is shown in Table 2.2.

Table 2.2: The dimensionless numbers obtained from the scaling procedure.

Description	Symbol	Expression	Typical value[†]
Froude number	Fr	$U^*/\sqrt{g^* H^*}$	0.029
Keulegan-Carpenter number	r	$U^* K^*/\sigma^*$	35.5
Vertical diffusion parameter	A_v	$A_\mathrm{v}^*/(\sigma^* H^{*2})$	0.32
Scaled resistance parameter	S	$S^*/(H^*\sigma^*)$	2.4
Scaled slope correction factor	λ	$\lambda^* H^* K^*$	0.45
Relative importance of bed load	μ_b	$T_\mathrm{m}^*/T_\mathrm{m,b}^*$	≤ 1
Relative importance of suspended load	μ_s	$T_\mathrm{m}^*/T_\mathrm{m,s}^*$	≤ 1
Scaled wave friction factor	f_w	$f_\mathrm{w}^* U^*/(H^*\sigma^*)$	12
Scaled Coriolis parameter	f	f^*/σ^*	0.82
Scaled settling velocity	w_s	$w_\mathrm{s}^*/(H^*\sigma^*)$	12.3
Scaled wind wave number	$\lvert\mathbf{k}_\mathrm{w}\rvert$	$\lvert\mathbf{k}_\mathrm{w}^*\rvert H^*$	4
Scaled wind wave surface height	H_wave	$\sigma_\mathrm{w}^* H_\mathrm{wave}^*/U^*$	1

[†]Based on the typical values given in Table 2.1.

2.3.2 Outline of the linear stability analysis

Using linear stability analysis, we investigate the stability of the flat bed subject to a spatially uniform tidal motion, termed the basic state. This is achieved by analyzing the response of the system to low-amplitude sinusoidal topographic perturbations

$$h^*|_{t^*=0} = \breve{h}^{*\mathrm{init}} \cos\left(K^*[x^* \cos\theta + y^* \sin\theta]\right). \tag{2.35}$$

Here, $\breve{h}^{*\mathrm{init}}$ is the initial amplitude, K^* the topographic wave number and θ the angle between the x-axis and the topographic wave vector, pointing in the crest-normal direction. After scaling Eq.(2.35), the bed level is given by

$$h|_{t_\mathrm{m}=0} = \varepsilon h_1|_{t_\mathrm{m}=0} = \varepsilon \breve{h}_1^{\mathrm{init}} \cos\left(\mathbf{k} \cdot \mathbf{x}_\mathrm{h}\right). \tag{2.36}$$

Here, h is the bed level, $\varepsilon = \breve{h}^*/H^* \ll 1$ a small expansion parameter, h_1 the perturbed bed level with initial amplitude $\breve{h}_1^{\mathrm{init}}$ and $\mathbf{k} = (k_x, k_y)^T = (\cos\theta, \sin\theta)^T$ is the topographic wave vector. Because of our scaling procedure, using $1/K^*$ as topographic length scale in Eq.(2.19), it follows that $|\mathbf{k}| = 1$.

The unknowns of the system $\varphi = (h, \mathbf{u}, \boldsymbol{\tau}, c, c_\mathrm{ref}, \mathbf{q}_\mathrm{b}, \mathbf{q}_\mathrm{s})$ are expanded in powers of ε, given by

$$\varphi = \varphi_0 + \varepsilon\varphi_1 + \mathcal{O}(\varepsilon^2). \tag{2.37}$$

Here, φ_0 represents the basic state, φ_1 the perturbed state, and higher-order terms are neglected since ε is small.

The system is linearly stable, if for all possible bed perturbations (referred to as 'modes') the amplitudes decay. If for at least one mode bed the amplitude grows, the basic state is unstable. The mode with the maximum growth rate is termed the fastest growing mode (FGM).

2.3.3 Basic State & Forcing

The system is forced by both a steady uniform wind stress $\boldsymbol{\tau}_{\text{wind}}$ at the free surface and by a tidal forcing. The latter is described by a Fourier series

$$\mathbf{F}(t) = \sum_{m=-M}^{M} \hat{\mathbf{F}}_m e^{imt}, \tag{2.38}$$

where $\hat{\mathbf{F}}_m$ are the complex amplitudes of the Fourier components, and M is the number of tidal constituents included. The complex amplitudes come in complex conjugate pairs, $\hat{\mathbf{F}}_m = \overline{\hat{\mathbf{F}}_{-m}}$, such that the actual forcing is real valued, corresponding to the prescribed depth-averaged flow values. The basic flow problem and its solution are given in 2.8.1.

The basic state bed load and suspended load transport formulation and solution are given in 2.8.2. In the basic state there is no divergence of bed load and suspended load sediment transport, hence there is no tidally-averaged bed evolution.

2.3.4 Perturbed State

The solution method for the perturbed flow module is given in 2.8.3. The perturbed bed load and suspended load transport formulation and solution procedure are given in 2.8.4. The perturbed bed evolution equation is given by

$$\frac{\partial h_1}{\partial t_{\text{m}}} + \mu_{\text{b}} \boldsymbol{\nabla}_{\text{h}} \cdot \langle \mathbf{q}_{\text{b},1} \rangle_{\text{t}} + \mu_{\text{s}} \boldsymbol{\nabla}_{\text{h}} \cdot \langle \mathbf{q}_{\text{s},1} \rangle_{\text{t}} = 0, \tag{2.39}$$

which can be rewritten as

$$\frac{\partial \breve{h}_1}{\partial t_{\text{m}}} = \gamma \breve{h}_1, \qquad \gamma = \omega - i c_{\text{mig}}. \tag{2.40}$$

Here γ is the complex growth rate depending on the topographic wave vector and on the problem parameters. The real part is the growth rate ω and minus the imaginary part the migration rate c_{mig}. The solution of the bed evolution is given by

$$h_1 = \breve{h}_1^{\text{init}} \exp(\omega t_{\text{m}}) \cos\left(\mathbf{k} \cdot \mathbf{x}_{\text{h}} - c_{\text{mig}} t_{\text{m}}\right), \tag{2.41}$$

where $\breve{h}_1^{\text{init}}$ is the initial perturbation amplitude. It describes exponential growth (or decay) and migration.

2.3.5 Contributions to the complex growth rate

To investigate the mechanisms responsible for the sand wave dynamics, it is useful to identify the various contributions to the complex growth rate. It is the sum of the complex growth rates due to bed load and suspended load, according to

$$\gamma = \gamma_{\text{b}} + \gamma_{\text{s}}. \tag{2.42}$$

In turn, the complex bed load growth rate γ_b can be written as

$$\gamma_\mathrm{b} = \gamma_\mathrm{b,fe} + \gamma_\mathrm{b,se}, \tag{2.43}$$

which consists of the contributions due to the perturbed flow $\gamma_\mathrm{b,fe}$, termed the flow effect, and the slope effect $\gamma_\mathrm{b,se}$. These contributions are given by

$$\gamma_\mathrm{b,fe} = \frac{-i\mathbf{k}\mu_\mathrm{b}}{\breve{h}_1} \cdot \left\langle \left\langle |\boldsymbol{\tau}_\mathrm{cw,0}|^{\beta_\mathrm{b}} \left(\frac{\breve{\boldsymbol{\tau}}_1}{|\boldsymbol{\tau}_\mathrm{cw,0}|} + (\beta_\mathrm{b}-1)\frac{\boldsymbol{\tau}_\mathrm{cw,0}\cdot\breve{\boldsymbol{\tau}}_1}{|\boldsymbol{\tau}_\mathrm{cw,0}|^3}\boldsymbol{\tau}_\mathrm{cw,0} \right) \right\rangle_\mathrm{w} \right\rangle_\mathrm{t}, \tag{2.44}$$

$$\gamma_\mathrm{b,se} = -\mu_\mathrm{b} \left\langle \left\langle |\boldsymbol{\tau}_\mathrm{cw,0}|^{\beta_\mathrm{b}} \lambda \right\rangle_\mathrm{w} \right\rangle_\mathrm{t}, \tag{2.45}$$

where $\breve{\boldsymbol{\tau}}_1$ is the complex amplitude as defined in 2.8.3. The complex suspended load growth rate γ_s is given by

$$\gamma_\mathrm{s} = \gamma_{\mathrm{s,c_1 u_0}} + \gamma_{\mathrm{s,c_0 u_1}} + \gamma_{\mathrm{s,h_1 c_0 u_0}}, \tag{2.46}$$

which is a sum of three contributions: (i) $\gamma_{\mathrm{s,c_1 u_0}}$ the complex growth rate due to the perturbed sediment concentration, (ii) $\gamma_{\mathrm{s,c_0 u_1}}$ the complex growth rate due to the perturbed flow and (iii) $\gamma_{\mathrm{s,h_1 c_0 u_0}}$ the complex growth rate due to the perturbed bed. These three contributions are given by

$$\gamma_{\mathrm{s,c_1 u_0}} = \frac{-i\mathbf{k}\mu_\mathrm{s}}{\breve{h}_1} \cdot \left\langle \int_{-1}^{0} \breve{c}_1 \mathbf{u}_0 dz \right\rangle_\mathrm{t}, \tag{2.47}$$

$$\gamma_{\mathrm{s,c_0 u_1}} = \frac{-i\mathbf{k}\mu_\mathrm{s}}{\breve{h}_1} \cdot \left\langle \int_{-1}^{0} c_0 \breve{\mathbf{u}}_1 dz \right\rangle_\mathrm{t}, \tag{2.48}$$

$$\gamma_{\mathrm{s,h_1 c_0 u_0}} = i\mathbf{k}\mu_\mathrm{s} \cdot \langle c_0 \mathbf{u}_0 |_{z=-1} \rangle_\mathrm{t}, \tag{2.49}$$

respectively. Here $\breve{c}_1$ and $\breve{\mathbf{u}}_1$ are the complex amplitudes as defined in 2.8.3.

2.3.6 Dimensional model output

The wavelength L^*, orientation θ, growth rate ω^* and migration rate c^*_mig of a mode $\mathbf{k}^*$ are given by

$$\begin{array}{ll} L^* = \frac{2\pi}{K^*}, & \theta = \tan^{-1}(k^*_y/k^*_x), \\ \omega^* = \omega/T^*_m, & c^*_\mathrm{mig} = c_\mathrm{mig}/(T^*_m K^*). \end{array} \tag{2.50}$$

In Section 2.4, the results are shown in dimensional form. This is because in the scaling procedure the morphological time scale, given in Eq.(2.20), is dependent on the topographic length scale $1/K^*$. This dependency results in a difference when determining the FGM by either the dimensional or by the dimensionless growth rate. Hence we choose to present the results in dimensional form.

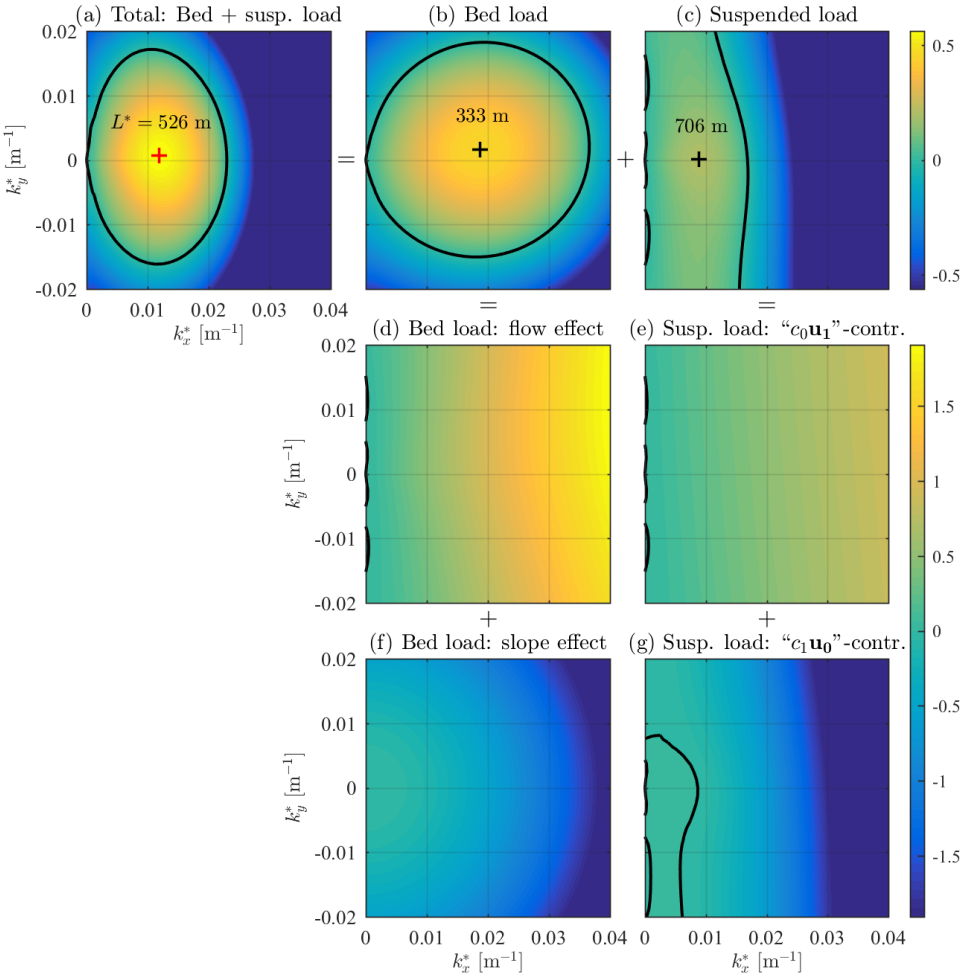

Figure 2.4: The growth rate [yr^{-1}] as function of the topographic wave numbers k_x^* and k_y^* for the fair weather reference condition. The total growth rate (a) is the sum of the growth rates due to bed load (b) and suspended load (c). The bed load growth rate is the sum of two contributions: (d) the flow effect and (f) the slope effect. The suspended load growth rate is the sum of two contributions: (e) a "$c_0\mathbf{u}_1$"-contribution due to perturbed flow and basic concentration and (g) a "$c_1\mathbf{u}_0$"-contribution. Note that the third contribution in Eq.(2.49) does not affect growth. The thick black lines denote the zero growth contours. The + denotes the FGM. The red + in (a) is the fixed mode used to investigate the influence of wind and wave processes.

2.4 Results

2.4.1 Reference situation: tidal currents only

To investigate the influence of storm-related processes on sand wave dynamics, a fair weather reference case is chosen, which includes tidal flow only and leaves out any storm process. For simplicity, a symmetric M2 tidal current is imposed, such that the migration rate of any bed perturbation is zero. The parameters chosen for this reference case are shown in Table 2.1. The growth rate, as a function of the topographic wave numbers k_x^* and k_y^*, is shown in Figure 2.4, in which (a) the total growth rate is the sum of the contributions of (b) bed load and (c) suspended load. In turn, the contributions to the growth rate due to bed load are given by the sum of (d) the flow effect, which is the growing mechanism, and (f) the slope effect which is the decaying mechanism. The contributions of the growth rate due to suspended load are given by the sum of (e) the flow effect, which is the growing mechanism, and (g) the concentration effect, which is the decaying mechanism. The FGM is indicated by a +. The FGM based on both bed and suspended load has the following characteristics: wavelength $L^* = 526$ m, orientation $\theta = 3.0°$, growth rate $\omega^* = 0.56$ yr^{-1} and migration rate $c^*_{\mathrm{mig}} = 0$ $\mathrm{m\,yr}^{-1}$.

2.4.2 Individual process effects

We investigate the effect of waves and wind for bed load and suspended load transport separately. In doing so, we fix the topographic wave vector to that of the fastest growing mode, indicated by the red + in Figure 2.4(a), i.e. taking $L^* = 526$ m and $\theta = 3.0°$ as the fixed mode throughout this section.

Wind waves

The effect of wind waves is shown in Figure 2.5 for varying wave height H^*_{wave} and wave angle θ_{wave}. As pointed out in Section 2.2.2, our model cannot distinguish between waves propagating in opposite directions, so we need to vary θ_{wave} between $-90°$ and $90°$ only. We will first focus on the effect of waves on the bed load growth rate contribution, shown in Figure 2.5(b), which is the sum of two contributions: 2.5(c) the perturbed flow effect in Eq.(2.44) and 2.5(d) the bed slope effect in Eq.(2.45). For increasing wave height the growth rate decreases, and eventually becomes negative. As wave action increases, the decrease of the slope effect outcompetes the increase of the flow effect. Waves thus decrease the growth rate and in particular when they propagate in a direction roughly parallel to the sand wave crest ($\theta_{\mathrm{wave}} = 90°$). The wave angle dependency appears to be strongest in the flow effect. When using $\beta_{\mathrm{b}} = 2$ (not shown) the wave angle dependency is purely in the flow effect. For the more generally accepted value of $\beta_{\mathrm{b}} = 1.5$, as used in the presented results, the wave angle dependence is still predominantly in the flow effect.

Let us now focus on the effect of waves on the suspended load growth rate contribution, shown in Figure 2.5(e), which is the sum of the two contributions: (f) the perturbed flow and (g) perturbed sediment concentration. The third contribution,

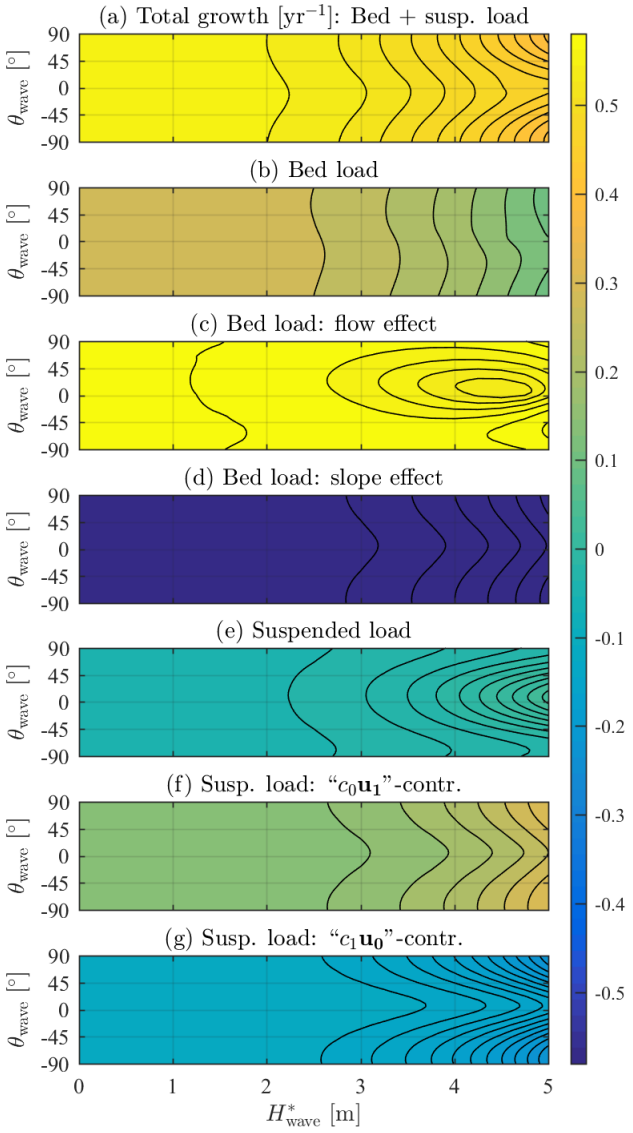

Figure 2.5: The growth rate [yr^{-1}] of the fixed mode as a function of wave height and angle. The total growth rate (a) is the sum of two transport modes: (b) bed load and (e) suspended load. The bed load growth rate is the sum of two contributions: (c) the growth rate due to the flow effects and (d) the bed slope effect. Likewise, the suspended load growth rate is the sum of three contributions: (f) the perturbed flow effect, (g) the perturbed sediment concentration effect, and the perturbed bed contribution. The last does not affect growth and therefore not shown. The thick black line denotes the zero growth contour.

$\gamma_{s,h_1 c_0 \mathbf{u}_0}$, does not contribute to the growth rate and only contributes to migration, which is zero in this symmetric example. The growth rate due to suspended load increases with increasing wave amplitude because the perturbed flow effect is stronger than the perturbed concentration effect. The suspended load growth rate behaves roughly similar to the bed load flow effect growth rate contribution, in Figure 2.5(c).

The decreasing effect of waves on the bed load induced growth rate is larger than the increasing effect of the suspended load growth rate. Hence waves decrease the total growth rate. Furthermore, it should be noted that adding waves does not break the symmetry of this example, so migration rates remain zero.

Wind-driven flow

The effect of wind-driven flow on the growth and migration rate for varying wind speed, $U^*_{\text{wind}} = |\mathbf{U}^*_{\text{wind}}|$, and wind angle, θ_{wind} are shown in Figure 2.6.

We will first focus on the effect of wind-driven flow on the growth and migration rate due to bed load transport, for which the growth rate is shown in Figure 2.6(c) and the migration rate in (d). The growth rate due to the flow effect, shown in Fig.2.6(e), either increases or decreases with increasing wind speed. The growth rate slightly decreases for intermediate wind speed. For higher wind speeds the growth rate increases for wind roughly perpendicular to the tidal currents ($\theta_{\text{wind}} \approx \pm 90°$) increases the growth rate, while wind parallel to the tidal flow ($\theta_{\text{wind}} \approx 0°, 180°$) further reduces the growth rates. Due to the Coriolis effect the wind-driven flow component experiences Ekman veering through the water column. When the wind is directed under an angle with respect to the tidal current, nearly perpendicular in this example, such that the near-bed flow is directed in the direction of the tidal flow, the growth rate is enhanced. However, when the wind is directed such that the wind-driven near-bed flow is directed perpendicular to the tidal flow, $\theta_{\text{wind}} \approx 0°$ in this example, the growth rate is reduced. The effect of wind-driven flow on the slope effect is shown in Fig.2.6(g). The slope effect becomes stronger with increasing wind speed and depends on the wind direction. The slope effect and flow effect together, results in a small decrease for intermediate wind speeds, and for larger wind speeds in an increase of the bed load growth rate once the near-bed wind-driven flow is in the direction of the tidal current, and in a reduction of the growth rate when the wind-driven near-bed flow is tangential to the tidal current. The effect of wind-driven flow on the migration rate due to bed load is shown in Figure 2.6(d). This migration is purely the flow effect contribution (f), since the slope effect (h) does not contribute to migration. Migration occurs when the symmetry of the tidal current is breached by the wind-driven flow. Also the wind direction at which maximum migration occurs and the magnitude of the maximum migration is affected by the Coriolis effect due to the veering of the flow.

Let us now focus on the influence of wind-driven flow on the growth and migration rate due to suspended load transport, shown in Figures 2.6(i) and (j) respectively. The growth rate due to suspended load decreases with increasing wind speed. The angle at which the growth rate is reduced most is approximately $\theta_{\text{wind}} = 45°, -135°$, which is a different wind angle at which the bed load growth rate was reduced most. The

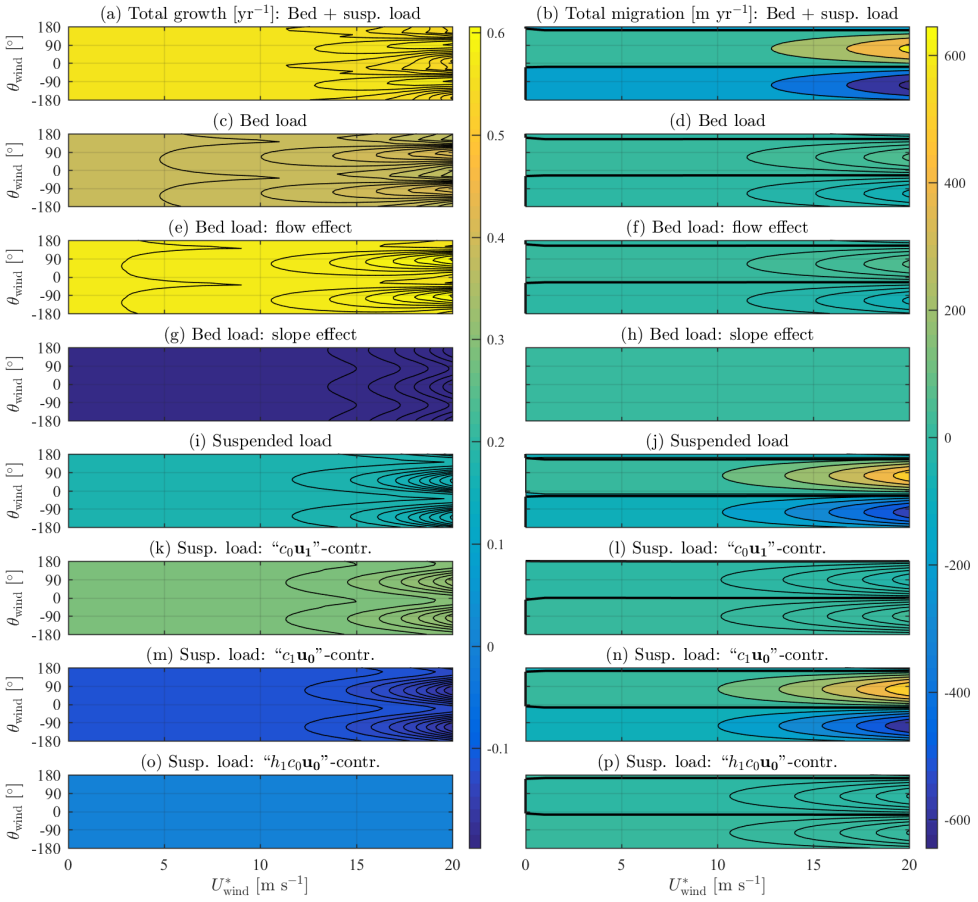

Figure 2.6: The growth rate (left) and the migration rate (right) contribution of the fixed mode as a function of wind speed and angle. The top row shows the total, the plots below show the various contributions. The thick black line denotes the zero growth or migration contour.

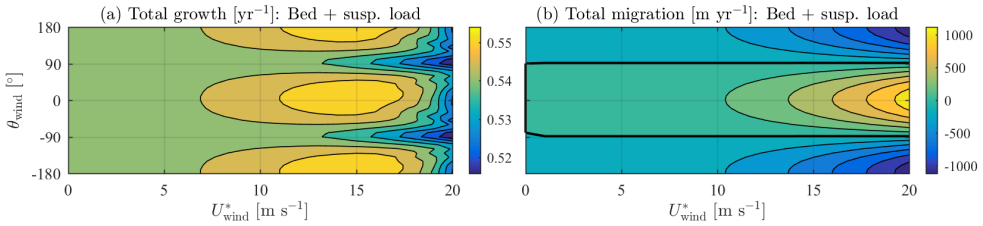

Figure 2.7: (a) The total growth rate [yr^{-1}] and (b) migration rate [$\mathrm{m\,yr}^{-1}$] of the fixed mode as a function of wind speed and angle, but now without the Coriolis effect ($\phi = 0°$). The thick black line denotes the zero migration contour.

migration due to suspended load is similar to that due to bed load. However, the migration rates due to suspended load are much larger than those of bed load transport. The growth rate due to the perturbed flow effect, shown in Fig.2.6(k), increases with increasing wind speeds. The increase in growth rate occurs at wind directions nearly perpendicular to the tidal current. Migration due to the perturbed flow effect, shown in Figure 2.6(l), has a small counteracting contribution to the total migration rate. The perturbed concentration contribution to the growth rate decreases with increasing wind speed, particularly for wind directed perpendicular to the tidal currents. The total migration rate is dominated by the perturbed concentration contribution of suspended load (n). Finally, the perturbed bed contribution, which does not affect the growth rate (o), has a small counteracting contribution to the total migration rate (p).

The effect of wind on the total growth rate is the sum of the alternating increasing and decreasing growth rate of bed load and the decreasing growth rate due to suspended load, which results in a growth rate that is either slightly increased for wind perpendicular to the tidal current or decreased for wind directed parallel to the tidal current. The total migration rate due to wind-driven flow is predominantly generated by the perturbed concentration contribution (n).

The wind-driven flow mechanism has been shown in Fig.2.6 for the reference situation where the Coriolis effect has been included ($\phi = 52°$). Figure 2.7 shows the total growth and migration rate for the same wind experiment, but now without the Coriolis effect ($\phi = 0°$). Without the Coriolis effect qualitatively the same mechanisms are observed. Two major differences are observed: (i) the magnitude of the migration due to wind-driven flow increased and (ii) the angle shift between the wind direction and the direction at which the wind-driven flow effects are strongest vanishes without the Coriolis effect, as there is no longer veering of the flow. The wind-induced decrease in growth rate due to suspended load dominates the alternating increase and decrease in growth rate due to bed load for large wind velocities. The Coriolis effect can thus change the subtle balance between the various processes.

2.4.3 Wind and waves combined

Now the combined effect of wind and waves on the growth and migration rates as function of the topographic wave numbers k_x^* and k_y^* is analyzed. Figure 2.8 shows the growth and migration rates for four conditions: (a) fair weather reference (as already plotted in Figure 2.4(a)), (b) waves, (c,e) wind and (d,f) both wind and waves. The wind and wave angles are both parallel to the tide ($\theta_{\text{wind}} = \theta_{\text{wave}} = 0°$). The wind speed is $U^*_{\text{wind}} = 20\ \text{m}\,\text{s}^{-1}$ and the wave height is $H^*_{\text{wave}} = 5$ m.

The mechanism responsible for the reduction in growth rate under wave action for the fixed mode, the fair weather FGM, has been described in Section 2.4.2. The growth rate of the mode corresponding to the fair weather FGM is greatly reduced in growth rate as a results of wave action. However, the effect of storms on the growth rate is dependent on the mode. The slope effect is more important for bed forms with small wavelengths. Therefore, especially small wavelength perturbations (large $|\mathbf{k}^*|$) experience a reduction in growth rate by wave action. Hence the FGM for the waves condition, shown in Fig.2.8(b), has a longer wavelength and a smaller growth rate compared to the fair weather condition (a).

Wind in the direction tangential to the tidal current results in a reduction of the growth rate of the fixed mode due to the veering of the wind-driven flow due to Coriolis, as was already shown in Figure 2.6(a). Wind is able to enhance the growth rate for angles roughly perpendicular to the wind driven flow, for the used set of parameters. The modes with their orientation roughly perpendicular to the tidal flow, now show an increase in growth rate. This is caused by the rotated wind-driven flow near the bed. As seen previously, wind-driven flow breaks the symmetry in the tidal current in this example and hence induces migration. The maximum migration is observed for modes that are oriented in the direction of the veered near-bed flow. Hence the FGM in this example does not experience the maximum possible growth rate for this wind speed.

The combined effect of waves and wind reduces the growth rate, and increases the wavelength of the FGM even further. Waves alone do not induce migration, but they enhance migration that is induced by wind. Although not shown in the examples presented here, migration due to residual currents (M0+M2) and tidal asymmetry (M2+M4) is enhanced by wave action, as well.

Figure 2.9 shows the growth and migration rates for waves and wind perpendicular to the tide ($\theta_{\text{wind}} = \theta_{\text{wave}} = 90°$). Perpendicular waves decrease the growth rate, and increase the wavelength of the FGM even further than tangential waves do. Wind perpendicular to the tide increases the growth rate of the FGM, and slightly increases its wavelength. The combined effect of waves and wind perpendicular to the tide results in a slightly smaller wavelength and larger growth rate compared to the combined effect of waves and wind tangential to the tide.

2.4.4 Dependencies of the FGM on wind and wave angle

Waves and wind have their individual and combined effect on the properties of bed forms. The FGM thus changes as function of the chosen wind and wave conditions.

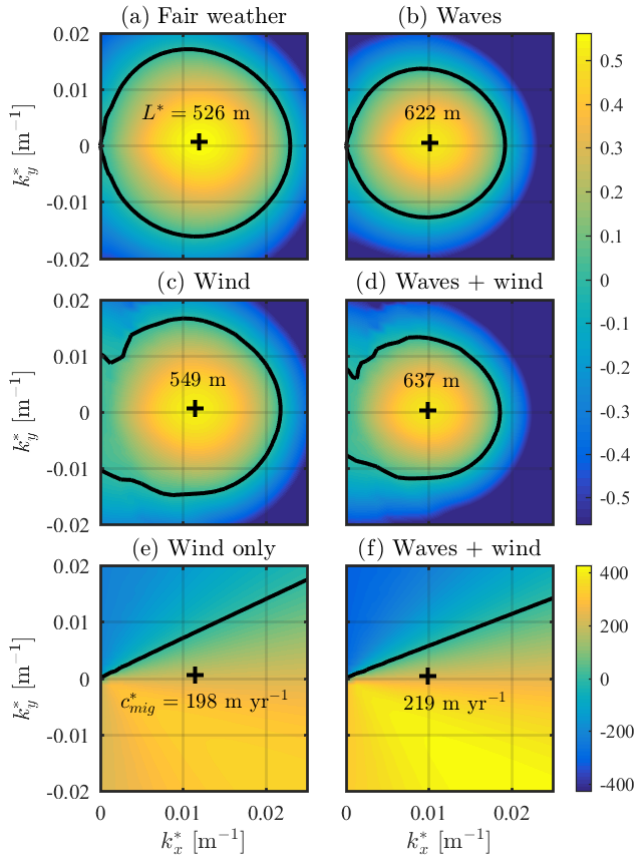

Figure 2.8: The total growth (a–d) [yr^{-1}] and migration rates (e–f) [m yr^{-1}] for four different storm conditions: no wind nor waves (a), waves (b), wind (c,e) and wind and waves (d,f). The wind and wave angle are $\theta_{\text{wave}} = \theta_{\text{wind}} = 0^\circ$, i.e. **parallel** to the tide.

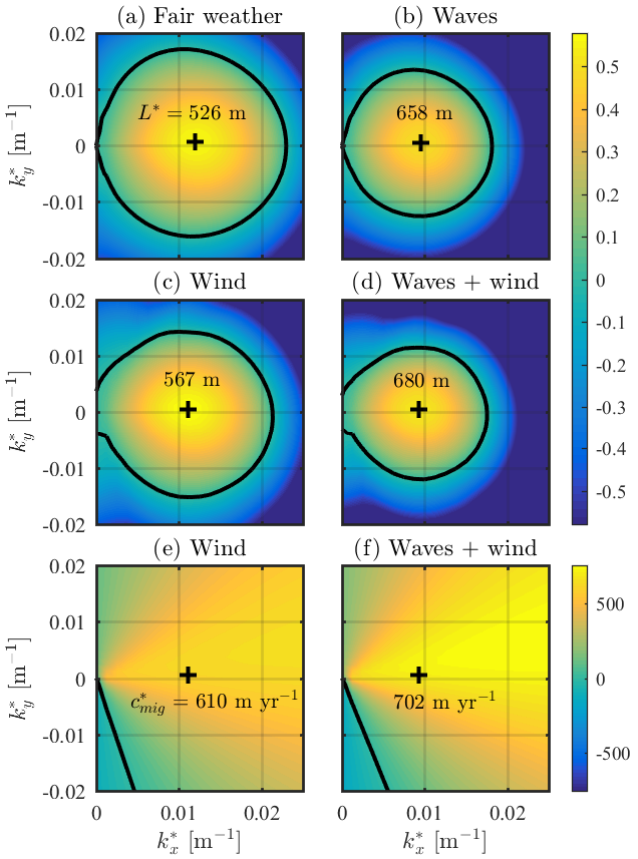

Figure 2.9: The total growth (a–d) [yr^{-1}] and migration rates (e–f) [m yr^{-1}] for four different storm conditions: no wind nor waves (a), waves (b), wind (c,e) and wind and waves (d,f). The wind and wave angle are $\theta_{\text{wave}} = \theta_{\text{wind}} = 90^\circ$, i.e. **perpendicular** to the tide.

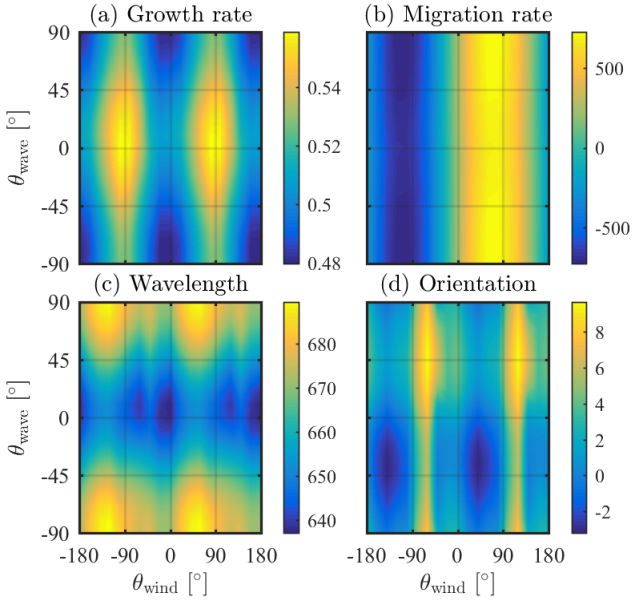

Figure 2.10: The FGM properties, (a) growth rate [yr^{-1}], (b) migration rate [$\text{m}\,\text{yr}^{-1}$], (c) wavelength [m] and (d) orientation [°] as function of the wave and wind angle. Both bed and suspended load are included.

Figure 2.10 shows the FGM properties as function of wave and wind angle. The wave height and wind speed are $H^*_{\text{wave}} = 5$ m and $U^*_{\text{wind}} = 20\ \text{m}\,\text{s}^{-1}$, respectively. The maximum FGM growth rate is approximately equal to the growth rate of the fair weather FGM. For all other wave and wind angle combinations the growth rate is less than the fair weather FGM growth rate. Also these growth rates all correspond to bed forms that have longer wavelengths, and sometimes fairly large angles with respect to the tidal current.

2.5 Discussion

2.5.1 Approach

Importantly, we investigated storm processes in the formation stage, implying that we cannot model properties of fully grown sand waves such as migration rates, heights and shape which require a nonlinear approach. Nevertheless, our results in the linear regime suggest that waves and wind-driven flow are also important processes in nonlinear sand wave models.

2.5.2 Rescaling of the perturbed problem

As pointed out in Section 2.3.1, the water depth H^* is not an appropriate vertical length scale for the perturbed problem. In the scaling of the surface elevation we already mentioned that there are two scales at play in the surface elevation term. Similarly there are two vertical length scales at play in the hydrodynamic problem. Firstly, the vertical scale of the basic state flow problem is indicated by the Stokes depth $\sqrt{2A_{\mathrm{v}}^*/\sigma^*} = \mathcal{O}(H^*)$. Secondly, the vertical length scale of the perturbed flow problem is much smaller as the vertical velocity profile needs time to adapt to the changing bed topography as the velocity profile is advected. The difference in the vertical length scale between the basic state and the perturbed state is induced by the difference in time scales. The vertical profile in the basic state flow problem adapts at the tidal time scale $1/\sigma^*$, whereas the vertical profile of the perturbed flow problem adapts at the advective time scale $1/(U^*K^*)$. The ratio of the tidal and advective time scales is expressed by the Keulegan-Carpenter number $r = U^*K^*/\sigma^* \sim \mathcal{O}(40)$, which is typically large in the perturbed state situation with undulations corresponding to sand waves (see Table 2.2).

The new vertical scale $\tilde{H}^*$ is determined by assuming that the diffusion term in the momentum balance is equally important as the advective and pressure term. This gives $\tilde{H}^* = \sqrt{A_{\mathrm{v}}^*/(U^*K^*)}$, which is used in our rescaled vertical coordinate $z^* = \tilde{H}^*\tilde{z}$, the vertical velocity $w^* = U^*\tilde{H}^*K^*\tilde{w}$ and the perturbed bed $h^* = \tilde{H}^*\tilde{h}$. Here tildes denote rescaled quantities. We now obtain the following hydrodynamic model, which would replace Eqs.(2.23)–(2.24), for the perturbed flow problem:

$$\boldsymbol{\nabla}_{\mathrm{h}} \cdot \mathbf{u}_{\mathrm{h},1} + \frac{\partial \tilde{w}_1}{\partial \tilde{z}} = 0, \tag{2.51}$$

$$\begin{aligned} \frac{1}{r}\frac{\partial \mathbf{u}_{\mathrm{h},1}}{\partial t} + \mathbf{u}_{\mathrm{h},0} \cdot \boldsymbol{\nabla}_{\mathrm{h}}\mathbf{u}_{\mathrm{h},1} + \tilde{w}_1\frac{\partial \mathbf{u}_{\mathrm{h},0}}{\partial \tilde{z}} + \frac{f}{r}\left[\mathbf{e}_z \times \mathbf{u}_1\right]_{\mathrm{h}} = \\ -\boldsymbol{\nabla}_{\mathrm{h}}\zeta_1 + \frac{\partial^2 \mathbf{u}_{\mathrm{h},1}}{\partial \tilde{z}^2}. \end{aligned} \tag{2.52}$$

The corresponding boundary conditions will have to be scaled accordingly. The rescaled problem shows that the inertial and Coriolis effects, which were significant in the basic state, are only small for the perturbed problem, because the Keulegan-Carpenter number, r, is large. Although these two terms are not significant in the perturbed state, the basic state solution still depends on these terms. Hence inertial and Coriolis effect do have their effect on the perturbations, but in an indirect way: via the interactions with the basic state.

2.5.3 Processes

We used a strongly schematized turbulence model, e.g. a constant eddy viscosity combined with a partial-slip condition, we expect that using more sophisticated models will only quantitatively affect the results.

Wind-driven flow is modeled assuming spatially uniform and steady wind, i.e. far away from coastlines or other obstructions. In reality wind-driven flow develops in

time as a response to the spatial and temporal wind conditions. Also, the presence of a coastline will result in a wind set-up due to Ekman transport resulting in a pressure gradient that forces a flow in the opposite direction, which will force the flow to align with the coastline. Therefore, the phase shift due to the Coriolis effect in wind-driven flow may be exaggerated or even reversed compared to situations that are affected by a coastline.

Waves are now parametrically included via linear wave theory, since this captures the most important effect of waves at large water depth, namely the near-bed orbital velocities. Left out processes like wave-current interactions and refraction are likely to have their influence on sand wave dynamics. However, because of the large water depth we do not expect these effects to be large.

2.5.4 Model studies and observations

Our model confirms sand wave migration due to wind-driven flow, which was found earlier by Németh et al. (2002) in a 2DV model assuming wind in the direction of the tidal current and neglecting the Coriolis effect. We extended this by allowing an arbitrary angle of the wind with respect to the tidal current, as well as including the Coriolis effect. Comparing our work to reality remains difficult since sand waves in the field are fully grown, i.e. no small amplitudes, and storm processes are not isolated events between two field measurements. Van Santen et al. (2011) combined a data analysis with a modeling approach, that did not include storm effects. They compared the observed variations in sand wave characteristics at several locations with the modeled sand wave characteristics as function of water depth, tidal amplitude, ellipticity and grain size. To a certain extent sand wave variations are explained by the model parameters. Our work suggests that storms may account for the remaining variation that could not be explained by the parameters in Van Santen et al.'s (2011) analysis.

Morphodynamical models are often calibrated with parameters such as the slope parameter or bed roughness (partial slip in our work). We have identified additional mechanisms that may explain longer wavelength and higher migration rates. Hence calibration of sand wave models without taking into account storm processes, results in correct wavelengths for the calibrated regime, but misses the physical processes of storms.

Based on the modeled effects of specific storm conditions we can say that waves and wind indeed can play a significant role in sand wave dynamics. The presented migration rates are seemingly very large compared to field data. However, storms occur only for a small fraction of the time. Also, one storm may result in a migration that is counteracting the migration due to a previous storm that had another wind direction. Successive field observations show the average dynamics of the sea bed that occurs in between observations. To assess the averaged model effect of storms on sand wave dynamics a statistical approach is required. We leave the impact of a statistically combined wave and wind climate on sand wave dynamics for future research.

2.6 Conclusion

We have presented a new idealized sand wave model that is able to systematically investigate storm related processes on sand wave dynamics in the formation stage. We found that waves decrease the growth rate of sand waves significantly, especially if they propagate perpendicular to the sand wave crest orientation. This wave angle dependency is mainly present in the flow effect, and hardly in the slope effect. Wind waves as modeled herein are unable to induce migration themselves, but they can enhance migration through other mechanisms such as wind-driven flow, residual currents or tidal asymmetry.

Wind-driven flow induces migration because it breaches tidal symmetry. Our model allows to vary the wind direction and to include the Coriolis effect. Without the Coriolis effect, wind parallel to the tidal flow increases the growth rate and causes migration. Perpendicular wind reduces the growth rate and does not induce migration. Including the Coriolis effect causes (*i*) a shift in the angle at which the maximum growth and migration rate occurs and (*ii*) the magnitude of the migration rate reduces. Suspended load is the sum of three contributions: (*i*) the flow effect, which is the growing mechanism and is enhanced by both waves and wind, (*ii*) the perturbed concentration effect, which is a decaying mechanism and a strong contribution to the migration rate that are both enhanced by waves and wind, (*iii*) the perturbed bed contribution, which does not affect growth and counteracts the total migration rate.

Storms tend to reduce growth rates, in a way that favors sand waves with longer wavelengths than those generated during fair weather conditions. Wind-driven flow in combination with waves may result in significant migration rates during storms, that may oppose migration during fair weather. Our model results support the observations by Terwindt (1971), McCave (1971), Fenster et al. (1990), Le Bot et al. (2000) and Ferret et al. (2010), who suggested that storms may be important factors in sand wave dynamics. Given the significance of storm effects on sand wave formation we suggest to further investigate the influence of storms on fully grown sand waves in the nonlinear regime. Furthermore, a statistical approach is required to assess the effect of a given storm climate.

2.7 Acknowledgment

This research is supported by the Dutch Technology Foundation STW, which is part of the Netherlands Organisation for Scientific Research (NWO), and which is partly funded by the Ministry of Economic Affairs. We thank an anonymous reviewer for his/her comments.

2.8 Appendix

2.8.1 Basic flow solution

For a flat bed no horizontal gradients occur and the vertical velocity near the bed is zero. Following from continuity there is no vertical flow: $w_0 = 0$. The basic state of the currents module is given by

$$\frac{\partial \mathbf{u}_{\mathrm{h},0}}{\partial t} + f[\mathbf{e}_z \times \mathbf{u}_0]_{\mathrm{h}} = -\mathbf{F} + A_{\mathrm{v}} \frac{\partial^2 \mathbf{u}_{\mathrm{h},0}}{\partial z^2}. \tag{2.53}$$

The free surface ($z = 0$) boundary conditions are:

$$A_{\mathrm{v}} \frac{\partial \mathbf{u}_{\mathrm{h},0}}{\partial z} = \boldsymbol{\tau}_{\mathrm{wind}}. \tag{2.54}$$

The sea bed ($z = -1$) boundary conditions are:

$$A_{\mathrm{v}} \frac{\partial \mathbf{u}_{\mathrm{h},0}}{\partial z} = S\mathbf{u}_{\mathrm{h},0}. \tag{2.55}$$

Each quantity is described as Fourier series in time:

$$u_0 = \sum_{m=-M}^{M} \hat{u}_{0,m} e^{imt}. \tag{2.56}$$

Here $\hat{u}_{0,m}$ represents the Fourier components of the unknowns of the system in the basic state. The Fourier velocity components $\hat{u}_{0,m}$ and $\hat{v}_{0,m}$ are given by:

$$\hat{u}_{0,m} = \frac{\hat{P_m^+} + \hat{P_m^-}}{2}, \qquad \hat{v}_{0,m} = \frac{\hat{P_m^+} - \hat{P_m^-}}{2i}, \tag{2.57}$$

with rotating components $\hat{P_m^\pm} = A_m^\pm \tau_w^\pm + B_m^\pm F_m^\pm$ in which $F_m^\pm = \hat{F}_{m,x} \pm i\hat{F}_{m,y}$ and $\tau_w^\pm = \tau_{\mathrm{wind},x} \pm i\tau_{\mathrm{wind},y}$ with coefficients:

$$\begin{aligned} A_m^\pm &= \begin{cases} a_m^\pm \cosh(\phi_m^\pm z) + \frac{1}{\phi_m^\pm A_{\mathrm{v}}} \sinh(\phi_m^\pm z) & \text{for } m = 0 \\ 0 & \text{for } m \neq 0 \end{cases}, \\ B_m^\pm &= b_m^\pm \cosh(\phi_m^\pm z) \pm \frac{i}{f \pm m}. \end{aligned} \tag{2.58}$$

Here, $\phi_m^\pm$, $a_m^\pm$ and $b_m^\pm$ are:

$$\begin{aligned} \phi_m^\pm &= \sqrt{i\frac{m \pm f}{A_{\mathrm{v}}}}, \\ a_m^\pm &= \frac{\frac{1}{\phi_m^\pm A_{\mathrm{v}}} \left[S \sinh(-\phi_m^\pm) - A_{\mathrm{v}} \phi_m^\pm \cosh(-\phi_m^\pm)\right]}{A_{\mathrm{v}} \phi_m^\pm \sinh(-\phi_m^\pm) - S \cosh(-\phi_m^\pm)}, \\ b_m^\pm &= \frac{\pm \frac{iS}{(f \pm m)}}{A_{\mathrm{v}} \phi_m^\pm \sinh(-\phi_m^\pm) - S \cosh(-\phi_m^\pm)}. \end{aligned} \tag{2.59}$$

Note that when $m = f$ the basic flow problem becomes parabolic, and yields a different solution. The basic state shear stress due to both currents and waves is

$$\boldsymbol{\tau}_{\mathrm{cw},0} = A_{\mathrm{v}} \frac{\partial \mathbf{u}_{\mathrm{h},0}}{\partial z} + \boldsymbol{\tau}_{\mathrm{w}}. \tag{2.60}$$

2.8.2 Basic state bed and suspended load transport

The basic state bed load transport is

$$\mathbf{q}_{\mathrm{b},0} = \left\langle |\boldsymbol{\tau}_{\mathrm{cw},0}|^{\beta_{\mathrm{b}}-1} \boldsymbol{\tau}_{\mathrm{cw},0} \right\rangle_{\mathrm{w}} \tag{2.61}$$

The basic state advection-diffusion equation for suspended sediment concentration, given by

$$\frac{\partial c_0}{\partial t} = A_{\mathrm{v}} \frac{\partial^2 c_0}{\partial z^2} + w_{\mathrm{s}} \frac{\partial c_0}{\partial z} \tag{2.62}$$

with its boundary conditions at the free surface ($z = 0$), given by

$$A_{\mathrm{v}} \frac{\partial c_0}{\partial z} + w_{\mathrm{s}} c_0 = 0 \tag{2.63}$$

and at the sea bed ($z = -1$):

$$A_{\mathrm{v}} \frac{\partial c_0}{\partial z} + w_{\mathrm{s}} c_{\mathrm{ref},0} = 0 \tag{2.64}$$

The basic state reference concentration is:

$$c_{\mathrm{ref},0} = \left\langle |\boldsymbol{\tau}_{\mathrm{cw},0}|^{\beta_{\mathrm{s}}} \right\rangle_{\mathrm{w}} \tag{2.65}$$

The solution of the basic state advection-diffusion equations for suspended sediment concentration (2.62)–(2.64) is:

$$c_0 = \sum_{m=-M}^{M} \hat{c}_{0,m} e^{imt}. \tag{2.66}$$

Here $\hat{c}_{0,m}$ are:

$$\hat{c}_{0,m} = \left[D_m e^{\lambda_m^+ z} + E_m e^{\lambda_m^- z} \right] w_{\mathrm{s}} \hat{c}_{\mathrm{ref},0,m} \tag{2.67}$$

D_m, E_m and $\lambda_m^{\pm}$ are:

$$D_m = \frac{A_{\mathrm{v}} \lambda_m^- + w_{\mathrm{s}}}{(A_{\mathrm{v}} \lambda_m^+ + w_{\mathrm{s}}) A_{\mathrm{v}} \lambda_m^- e^{-\lambda_m^-} - (A_{\mathrm{v}} \lambda_m^- + w_{\mathrm{s}}) A_{\mathrm{v}} \lambda_m^+ e^{-\lambda_m^+}} \tag{2.68}$$

$$E_m = \frac{-A_{\mathrm{v}} \lambda_m^+ - w_{\mathrm{s}}}{(A_{\mathrm{v}} \lambda_m^+ + w_{\mathrm{s}}) A_{\mathrm{v}} \lambda_m^- e^{-\lambda_m^-} - (A_{\mathrm{v}} \lambda_m^- + w_{\mathrm{s}}) A_{\mathrm{v}} \lambda_m^+ e^{-\lambda_m^+}} \tag{2.69}$$

$$\lambda_m^{\pm} = \frac{-w_{\mathrm{s}} \pm \sqrt{w_{\mathrm{s}}^2 + 4imA_{\mathrm{v}}}}{2A_{\mathrm{v}}}. \tag{2.70}$$

Since Eq.(2.65) is nonlinear, $\hat{c}_{\mathrm{ref},0,m}$ is approximated by Fast Fourier Transform of a discrete time series of $c_{\mathrm{ref},0}$.

2.8.3 Perturbed flow

The perturbed topographic bed consist of a single spatial Fourier mode $e^{i\mathbf{k}\cdot\mathbf{x}_\mathrm{h}}$. The horizontal structure of the hydrodynamic system is therefore described using this horizontal Fourier mode

$$\varphi_1 = \frac{1}{2}\breve{\varphi}_{1,m}e^{i\mathbf{k}\cdot\mathbf{x}_\mathrm{h}} + c.c., \tag{2.71}$$

where $\breve{\varphi}_1$ is represented as a finite number of Fourier components in time, given by

$$\breve{\varphi}_1 = \sum_{m=-M}^{M} \hat{\varphi}_{1,m}e^{imt}. \tag{2.72}$$

In the shown results, where the system is forced with a symmetric M2 tidal current, the Fourier series is truncated at $M = 4$ to allowing several higher harmonics which are generated in the non-linear advection terms. Higher truncation numbers did not show significant changes to the results. The hydrodynamic problem per temporal Fourier component is then written as:

$$i\mathbf{k}\cdot\hat{\mathbf{u}}_{\mathrm{h},1,m} + \frac{\mathrm{d}\hat{w}_{1,m}}{\mathrm{d}z} = 0, \tag{2.73}$$

$$\begin{aligned} im\hat{\mathbf{u}}_{\mathrm{h},1,m} + r\sum_{n=-M}^{M}\left[i\hat{\mathbf{u}}_{\mathrm{h},0,n}\cdot\mathbf{k}\hat{\mathbf{u}}_{\mathrm{h},1,m-n} + \hat{w}_{1,n}\frac{\mathrm{d}\hat{\mathbf{u}}_{\mathrm{h},0,m-n}}{\mathrm{d}z}\right] \\ + f\left[\mathbf{e}_z\times\hat{\mathbf{u}}_{1,m}\right]_\mathrm{h} = -i\mathbf{k}\hat{\zeta}_{1,m} + A_\mathrm{v}\frac{\mathrm{d}^2\hat{\mathbf{u}}_{\mathrm{h},1,m}}{\mathrm{d}z^2}, \end{aligned} \tag{2.74}$$

with boundary conditions at $z = 0$:

$$\hat{w}_{1,m} = 0, \quad \frac{\mathrm{d}\hat{\mathbf{u}}_{\mathrm{h},1,m}}{\mathrm{d}z} = 0, \tag{2.75}$$

and boundary conditions at $z = -1$:

$$\begin{aligned} \hat{w}_{1,m} &= i\hat{\mathbf{u}}_{\mathrm{h},0,m}\cdot\mathbf{k}\breve{h}_1, \\ A_\mathrm{v}\left[\frac{\mathrm{d}\hat{\mathbf{u}}_{\mathrm{h},1,m}}{\mathrm{d}z} + \breve{h}_1\frac{\mathrm{d}^2\hat{\mathbf{u}}_{\mathrm{h},0,m}}{\mathrm{d}z^2}\right] &= S\left[\hat{\mathbf{u}}_{\mathrm{h},1,m} + \breve{h}_1\frac{\mathrm{d}\hat{\mathbf{u}}_{\mathrm{h},0,m}}{\mathrm{d}z}\right]. \end{aligned} \tag{2.76}$$

The above system of ordinary differential equations is a boundary value problem, i.e. at neither boundary of the domain all quantities are known. Hence, some quantities require initial guesses in order to start numerical integration (4th order Runge-Kutta) through the water column towards the other boundary condition. At the other boundary the residuals of the boundary conditions are evaluated to indicate weather the initial values were properly chosen. The procedure is repeated with other initial values until sufficient linear independent combinations have been chosen to solve the linear system to obtain the correct initial values such that the boundary conditions at both boundaries are met. This procedure is known as the shooting method.

The perturbed currents induced bed shear stress is computed via:

$$\boldsymbol{\tau}_1 = A_\mathrm{v}\left[\frac{\partial\mathbf{u}_1}{\partial z} + h_1\frac{\partial^2\mathbf{u}_0}{\partial z^2}\right]. \tag{2.77}$$

2.8.4 Perturbed state bed load and suspended load transport

The perturbed bed load transport formula is given by

$$\mathbf{q}_{\mathrm{b},1} = \left\langle |\boldsymbol{\tau}_{\mathrm{cw},0}|^{\beta_\mathrm{b}} \left(\frac{\boldsymbol{\tau}_1}{|\boldsymbol{\tau}_{\mathrm{cw},0}|} + (\beta_\mathrm{b} - 1) \frac{\boldsymbol{\tau}_{\mathrm{cw},0} \cdot \boldsymbol{\tau}_1}{|\boldsymbol{\tau}_{\mathrm{cw},0}|^3} \boldsymbol{\tau}_{\mathrm{cw},0} - \lambda \boldsymbol{\nabla}_\mathrm{h} h_1 \right) \right\rangle_\mathrm{w} \tag{2.78}$$

The perturbed suspended sediment module becomes:

$$\frac{\partial c_1}{\partial t} + r \left[\mathbf{u}_{\mathrm{h},0} \cdot \boldsymbol{\nabla}_\mathrm{h} c_1 + w_1 \frac{\partial c_0}{\partial z} \right] - w_\mathrm{s} \frac{\partial c_1}{\partial z} = A_\mathrm{v} \frac{\partial^2 c_1}{\partial z^2} \tag{2.79}$$

The boundary conditions at $z = 0$ and $z = -1$, are:

$$\begin{aligned} &- A_\mathrm{v} \frac{\partial c_1}{\partial z} - w_\mathrm{s} c_1 = 0 \\ &- A_\mathrm{v} \frac{\partial c_1}{\partial z} - h_1 A_\mathrm{v} \frac{\partial^2 c_0}{\partial z^2} + r w_1 c_0 - w_\mathrm{s} c_{\mathrm{ref},1} = 0 \end{aligned} \tag{2.80}$$

The perturbed reference concentration is given by

$$c_{\mathrm{ref},1} = \left\langle \beta_\mathrm{s} |\boldsymbol{\tau}_{\mathrm{cw},0}|^{\beta_\mathrm{s}-1} \frac{\boldsymbol{\tau}_{\mathrm{cw},0} \cdot \boldsymbol{\tau}_1}{|\boldsymbol{\tau}_{\mathrm{cw},0}|} \right\rangle_\mathrm{w} \tag{2.81}$$

The perturbed advection-diffusion problem is solved similarly to the perturbed hydrodynamic problem, using Fourier components and the shooting method.

Chapter 3

Modeling wave and wind climate effects on tidal sand wave dynamics: a North Sea case study*

Abstract

To obtain site-specific wave and wind climate averaged sand wave dynamics, we combine an idealized linear stability model with 20 years of wave and wind data taken from the Euro Platform in the North Sea. The model output results in a wave and wind climate-averaged growth and migration rate. The results show that waves and wind affect particularly migration and to a much smaller extent the growth rate. Seasonal variations in wave and wind conditions during winter and summer periods result in seasonal variations in sand wave dynamics, in particular during winter the migration rate is larger, the growth rates are lower and the preferred wavelength is larger compared to summer. Medium wave and wind conditions are responsible for two thirds of the migration rate, while these conditions occur roughly only one third of the time. Extreme wave and wind conditions result in only a moderate contribution to the migration rate. Furthermore, we see a seasonal variation in migration as well as reasonable correlation with observed migration rates for the intervals between surveys in the period 1996-2010. Our work shows that storms are able to affect sand wave migration, and cause variability in migration rate.

*This chapter has been submitted as Campmans, G.H.P., P.C. Roos, E.P.W.J. Schrijen, and S.J.M.H. Hulscher (subm.) Modeling wave and wind climate effects on tidal sand wave dynamics: a North Sea case study.

3.1 Introduction

Tidal sand waves are rhythmic bed forms observed in tidally dominated shallow seas all around the world. They have typical wavelengths of hundreds of meters and heights of several meters (Terwindt, 1971; Van Dijk and Kleinhans, 2005, also see Fig.3.1a). These large bed forms are dynamic, e.g. showing migration and growth. Because of their dynamical behavior in combination with their large dimensions, they interfere with various human activities in shallow seas. For example, sand waves may pose a hazard to navigation, pipelines, cables as well as the foundation of wind farms and gas/oil platforms (Németh et al., 2003). Therefore, an accurate understanding of sand wave dynamics is required.

Sand waves have been studied both using observations and from a modeling perspective. Hulscher (1996) explained sand waves as a free instability of the sandy seabed subject to tidal flow. Tidally averaged circulation cells tend to move sediment towards the crests, while gravity favors sediment transport towards the troughs. Observational studies show that storms, which occur on a much more irregular basis compared to the tidal flow, also affect sand wave dynamics. In particular, sand wave heights are reduced during stormy periods (Terwindt, 1971; Houthuys et al., 1994; Van Dijk and Kleinhans, 2005) and migration speed or even direction may change (Harris, 1989; Fenster et al., 1990; Le Bot et al., 2000).

To better understand sand wave dynamics, various physical processes that affect their dynamics have been investigated using process-based modeling approaches. As shown by Hulscher (1996), small-amplitude sand wave dynamics can be investigated using linear stability analysis. It produces growth and migration rates as a function of the topographic wave vector (k_x, k_y), which is related to wavelength and crest orientation. If the growth rates are negative for all (k_x, k_y), i.e. the perturbations decay, the flat seabed is stable. If some mode grows, the seabed is unstable, and the fastest growing mode (FGM) is assumed to be the dominant bed form (Dodd et al., 2003). The FGM properties have successfully been used to predict sand wave occurrence (Hulscher and Van den Brink, 2001) and variations (Van Santen et al., 2011). By extending Hulscher's approach, sand wave migration has been explained by pressure- or wind-driven currents (Németh et al., 2002) and by tidal asymmetry (Besio et al., 2004). Other studies investigated the effects of grain-size variation (Roos et al., 2007; Van Oyen and Blondeaux, 2009), benthos (Borsje et al., 2009) and non-erodible bed layers (Blondeaux et al., 2016). Blondeaux and Vittori (2016) successfully compared modeled sand waves with observations (Menninga, 2012). They included the spring-neap cycle, a residual current and a single wind wave condition. Inspired by the storm-related observations mentioned above, Campmans et al. (2017) developed a linear stability model to systematically investigate the effect of wind-driven flow and wind waves on sand wave dynamics. Both waves and wind are potentially able to reduce the growth rate of sand waves. Wind-driven flow induces sand wave migration and wind waves enhance migration already occurring due to other processes. Importantly, the results by Campmans et al. (2017) were obtained by studying the various wave and wind conditions in isolation; their weighted effects in wave and wind climate averaged sense were not taken into account. Strictly speaking, linear stability

analysis is only valid for infinitesimally small amplitudes. However, applying it in practice with a finite amplitude gives a reliable approximation (e.g., up to 1 m, as illustrated in Fig.11 in Campmans et al., 2018). Linear stability models typically are computationally fast (seconds), which makes them suitable to explore the parameter space in detailed sensitivity studies.

Capturing finite amplitude sand wave dynamics including equilibrium shape and height requires a nonlinear modeling approach (Németh et al., 2007; Van den Berg et al., 2012; Van Gerwen et al., 2018; Campmans et al., 2018). However, these models are computationally heavy (hours/days, or even longer), which puts limits to their applicability.

As outlined above, both linear and nonlinear model approaches have their own benefits and weaknesses. Ideally they should be used in combination, such that computationally heavy nonlinear models are used with parameters obtained from the fast linear stability model.

The aim of this work is to determine the effects of a wave and wind climate on sand wave dynamics at a typical North Sea location. Restricting to small-amplitude dynamics, we specifically address the following three research questions:

- How does the North Sea wave and wind climate affect the sand wave growth and migration rates?

- Which storm conditions have the largest impact on sand wave dynamics, e.g. the more moderate, frequent conditions or the extreme, rare conditions?

- How do the properties of the fastest growing mode (growth rate, migration rate, wavelength) vary seasonally, i.e. distinguishing the rougher winter periods from milder summer periods?

To answer these questions, we process time series of observations into a wave and wind climate, which is then used as input for the linear stability model by Campmans et al. (2017). The model output results in a wave and wind climate-averaged growth and migration rate as function of k_x and k_y. This requires a statistical approach in which the joint probability of wave and wind parameters is taken into account in the climate-averaged model outcome. As location we choose the Euro Platform, which is an offshore structure to aid navigation and equipped with wave and wind measurement instruments. It is located in a sand wave field at approximately 50 km west of the port of Rotterdam (Fig.3.1). The innovation of this work is that we combine modeled wave and wind effects with the joint probability of wave and wind conditions obtained from observational data in order to generate site-specific results.

The paper is structured as follows. Section 3.2 explains how wave and wind data are used together with the linear stability model and provides values of the model parameters at the research location. In Section 3.3 the resulting effect of the wave and wind climate on sand wave dynamics is shown and the contributions of various wave and wind conditions are explained. Finally, Sections 3.4 and 3.5 contain the discussion and conclusion, respectively.

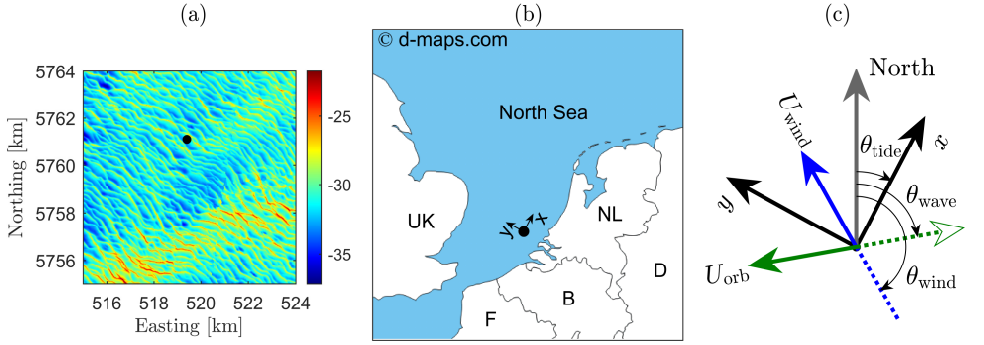

Figure 3.1: (a) Sand wave field in the vicinity of the Euro Platform (data from Royal Dutch Navy). (b) Map of the Southern North Sea with Euro Platform indicated by a black dot (source: d-maps.com). The (x, y)-axis indicates the local coordinate system used in the linear stability model, where the x-direction coincides with the principal tidal flow direction. (c) Definition sketch defining wave angle and wind angle clockwise w.r.t. north.

3.2 Methods

3.2.1 Site-specific conditions at the Euro Platform

The average wavelength and wave height of the sand waves as presented in Figure 3.1 are 230 m (ranging from approximately 110-450 m) and 2.7 m (ranging from approximately 0.1-7.6 m), respectively. Damen et al. (2018) performed an extensive data analysis study to systematically investigate correlations between sand wave characteristics and environmental properties across the entire Dutch continental shelf, including our case study area. This work identified areas that are bed load or suspended load dominated. Since our study location is in a bed load dominated region (see Figure 8A in Damen et al., 2018), we decided not to include suspended load sediment transport. These model parameters include site-specific values of, among others, a sediment grain size of 393 μm, 0.2 tidal ellipticity, a tidal flow oriented at 28° w.r.t. north, and a water depth of 31 m (Damen et al., 2018). In the same area Menninga (2012) analyzed sand wave dynamics, including migration. Our model findings will be compared with their observed sand wave migration.

3.2.2 Wave and wind data at the Euro Platform

At the Euro Platform hourly wave and wind measurement data are available from Rijkswaterstaat (n.d.) and KNMI (n.d.), respectively. The hourly measurements contain wave height H_{w}, wave period T_{w}, wave direction θ_{wave}, wind speed U_{wind} and wind direction θ_{wind} during the period 1996–2017, of which a three-month section is shown in Figure 3.2.

The wave and wind condition vector $\boldsymbol{\xi}$ is

$$\boldsymbol{\xi} = (U_{\text{wind}}, \theta_{\text{wind}}, U_{\text{orb}}, \theta_{\text{wave}}), \tag{3.1}$$

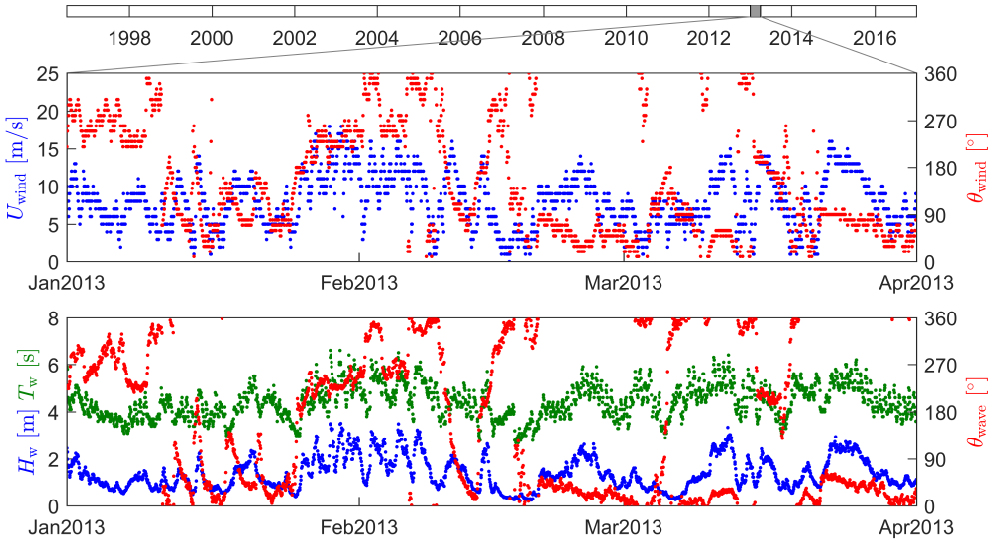

Figure 3.2: A graphical impression of the wave and wind data measured at the Euro Platform showing the entire measurement period (top), as well as zoomed graphs of wind speed U_{wind} and angle θ_{wind} (middle) and wave height H_{w}, period T_{w} and angle θ_{wave} (bottom) for the period January 1$^{\mathrm{st}}$ – April 1$^{\mathrm{st}}$, 2013.

which contains the wind speed U_{wind}, wind direction θ_{wind}, near-bed wave orbital velocity amplitude U_{orb} and wave direction θ_{wave}. The wave and wind angles θ_{wave} and θ_{wind} (i.e., the directions from which they approach) are measured clockwise with respect to north, see Figure 3.1c. The near-bed orbital velocity amplitudes are computed using linear wave theory (e.g., Mei, 1989) according to

$$U_{\mathrm{orb}} = \frac{\pi H_{\mathrm{w}}}{T_{\mathrm{w}} \sinh k_{\mathrm{w}} h}, \tag{3.2}$$

where H_{w} is the wave height, T_{w} the wave period, h the water depth and k_{w} the wave number determined by the dispersion relation

$$\left(\frac{2\pi}{T_{\mathrm{w}}}\right)^2 = g k_{\mathrm{w}} \tanh(k_{\mathrm{w}} h). \tag{3.3}$$

Here g is the gravitational acceleration constant. Importantly, Eq.(3.2) enables us to combine two parameters (wave period T_{w} and wave height H_{w}) into one single parameter U_{orb}, thus reducing the dimension of the parameter space from five to four. This speeds up the computations.

3.2.3 Joint wave and wind probability density function

Using the data, a joint probability density function of the occurrence of wave and wind parameter combinations $\boldsymbol{\xi}$ is determined. The data combinations, $\boldsymbol{\xi}$, are binned

Table 3.1: Bin bounds for each of the four wave and wind parameters, leading to a total of $12^4 = 20,736$ bins.

U_{wind} [m/s]	θ_{wind} [°]	U_{orb} [m/s]	θ_{wave} [°]
0.00	28	0.000	13
2.08	58	0.042	28
4.17	88	0.083	43
6.25	118	0.125	58
8.33	148	0.167	73
10.42	178	0.208	88
12.50	208	0.250	103
14.58	238	0.292	118
16.67	268	0.333	133
18.75	298	0.375	148
20.83	328	0.417	163
22.92	358	0.458	178
25.00	28	0.500	193

into $M = 12^4$ equally spaced bins. For all bins the probability of the wave and wind conditions is computed using the hourly measured wave and wind data, according to

$$P(\boldsymbol{\xi}_{\text{lower}}, \boldsymbol{\xi}_{\text{upper}}) = \frac{1}{N} \sum_{n=1}^{N} \eta(\boldsymbol{\xi}_n, \boldsymbol{\xi}_{\text{lower}}, \boldsymbol{\xi}_{\text{upper}}). \tag{3.4}$$

Here $P(\boldsymbol{\xi}_{\text{lower}}, \boldsymbol{\xi}_{\text{upper}})$ is the probability of wave conditions $\boldsymbol{\xi}$ to be inside the bin bounded by lower and upper interval limits $\boldsymbol{\xi}_{\text{lower}}$ and $\boldsymbol{\xi}_{\text{upper}}$, respectively. Furthermore, N is the total number of hourly wave and wind data points, here $N = 169,657$, $\boldsymbol{\xi}_n$ represents the measured wave and wind conditions for the n^{th} data point, see Eq.(3.1). Finally, $\eta(\boldsymbol{\xi}_n, \boldsymbol{\xi}_{\text{lower}}, \boldsymbol{\xi}_{\text{upper}})$ is a function that returns one if the measurement $\boldsymbol{\xi}_n$ is inside the bin and zero otherwise. The bin bounds applied in this study are shown in Table 3.1.

The bin bounds for the wave and wind angles are chosen such that the bins are defined symmetrically around the tidal current direction ($\theta_{\text{tide}} = 28°$ w.r.t. north, see Figure 3.1c.

3.2.4 Outline of linear stability model

The sand wave model is based on the morphodynamic loop and consists of three parts: (1) The hydrodynamics are described by the 3D shallow water equations which describe tidal and wind-driven flow. (2) Sediment transport is modeled by a bed load formula. Here wave stirring is taken into account. (3) The seabed evolution satisfies the Exner equation, which describes sediment conservation.

Consider a sinusoidal seabed perturbation (representing a sand wave) characterized by topographic wave vector (k_x, k_y), with magnitude $k = (k_x^2 + k_y^2)^{1/2}$. The

Table 3.2: Overview of model parameters.

Model parameter	Symbol	Reference value†	Unit
Water depth	H	31	m
Tidal current velocity (M2)	U	0.5	m s^{-1}
Tidal frequency (M2)	σ	$1.41 \cdot 10^{-4}$	rad s^{-1}
Tidal angle (M2)	θ_{tide}	28	°
Wave friction factor	f_{w}	0.1	-
Gravitational acceleration	g	9.81	m s^{-2}
Vertical eddy viscosity	A_{v}	0.04	m^2 s^{-1}
Slip parameter	S	0.01	m s^{-1}
Slope correction factor	λ	1.5	-
Tidal ellipticity (M2)	ϵ_{M2}	0.2	-
Sediment grain size	d	393	μm
Bed load exponent	β	1.5	-
Bed load coefficient	α	$1.51 \cdot 10^{-5}$	$m^{\beta+2}s^{2\beta-1}kg^{-\beta}$

model solution describes exponential growth (or decay) and migration of this individual mode:

$$h(x, y, t) = h_{\text{init}} \exp(\omega t) \cos(k_x x + k_y y - k c_{\text{mig}} t). \tag{3.5}$$

Here, h_{init} is the initial amplitude of the perturbation, ω the growth rate and c_{mig} the migration rate (in the direction orthogonal to the sand wave crests). These growth and migration rates depend on (k_x, k_y). As pointed out in the introduction, if the growth rate is negative for all (k_x, k_y) the flat seabed is stable. Otherwise, it is unstable and the perturbation with the maximum growth rate is termed the 'fastest growing mode' (FGM).

Here we use the linear stability model to analyze the stability of a flat seabed under different wave and wind conditions. This can be written as

$$\omega = \omega(k_x, k_y, U_{\text{wind}}, \theta_{\text{wind}}, U_{\text{orb}}, \theta_{\text{wave}}), \tag{3.6}$$

$$c_{\text{mig}} = c_{\text{mig}}(k_x, k_y, U_{\text{wind}}, \theta_{\text{wind}}, U_{\text{orb}}, \theta_{\text{wave}}). \tag{3.7}$$

The model parameters, other than wave and wind conditions, are presented in Table 3.2. For a detailed model description we refer to Campmans et al. (2017).

3.2.5 Combining model results with wave and wind probability

In the linear regime, the sequence in which the various wave and wind conditions occur, is irrelevant. This property enables us to compute growth and migration rates that are averaged over the combined wave and wind climate. These are termed the climate-averaged growth and migration rates.

For each bin of wave and wind conditions for which the weighting factor is nonzero, the linear stability model is applied with the wave and wind conditions coinciding with the bin centers $\bar{\boldsymbol{\xi}} = \frac{1}{2}(\boldsymbol{\xi}_{\text{lower}} + \boldsymbol{\xi}_{\text{upper}})$.

The climate-averaged growth and migration rates, $\langle\omega\rangle$ and $\langle c_{\text{mig}}\rangle$ respectively, are computed by multiplying the linear stability model output for the bin-centered wave and wind conditions with the corresponding probability P_m of those conditions, and summing over all $M = 12^4$ bins:

$$\langle\omega\rangle = \sum_{m=1}^{M} P_m \omega_m, \tag{3.8}$$

$$\langle c_{\text{mig}}\rangle = \sum_{m=1}^{M} P_m c_{\text{mig},m}. \tag{3.9}$$

To analyze the effect of wave and wind conditions, we also calculate the dynamics of the system with tide only ($\omega_{\text{tide}}, c_{\text{mig,tide}}$) i.e. no waves and wind: $U_{\text{wind}} = 0$ and $U_{\text{orb}} = 0$. For each bin, we then define the probability-weighted relative growth and migration rate according to

$$\Delta\omega_m = P_m \left(\omega_m - \omega_{\text{tide}}\right), \tag{3.10}$$

$$\Delta c_{\text{mig},m} = P_m \left(c_{\text{mig},m} - c_{\text{mig,tide}}\right). \tag{3.11}$$

The probability-weighted storm effect gives insight which storm conditions have the biggest influence on the total climate-averaged sand wave dynamics.

3.3 Results

3.3.1 Probability density function

The probability density function resulting from the binning procedure is in fact a four dimensional matrix, which is visualized in Figure 3.3. The distinct patterns in the colored part of the figure (top) indicate that wave and wind conditions are correlated, most clearly regarding direction. The peaks in the bar plots (bottom row) show the dominant wind speed (around 5-10 m/s), wind direction (roughly SW), orbital velocity (0-0.05 m/s) and wave direction (also SW). Also many of the bins are empty or close to empty showing that those conditions never or hardly occur. The probability density function shows that extreme wave and wind conditions rarely occur, waves hardly reach significant orbital velocities for most of the time. Larger wave orbital velocities occur mainly in combination with larger wind speeds, and the wave and wind direction are strongly correlated suggesting that most of the measured waves are locally induced by the wind conditions.

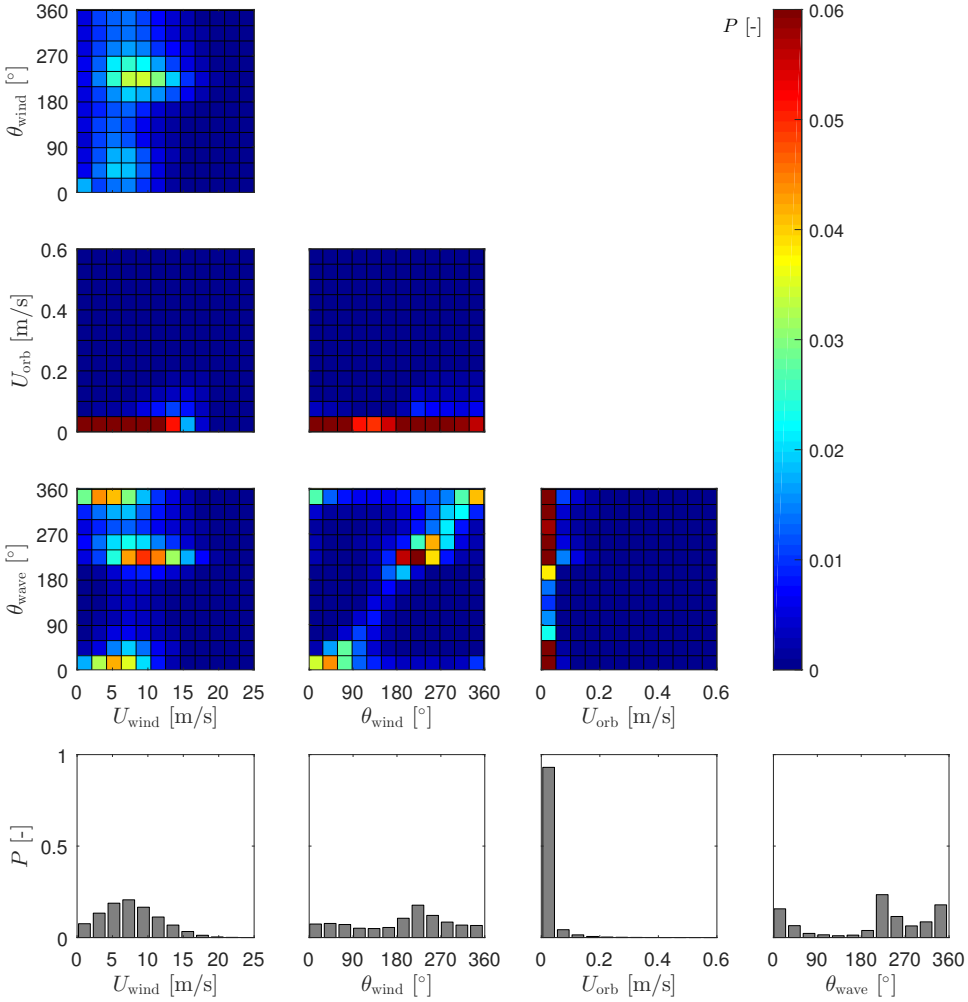

Figure 3.3: Visualization of the four-dimensional probability density function, showing the frequency of occurrence (P) as a function of the four wave and wind parameters. Each two-dimensional color plot shows the joint probability for two of the parameters, i.e. summing over the two other parameters. The four bottom plots show the distribution over each of the four parameters, i.e. summing over the three other parameters. This means that the frequencies in each individual plot add to one.

3.3.2 Wave and wind climate-averaged dynamics

Figure 3.4 shows for both fair-weather and wave and wind climate-averaged conditions the growth and migration rate as function of (k_x, k_y). For fair-weather conditions the FGM is a mode with crests perpendicular to the tidal flow direction and with a wavelength of $L_{\mathrm{FGM}} = 356$ m, the growth rate is $\omega_{\mathrm{FGM,tide}} = 0.390\ \mathrm{yr}^{-1}$ and due to the symmetrical tidal forcing the migration rate is zero.

In comparison, for the wave and wind-climate averaged results, the FGM has hardly shifted: it has a wavelength of $\langle L_{\mathrm{FGM}} \rangle = 361$ m, a growth rate of $\langle \omega_{\mathrm{FGM}} \rangle = 0.387\ \mathrm{yr}^{-1}$ and a migration rate of $\langle c_{\mathrm{mig,FGM}} \rangle = 6.6\ \mathrm{m\,yr}^{-1}$. A positive migration rate is in the direction of the positive x-axis, as shown in Figure 3.1.

3.3.3 Storm effects on growth and migration rate

The four-dimensional relative growth and migration rates, corresponding to the climate-averaged fastest growing mode (denoted with a plus-sign in Figs.3.4c-f) are shown in Figures 3.5 and 3.6, respectively.

Figure 3.5 shows both negative and positive growth rate contributions (relative to fair-weather) indicating that storm conditions can both enhance and reduce sand wave growth. Adding all growth rate contributions results in a rather small overall negative contribution to the growth rate of $\Delta\omega = \langle \omega \rangle - \omega_{\mathrm{tide}} = -2.9 \cdot 10^{-3}\ \mathrm{yr}^{-1}$. These negative values also appear for other topographic wave numbers (k_x, k_y), as seen from the growth rate plots in Fig.3.4e. Regarding migration rates, shown in Figure 3.6, we observe predominantly positive contributions from the southwest direction.

3.3.4 Mild versus extreme conditions

To address the question which storm conditions have the largest effects mild, medium and extreme conditions are defined. This classification is based on wave orbital velocity and wind speed values that coincide with bin bounds, and irrespective to wave or wind angle. First, 'mild' conditions are considered to have wave orbital velocities below 0.05 m/s and wind speeds below 8.33 m/s. Then, 'medium' conditions have orbital velocities below 0.1 m/s and wind speeds below 16.67 m/s. The remaining conditions are termed 'extreme'. Mild, medium and extreme conditions are indicated by the colors in Figure 3.7. Figure 3.7(a) shows the percentages of the probability of mild, medium and extreme conditions to occur and 3.7(b) shows the relative to fair-weather migration rate contribution. Note that for computing the percentages, the absolute value of the relative to fair-weather growth and migration rate of each bin has been taken.

The plots in Figure 3.7 clearly show a shift in percentages between the probability contribution and the migration rate contribution. Whereas mild conditions occur for 59.7% of the time, they result in only a contribution of 17% to the total migration rate. Intermediate conditions occur for 36.8% of the time, whereas they cause 67% of the total migration rate. Extreme conditions occur for 3.5% of the time, causing 15.7% of the total migration rate. These percentages of course depend on the definition of mild, medium and extreme conditions, but the general picture remains the following.

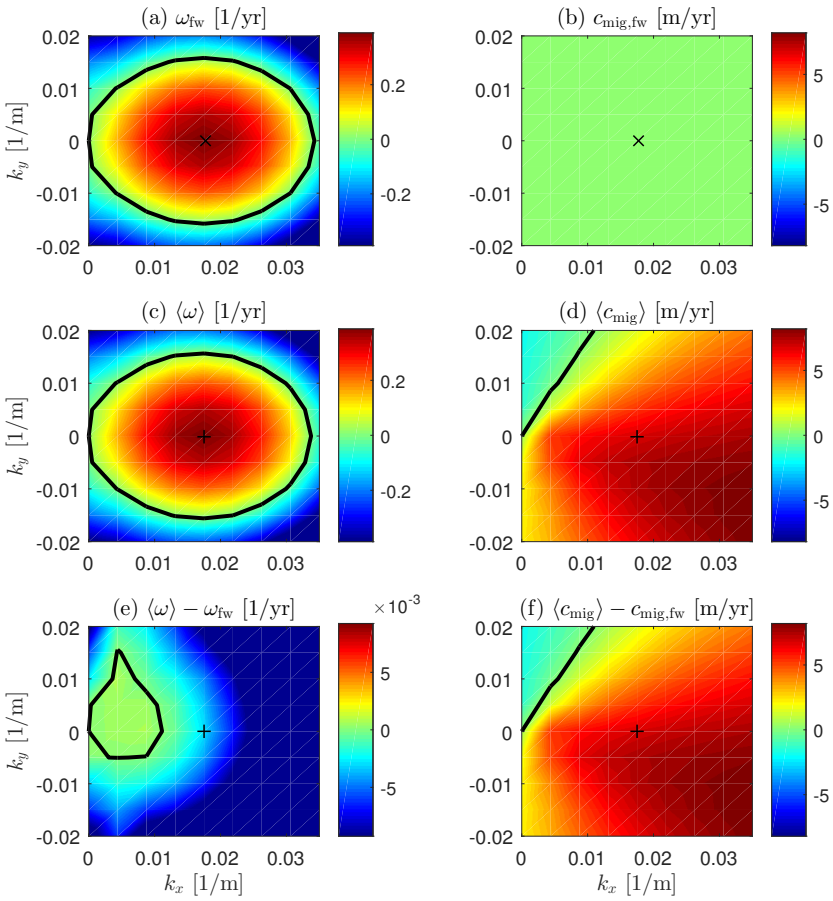

Figure 3.4: Growth rates (ω, left) and migration rates (c_{mig}, right), as a function of the topographic wave vector (k_x, k_y), for three cases: fair weather (top), climate-averaged (middle), difference (bottom). The $\times$ and $+$ indicate the fair-weather and climate averaged fastest growing modes, respectively.

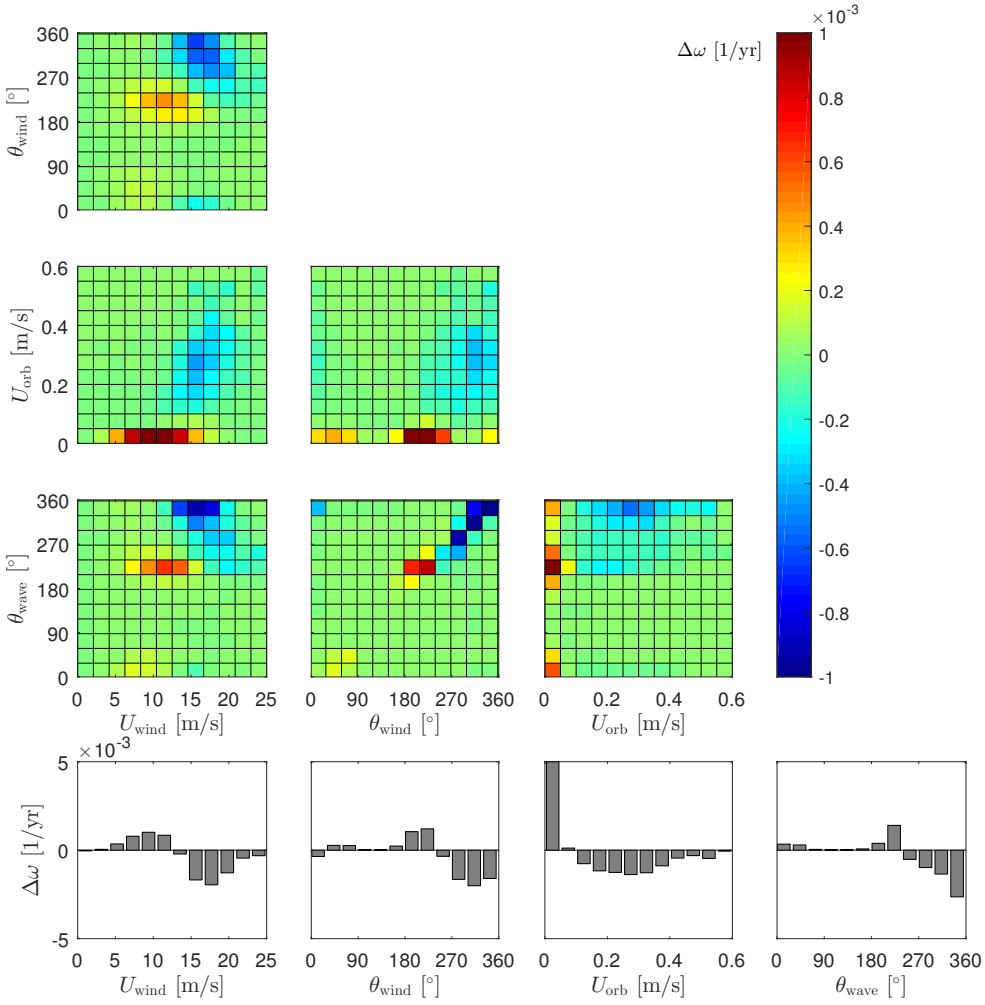

Figure 3.5: Visualization of the four-dimensional storm contributions of the weighted model runs to the *growth rate* ω [yr^{-1}] corresponding to the wave and wind conditions in the bins. Note that the plotted two-dimensional bins are in fact a summation over the other two bins. The lower four plots show the contributions of each of the four wave and wind conditions. These growth rate contributions correspond to the climate-averaged FGM.

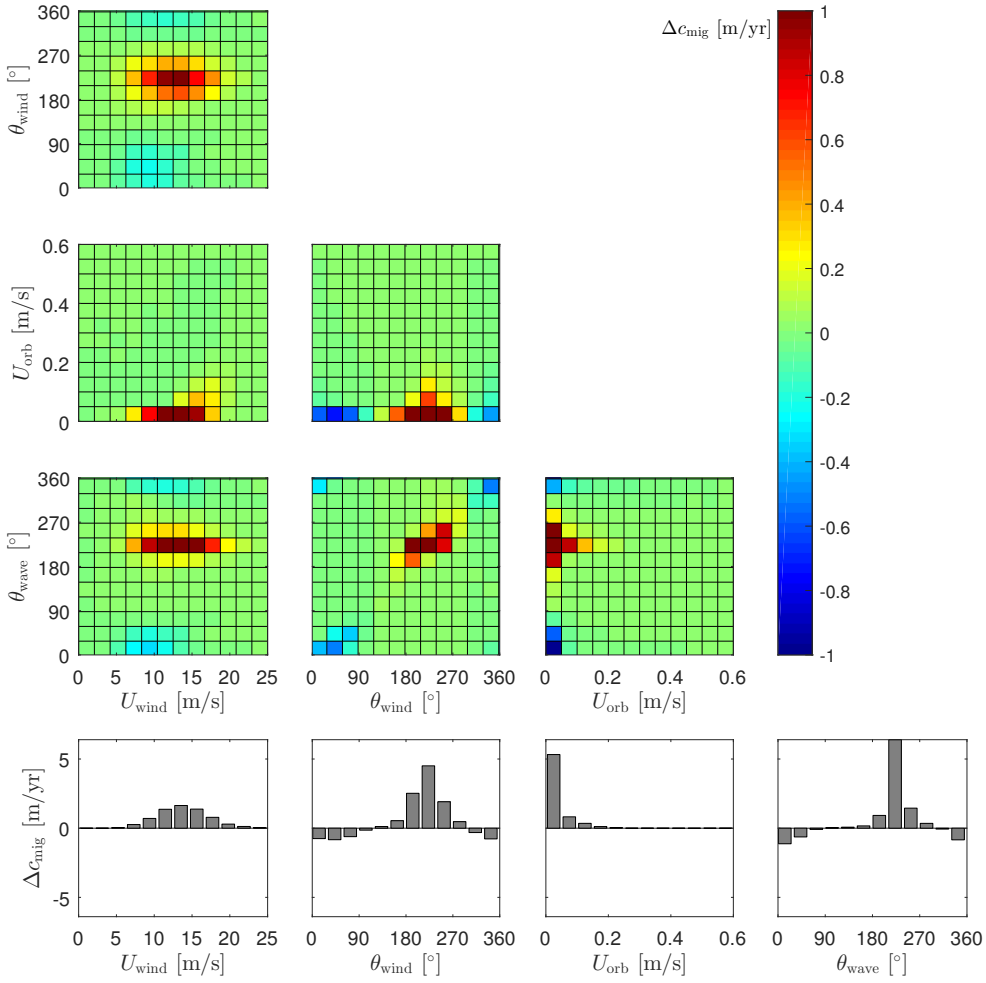

Figure 3.6: Visualization of the four-dimensional storm contributions of the weighted model runs to the *migration rate* c_{mig} [$\text{m}\,\text{yr}^{-1}$] corresponding to the wave and wind conditions in the bins. Note that the plotted two-dimensional bins are in fact a summation over the other two bins. The lower four plots show the contributions of each of the four wave and wind conditions. These migration rate contributions correspond to the climate-averaged FGM.

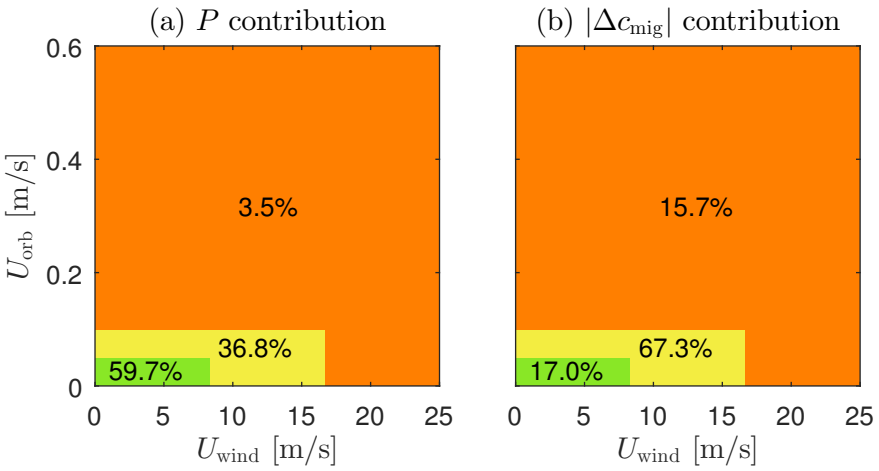

Figure 3.7: Relative contributions of mild (green), medium (yellow) and extreme (orange) wave and wind conditions. The two subfigures show: (a) the probability P of the condition to occur and (b) the relative migration rate effect $|\Delta c_{\mathrm{mig}}|$ (absolute values).

Relative to their occurrence, the contribution of mild conditions to the migration rate is only small. For medium conditions the contribution to the migration rate is large compared to their occurrence. This shift is even stronger for extreme conditions. Overall, the major contribution to sand wave migration is caused by conditions that combine a sufficiently large effect with a relatively large probability of occurrence.

The contributions of mild, medium and extreme conditions to $\Delta\omega$ show a similar shift (not shown here). Because the total effect on the climate-averaged growth rate is small (Section 3.3.3), we do not further analyze this.

3.3.5 Seasonal variations: winter vs summer

By repeating our analysis for yearly seasonal sections of the wave and wind data we obtain seasonal wave and wind averaged FGM properties. Here we defined the winter season for a given year as from 1 October of the past year until 1 March. The summer season is from 1 March until the 1 October. These FGM properties as function of year are shown in Figure 3.8.

Here we observe that especially the migration rate shows large seasonal variations, which support variation of observed migration due to storm effects (Fenster et al., 1990) as well as seasonal variations (Harris, 1989). The mean migration rate in summer is 3.4 m/yr (with standard deviation $\sigma = 1.7$ m/yr) and 8.1 m/yr in winter ($\sigma = 2.2$ m/yr).

Also the growth rate and the wavelength of the fastest growing mode show a systematic seasonal variation, be it only small. The mean growth rate in summer is 0.392 yr^{-1} ($\sigma = 2.3 \cdot 10^{-3}$ yr^{-1}) and 0.385 yr^{-1} in winter ($\sigma = 3.2 \cdot 10^{-3}$ yr^{-1}). The mean wavelength in summer is 355m ($\sigma = 2.1$ m) and 363 m in winter ($\sigma = 2.9$ m).

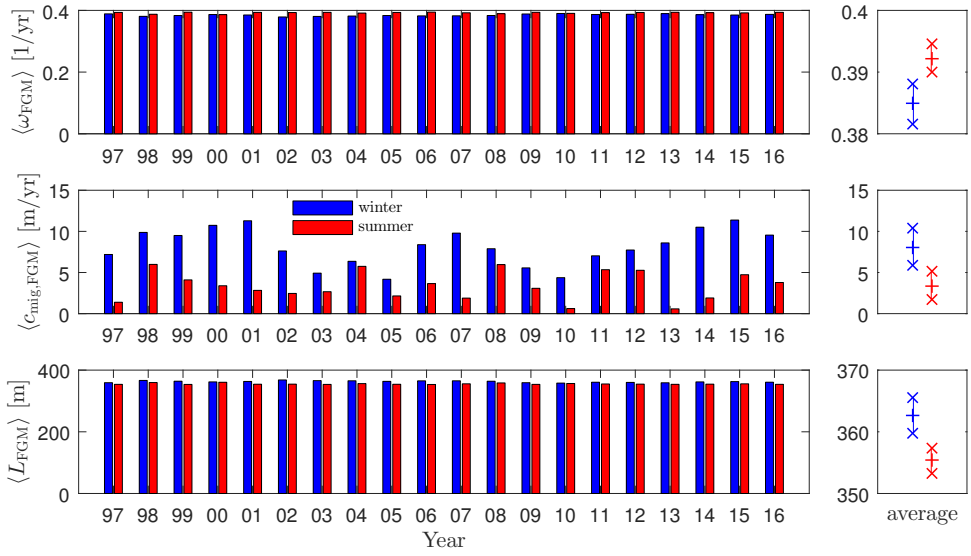

Figure 3.8: The wave and wind climate-averaged properties of the fastest growing mode (growth rate ω, migration rate c_{mig} and wavelength L) for winter (blue) and summer (red) season between 1997 and 2016. The years 1996 and 2017 have been excluded in this analysis since no full year data is available. The panels on the right show the mean values indicated with a + plus and minus the standard deviation indicated with a $\times$. Please note the different scales in the vertical axes.

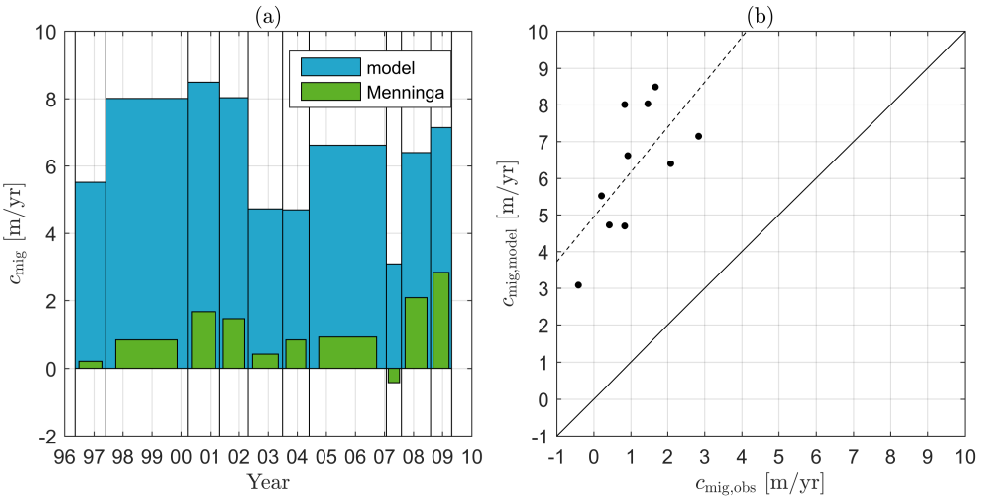

Figure 3.9: Comparing the modeled wave and wind climate-averaged migration rate c_{mig} of the fastest growing mode with the observations (see Fig. 3.9 from Menninga, 2012). (a) Observed (green) and modeled (light blue) migration rates placed on the time intervals in-between surveys (vertical black lines). (b) Scatter plot of modeled versus observed migration rates per time interval, showing the fitted linear function (dashed) in Eq.(3.12).

3.3.6 Comparison with field observations

Menninga (2012) analyzed sand wave characteristics at various locations in the North Sea. Close to the Euro Platform he analyzed a sand wave transect with 15 surveys between 1992 and 2010. From 1996 onwards we have both wave and wind data from the Euro Platform (Fig.3.2). Here, we compare the migration rates obtained from our model approach using the wave and wind data between the sand wave survey moments with observed migration rates from the analysis of Menninga (2012). As shown in Figure 3.9, we find a correlation between modeled and observed migration rates, which can be captured in a linear function fitted using the least squares reads:

$$c_{\text{mig,obs}} = -4.04 + 0.817 c_{\text{mig,model}}. \tag{3.12}$$

with correlation coefficients $R = 0.67$ and $p = 0.035$. This shows a reasonable agreement indicating that the method might work to estimate sand wave migration based on wave and wind observations. Nevertheless these statistics are based on only 10 data points which is certainly not sufficient to claim that the method is robust. The coefficients in Eq.(3.12) are not by any means universal and should be determined for a specific location. The modeled migration overestimates the observed values and the constant -4.04 in Eq.(3.12) suggests a tidal asymmetry or residual current, which we did not include in our model.

3.4 Discussion

Our model results have shown that for a simple setup, we have obtained realistic values of sand wave migration rate and wavelength. The following simplifications have been made: symmetrical tidal current, no Coriolis effect and bed load transport only. Observational data show (Le Bot et al., 2000, Figure 4) that veering of the flow due to the Coriolis effect is not as large as predicted in our infinitely large model domain. This justifies neglecting the Coriolis effect in our simulations. The effect of suspended load sediment transport is left out in our analysis as environmental conditions at the study site show that bed load is the dominant transport mode (see Figure 8A in Damen et al., 2018).

The turbulence model used in the model is based on a constant eddy viscosity which reasonably resolves the flow outside the boundary layer, supplemented with a partial slip condition at the seabed to simulate smaller turbulent mixing near the bed to find reasonable shear stresses at the seabed. The results of the linear stability sand wave model turn out to be sensitive to this partial slip parameter. Other studies investigated the use of more sophisticated turbulence models in sand wave modeling, and show that quantitatively more refined turbulence modeling improves sand wave generation. However, more refined turbulence models come at the cost of more computational effort. Qualitatively a constant eddy viscosity model is able to capture the generating mechanism of sand waves, if the partial slip parameter is properly chosen. We tuned the partial slip parameter such that in fair-weather conditions the sand wave wavelength corresponds to those observed in the field. The constants determined in Eq.(3.12) are partially explained by the simplifications in the setup. However, the model is still able to capture the most important dynamics.

As it turns out that variations in wave and wind conditions also lead to variations in sand wave migration our model could prove useful as a predictive tool solely based on measured wave and wind conditions, potentially decreasing the bathymetric surveying frequency that is required to guarantee shipping safety.

In other locations variations in sand wave migration have been observed, and these are associated with variations in wind conditions (Le Bot et al., 2000; Krewinkel et al., 2017). In the Adolphus Channel, northeast of Australia, Harris (1989) shows seasonal reversal of sand wave migration during the monsoon season.

Since we make use of a linear stability model, for which we look at the formation stage of small sand waves, the sequence in which wave and wind conditions occur is irrelevant. For large sand wave amplitudes a nonlinear analysis is required, in which the sequence in which wave and wind conditions occur is relevant. However, an equivalent nonlinear analysis with equally many wave and wind conditions is not yet feasible with available sand wave models.

Our model findings imply that climate change will affect sand wave dynamics. If waves and wind conditions become more extreme, this will result in larger sand wave migration rates.

Our work shows that wind and waves can cause a seasonal varying effect on sand wave characteristics. Particularly the migration rate is subject to seasonal variations. The change in preferred wavelength is only small, and on the timescale of seasonal

variations sand waves are unlikely to show variations in wavelength. Furthermore it should be noted that various other phenomenon may affect sand waves seasonally, such as biology (Borsje et al., 2009; Damveld et al., 2017) or thermally induced variations in tidal characteristics (Gräwe et al., 2014).

Blondeaux and Vittori (2016) includes a wide variety of processes in their model. Among them wind waves, the spring-neap cycle and a residual tidal component. In our work we focus in detail on an actual wave and wind climate on sand wave dynamics, while using a more simplified version of other processes. Our work agrees with their model findings and additionally shows that seasonal variations may occur as well as which of the wave and wind conditions contribute the most.

This research has been carried out as part of a bigger project called SMARTSEA. The goal of the project is to improve the efficiency and safety of navigation. For safe navigation in shallow seas such as the North Sea with a dynamic seabed, mainly caused by sand wave dynamics, accurate nautical charts are required. At present sand wave dynamics are poorly predictable and frequent surveying is required. This research shows from a process-based perspective that storms are one of the mechanisms that causes the irregularities in sand wave dynamics. A better understanding of the temporally varying migration and growth behavior of sand wave dynamics will eventually reduce the surveying frequencies and lead to more efficient maintenance strategies for navigation channels.

Ernstsen et al. (2011) observed spatiotemporal variations in sand wave height in the Grådyb tidal inlet channel (Denmark) and linked this to a nearby scour hole formed by a sunk dredger. In their work they observe temporal variations in sand wave height and report a large influence of the scour hole on the sand wave height. Before the formation of the scour hole temporal variations in height are also present, albeit that these variations are smaller than the variations after the formation and subsequent filling of the scour hole. In our work we were restricted to small-amplitude dynamics. Wind and waves may well be able to cause temporally variable sand wave height variations in a similar fashion as the observed migration rate. This would require future research.

3.5 Conclusion

By combining wind and wave data with an idealized linear stability model we were able to investigate the effect of an actual storm climate on sand wave dynamics near the Euro Platform in the North Sea. We find that storms affect particularly migration, and to a smaller extent the growth rate. The fastest growing mode properties of sand waves in a storm climate of the past 20 years have a slightly lower growth rate and a slightly longer wavelength, compared to the fair-weather model results. The most notable effect is a 6.6 $\mathrm{m\,yr^{-1}}$ migration rate towards the northeast. The very small ($\sim 1\%$) decrease in growth rate indicates that the growth and wavelength of sand waves is hardly affected by storm effects at our study site.

Because the model is quick, it enables to conduct a very large number of simulations (order 10^4). We have identified the type of wind and wave conditions with

the largest contributions, taking into account both the probability of occurrence and their effect. The analysis showed that even though some conditions rarely occur they still had a prominent contribution due to their large effect during such conditions. We find that medium conditions are responsible for two thirds of the migration rate ($\sim$67%), while these conditions occur roughly only one third of the time ($\sim$37%).

Partitioning the data sets of wind and wave conditions into yearly seasonal time series allowed us to investigate the effect of seasonal effects. We observed a clear trend between summer and winter periods. Typically sand wave migration rates are larger during winter times compared to the more calm summer periods. Similarly growth rates are lower and the preferred wavelength is larger during winter periods compared to the summer periods, although these effects are only small compared to migration rate effects. Migration rate variations have been observed by many observational studies, for which many of the authors referred to the potential effects of storms. From a process-based modeling perspective, we have linked migration rates of sand waves in the North Sea (and their seasonal fluctuations) to observed variations in wave and wind conditions. Finally, comparison of our model results with observed sand wave migration supports the suggested link between the occurrence of wave and wind conditions and temporal variability in sand wave migration.

3.6 Acknowledgements

This work is part of the research programme SMARTSEA with project number 13275, which is (partly) financed by the Netherlands Organisation for Scientific Research (NWO). The authors thank John Damen for providing site specific sand wave characteristics.

Chapter 4

Modeling the influence of storms on sand wave evolution: a nonlinear idealized modeling approach*

Abstract

We present a new 2DV nonlinear process-based morphodynamic model to investigate the effects of storms, specifically wind-driven flow and wind waves, on finite amplitude tidal sand wave evolution. Simulations are performed on periodic domains of two lengths: (i) on a 350 m domain, comparable to the wavelength of observed sand waves, we study the evolution towards equilibrium shapes and (ii), on a 4 km domain we study the evolution from a randomly perturbed seabed. Our model results demonstrate that both wind-driven flow and wind waves reduce sand wave height and tend to increase wavelength. Wind-driven flow breaks the tidal symmetry, resulting in horizontal sand wave asymmetry and migration. Waves alone do not induce migration, but can enhance migration induced by e.g. tidal asymmetry and wind-driven flow. On the 350 m domain, we further find that migration rates decrease with increasing sand wave height. However, in an irregular sand wave field, large sand waves tend to overtake the smaller ones, suggesting a complicated interaction among neighboring bed forms. The above results concern steady state storm conditions. However, since storms occur on an intermittent basis, we also simulated a synthetic storm climate consisting of alternating short periods of storm conditions and long periods of fair-weather conditions. Simulations reveal a dynamic equilibrium with sand wave heights

*This chapter is published as Campmans, G.H.P., P.C. Roos, H.J. de Vriend, and S.J.M.H. Hulscher (2018). Modeling the influence of storms on sand wave evolution: a nonlinear idealized modeling approach, *Journal of Geophysical Research - Earth Surface*

significantly below those obtained for tide-only conditions, also for relatively short storm duration. Our work identifies mechanisms that explain why sand wave heights are generally overpredicted by numerical models that do not include storm processes.

4.1 Introduction

In many tidally dominated shallow seas tidal sand waves are observed, where typical water depths are 15-50 m (Hulscher and Van den Brink, 2001). Sand waves are large-scale dynamic bed forms that form a rhythmic seabed pattern (e.g. Terwindt, 1971; McCave, 1971). They have heights of several meters, wavelengths of 100-1000 m, can migrate up to several meters per year (Van Dijk and Kleinhans, 2005; Damen et al., 2018), and are typically formed at the time scales of several years.

The presence of sand waves dynamically affects the seabed topography, thus posing danger to navigation (Dorst et al., 2011), burying and exposing objects at the seabed such as sea mines and ship wrecks, creating free spans of cables and pipelines and affecting stability of offshore structures such as pylons for wind turbines and platforms. For all of these applications an accurate understanding of seabed dynamics and thus sand wave dynamics is desirable.

Even though tidal sand waves are generally believed to be formed and shaped by tidal currents, observational studies have shown that storm processes decrease their height (Terwindt, 1971; Houthuys et al., 1994; Van Dijk and Kleinhans, 2005) and significantly affects migration speed and direction (Fenster et al., 1990; Harris, 1989; Le Bot et al., 2000). Below we describe the literature on sand wave modeling, particularly focusing on the influence of storms.

Process-based models have been developed to understand the processes behind sand wave dynamics (see e.g. the review by Besio et al., 2008). Using a linear stability analysis, tidal sand waves have been explained as an instability of a sandy seabed subject to tidal flow (Hulscher, 1996). Tidally averaged recirculation cells tend to move sediment towards the crest, whereas gravity favors downslope transport towards the troughs. The perturbation with the largest growth rate is termed the fastest growing mode (FGM) and is considered to be the preferred bed form (Dodd et al., 2003).

Later, other researchers extended this linear stability approach to investigate the effect of various physical mechanisms on sand wave dynamics. For example, sand wave migration can be caused by pressure-gradient or wind-driven flow (Németh et al., 2002) or by tidal asymmetry (Besio et al., 2004). Others investigated the effect of a refined turbulence model (Blondeaux and Vittori, 2005a,b; Borsje et al., 2014) and grain-size variation (Roos et al., 2007; Van Oyen and Blondeaux, 2009). Campmans et al. (2017) investigated the effects of storms, wind waves and wind-driven flow, on sand wave formation using linear stability analysis of an idealized sand wave model. They concluded that storm effects indeed affect sand waves in the small-amplitude regime. Wind waves and wind-driven flow decrease the growth rate and increase the preferred wavelength of sand waves. Wind waves may enhance migration due to other processes, such as wind-driven flow, residual tidal current or tidal asymmetry.

Importantly, these studies are limited to small-amplitude seabed topographies only.

Nonlinear models were developed in order to explain finite-amplitude sand wave behavior. Németh et al. (2007) investigated sand wave height, shape and migration. Van den Berg et al. (2012) developed a sand wave solution method based on a spectral time-integration method for the flow, in order to investigate sand wave variation on large model domains. Later, a case study compared an initial version of this model with field data (Sterlini et al., 2009). All of these studies were able to describe equilibrium sand wave profiles on a domain with a length in the order of hundreds of meters. Shortcomings of these type of models are generally that the sand wave height is significantly overpredicted with sand wave heights in the order of 10 m instead of several meters and that the wavelength keeps increasing for larger model domains.

From the above literature review, we conclude that (*i*) the influence of storms on sand wave dynamics is significant, but has been modeled in the linear regime only, and that (*ii*) nonlinear models suffer from various shortcomings, such as overpredicting sand wave height. Therefore, the goal of this study is to assess the influence of storm processes on sand wave dynamics in the finite-amplitude regime. Specifically, we address the following research questions. Do storm effects lead to a decrease in sand wave height, and how do they affect sand wave shape and migration speeds?

To that end, we numerically solve the shallow water equations on a 2DV periodic domain, where tidal and wind-driven flow – enhanced by wave stirring – trigger sediment transport. With this model we systematically investigate the effect of wind-driven flow and wind waves on the evolution and final sand wave characteristics. We use simulations on both short and long domains with spatially periodic boundary conditions, because a short domain artificially fixes the wavelength as mentioned by Van den Berg et al. (2012). This would exclude the investigation of nonlinear wavelength effects.

The paper is structured as follows. Section 4.2 gives the model formulation and section 4.3 describes the solution procedure. In section 4.4, finite-amplitude model results are shown. Finally, sections 4.5 and 4.6 contain the discussion and conclusions, respectively.

4.2 Model formulation

4.2.1 Geometry

The model domain is schematically shown in Figure 4.1. It is a two dimensional (x, z) domain, in which flow is allowed in the third dimension. However, no variations in the y-directions are allowed $\partial/\partial y(\cdot) = 0$. Including flow in the second horizontal dimension allows for arbitrary wind and wave angles. The domain is spatially periodic in the x-direction, with domain length L, the mean water depth is H, with an undulating seabed topography h and surface elevation ζ which are both functions of x and t. Horizontally integrated, the seabed topography and surface elevation are zero, i.e. $\int_0^L h\mathrm{d}x = 0$ and $\int_0^L \zeta\mathrm{d}x = 0$. The tidal flow is directed parallel to the x-axis, whereas wind waves and wind may be directed under an angle with respect to the x-axis (Fig-

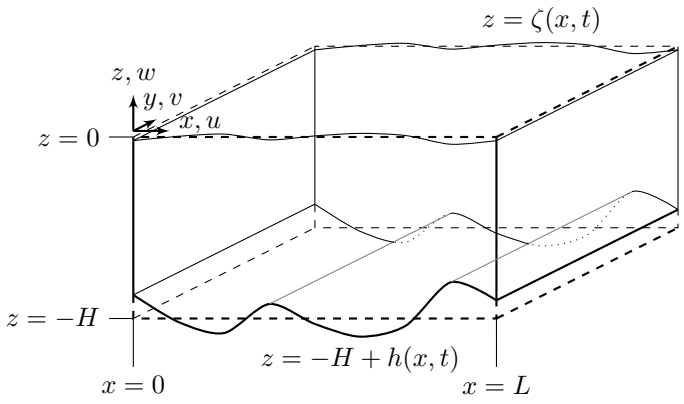

Figure 4.1: The model domain, a 2DV model that allows for velocity components but no variations in the y-directions: $\partial/\partial y(\cdot) = 0$. In the x-direction the domain is spatially periodic, with a domain length L.

ure 4.2). Spatial periodicity implies that all quantities (and their derivatives) are the same at $x = 0$ and $x = L$.

4.2.2 Hydrodynamics

The pressure is assumed to be in hydrostatic balance, so that the continuity and momentum equations in the original (x, z)–domain are given by

$$\boldsymbol{\nabla} \cdot \mathbf{u} = 0, \tag{4.1}$$

$$\frac{\partial \mathbf{u}_\mathrm{h}}{\partial t} + \mathbf{u} \cdot \boldsymbol{\nabla} \mathbf{u}_\mathrm{h} + g \boldsymbol{\nabla}_\mathrm{h} \zeta + \mathbf{F} - \frac{\partial}{\partial z} \left(A_\mathrm{v} \frac{\partial \mathbf{u}_\mathrm{h}}{\partial z} \right) = 0, \tag{4.2}$$

Here $\mathbf{u} = (u, v, w)^T$ is the velocity vector in the Cartesian coordinates $\mathbf{x} = (x, y, z)^T$, subscript $_\mathrm{h}$ denotes the horizontal (x- and y-) components of the vector, g is the gravitational acceleration constant, ζ the free surface elevation response to seabed undulations and $\mathbf{F} = (F_x, 0)^T$ is a spatially uniform forcing term representing free surface elevation gradient of the tidal wave. Turbulence is represented using the combination of a constant vertical eddy viscosity A_v (Bowden et al., 1959) and a partial slip condition at the bed (e.g. Hulscher, 1996; Van den Berg et al., 2012; Campmans et al., 2017). More refined turbulence models such as a Dean profile (Besio et al., 2006) or a k-ε (Borsje et al., 2013) model lead to quantitatively different but not qualitatively different results in the linear regime. The Coriolis effect is neglected, as it is only of minor importance for sand wave dynamics (Hulscher, 1996).

The boundary conditions at the free surface (rigid lid) and the sea bed (partial

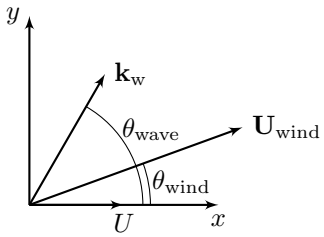

Figure 4.2: Definition sketch (top view) of the tidal current U, the wind velocity vector $\mathbf{U}_\mathrm{wind}$ and wave vector $\mathbf{k}_\mathrm{w}$ (in the direction in which the waves propagate). Although the depth-averaged tidal flow can be in arbitrary direction, in our model simulations it is always chosen aligned with the x-axis.

slip) are given by

$$\begin{aligned} w &= 0, & A_\mathrm{v}\frac{\partial \mathbf{u}_\mathrm{h}}{\partial z} &= \frac{\boldsymbol{\tau}_\mathrm{wind}}{\rho}, & \text{at} \quad z &= 0, \\ w &= u\frac{\partial h}{\partial x}, & \frac{\boldsymbol{\tau}}{\rho} \equiv A_\mathrm{v}\frac{\partial \mathbf{u}}{\partial z} &= S\mathbf{u}_\mathrm{h}, & \text{at} \quad z &= -H+h. \end{aligned} \tag{4.3}$$

Here $\boldsymbol{\tau}_\mathrm{wind}$ is the wind-induced shear stress, ρ the density of water, h the sea bed topography, S the slip parameter (Maas and Van Haren, 1987) and finally, $\boldsymbol{\tau}$ is the bed shear stresses due to wind-driven and tidal currents. The wind-induced shear stress $\boldsymbol{\tau}_\mathrm{wind}$ at the sea surface is given by

$$\boldsymbol{\tau}_\mathrm{wind} = \rho_\mathrm{a} C_d |\mathbf{U}_\mathrm{wind}| \mathbf{U}_\mathrm{wind}, \tag{4.4}$$

where $\mathbf{U}_\mathrm{wind}$ is the horizontal wind velocity vector at 10 m above the sea surface, $C_d = (0.75 + 0.067|\mathbf{U}_\mathrm{wind}|)10^{-3}$ is a friction factor (Makin et al., 1995) and ρ_a is the air density. The wind vector has a magnitude $|\mathbf{U}_\mathrm{wind}|$ and an angle θ_wind with respect to the x-axis, see Figure 4.2. The forcing term F_x is chosen such that the tidal flow, over a flat bed and in absence of wind-driven flow, satisfies

$$\frac{1}{H}\int_{-H}^{0} \mathbf{u}_\mathrm{h}\,\mathrm{d}z = [U_\mathrm{M2}, 0]^T \sin(\sigma_\mathrm{t} t), \tag{4.5}$$

where, U_M2 is the depth-averaged tidal velocity amplitude and σ_t the tidal angular frequency. Note that in Eq.(4.5), we have chosen symmetrical tidal flow but additional components could be forced as well.

The waves are monochromatic, with a prescribed period and energy flux component in x-direction. Wave kinematics are modeled by linear wave theory (e.g. Mei, 1989), including local and instantaneous adaptation due to shoaling and refraction over the varying water depth. Wave diffraction and wave-current interactions are excluded, the latter because typical wave speeds ($\sim$10 m/s) are well above the current speeds ($<$1 m/s). The total bed shear stress due to both wind waves and the currents

is modeled as the sum of the two shear stress contributions due to currents and waves, i.e.

$$\boldsymbol{\tau}_{\mathrm{cw}} = \boldsymbol{\tau} + \boldsymbol{\tau}_{\mathrm{w}}. \tag{4.6}$$

Here $\boldsymbol{\tau}$ is as defined in equation (4.3), whereas the wave-induced bed shear stress is given by

$$\boldsymbol{\tau}_{\mathrm{w}} = \frac{1}{2}\rho f_{\mathrm{w}} |\mathbf{u}_{\mathrm{w}}| \mathbf{u}_{\mathrm{w}}, \tag{4.7}$$

where f_{w} is a wave friction factor (Nielsen, 1992) and $\mathbf{u}_{\mathrm{w}}$, the near bed wave orbital velocity vector, is given by

$$\mathbf{u}_{\mathrm{w}} = \frac{\mathbf{k}_{\mathrm{w}}}{|\mathbf{k}_{\mathrm{w}}|} \frac{\sigma_{\mathrm{w}} H_{\mathrm{w}} \cos(\sigma_{\mathrm{w}} t)}{2 \sinh(|\mathbf{k}_{\mathrm{w}}|(H-h))}. \tag{4.8}$$

Here, $\mathbf{k}_{\mathrm{w}}$ is the local wave vector, σ_{w} the wave angular frequency and H_{w} the local wave height. The wave period is given by $T = 2\pi/\sigma_{\mathrm{w}}$. The magnitude of the wave vector $\mathbf{k}_{\mathrm{w}}$ is determined by the dispersion relation

$$\sigma_{\mathrm{w}}^2 = g|\mathbf{k}_{\mathrm{w}}| \tanh(|\mathbf{k}_{\mathrm{w}}|(H-h)), \tag{4.9}$$

and the wave propagation angle is given by Snell's law:

$$\frac{\sin\theta_{\mathrm{wave}}}{c} = \frac{\sin\theta_{\mathrm{wave0}}}{c_0}, \tag{4.10}$$

where the θ_{wave} is defined as the angle between the x-axis and the propagation direction of the waves, see Figure 4.2, the wave celerity is given by $c = \sigma_{\mathrm{w}}/|\mathbf{k}_{\mathrm{w}}|$. The quantities with subscript $_0$ denote the reference wave conditions, i.e. the wave conditions for the waves that would travel through the domain if the seabed were flat. Note that for large reference wave angles, Snell's law in equation (4.10), produces complex angles in sand wave troughs, which prevents us from using reference wave angles close to 90 degrees. The local wave height H_{w} is computed from wave energy conservation and reads

$$H_{\mathrm{w}} = \sqrt{\frac{c_{g,0}}{c_g}} \sqrt{\frac{\cos\theta_{\mathrm{wave0}}}{\cos\theta_{\mathrm{wave}}}} H_{\mathrm{w0}} \tag{4.11}$$

where the wave group speed c_g is given by

$$c_g = \left[\frac{1}{2} + \frac{|\mathbf{k}_{\mathrm{w}}|(H-h)}{\sinh(2|\mathbf{k}_{\mathrm{w}}|(H-h))}\right] c. \tag{4.12}$$

4.2.3 Sediment transport

Following Hulscher (1996), we consider bed load sediment transport only, which is modeled as a power law of the bed shear stress, including a slope correction term, favoring downhill transport, given by

$$\mathbf{q}_{\mathrm{b}} = \alpha_{\mathrm{b}} |\boldsymbol{\tau}_{\mathrm{cw}}|^{\beta_{\mathrm{b}}} \left(\frac{\boldsymbol{\tau}_{\mathrm{cw}}}{|\boldsymbol{\tau}_{\mathrm{cw}}|} - \lambda \boldsymbol{\nabla}_{\mathrm{h}} h \right). \tag{4.13}$$

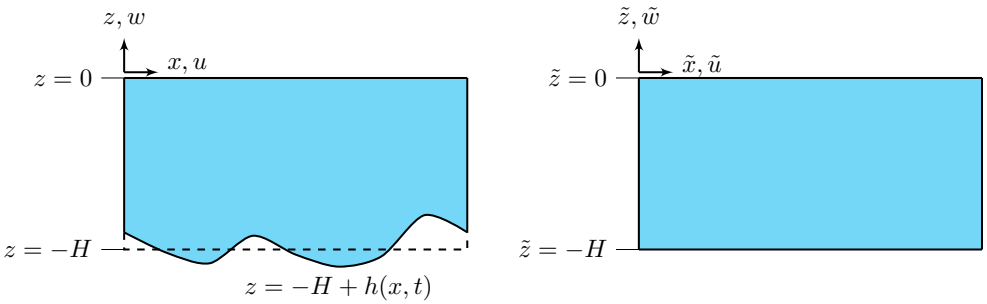

Figure 4.3: The transformation from the Cartesian (x, z) model domain towards the rectangular $(\tilde{x}, \tilde{z})$ model domain in which the transformed model equations will be solved numerically.

Here $\mathbf{q}_\mathrm{b}$ is the sediment transport flux, α_b is the bed load coefficient derived from Van Rijn (1993), β_b the exponent that expresses the nonlinearity of the bed load transport and λ is the slope correction parameter.

4.2.4 Bed evolution

The bed evolution satisfies the Exner equation for sediment conservation

$$(1-p)\frac{\partial h}{\partial t} = -\boldsymbol{\nabla}_\mathrm{h} \cdot \langle \mathbf{q}_\mathrm{b} \rangle, \tag{4.14}$$

where p is the bed porosity. Furthermore, $\langle \cdot \rangle$ denotes that we use the wave and tidally averaged sediment flux for seabed evolution, as a scaling analysis (Campmans et al., 2017) has demonstrated that we may consider separation of timescales. In our model we distinguish between three timescales: Firstly that of the wind waves (3-10 seconds), secondly that of the tidal current ($\sim$12 hours) and thirdly that of morphodynamic changes (months to years). On the intra-wave timescale the shear stress due to the currents is kept constant, and the sediment transport equation (4.13) is evaluated at a number of points in the wave cycle and then averaged over one wind wave period. Likewise, the morphological timescale is much longer than the tidal period, hence the seabed is kept constant on the hydrodynamic timescale. The sediment flux on the hydrodynamic timescale is then tidally averaged to obtain the bed evolution at the morphological timescale.

4.3 Solution method

The morphodynamic model is solved in several steps. First, the hydrodynamic model equations are transformed to a rectangular domain. Second, the hydrodynamic model equations are discretized, and numerically integrated over time. Thirdly, the sediment transport is computed. Finally, the seabed evolution is computed.

4.3.1 Coordinate transform

Following Van den Berg et al. (2012), we transform the hydrodynamic model equations from the Cartesian horizontal coordinate x and vertical coordinate z to coordinates $\tilde{x}$ and $\tilde{z}$ such that the transformed domain is rectangular and hence easier to discretize. The coordinate transformation is given by

$$\tilde{x} = x, \qquad \tilde{z} = H\frac{z}{H-h}, \tag{4.15}$$

and shown in Figure 4.3. This transformation uniquely maps coordinates to the transformed coordinate set, because the determinant of the transformation Jacobian

$$\mathcal{J} = \frac{\partial(\tilde{x},\tilde{z})}{\partial(x,z)} = \begin{bmatrix} \frac{\partial\tilde{x}}{\partial x} & \frac{\partial\tilde{x}}{\partial z} \\ \frac{\partial\tilde{z}}{\partial x} & \frac{\partial\tilde{z}}{\partial z} \end{bmatrix} = \begin{bmatrix} 1 & 0 \\ \eta & \xi \end{bmatrix}, \tag{4.16}$$

is nonzero: $\det(\mathcal{J}) = \xi$. Here η and ξ are given by

$$\eta = H\frac{z}{(H-h)^2}\frac{\partial h}{\partial x}, \qquad \xi = \frac{H}{H-h}. \tag{4.17}$$

After the coordinate transformation a variable transformation is applied introducing $(\tilde{\mathbf{u}}_\mathrm{h}, \tilde{w})$ such that

$$\mathbf{u}_\mathrm{h} = \xi\tilde{\mathbf{u}}_\mathrm{h}, \qquad w = \tilde{w} - \eta\tilde{u}. \tag{4.18}$$

This variable transformation enables us to write the hydrodynamic model problem in conservative form:

$$\frac{\partial\tilde{u}}{\partial\tilde{x}} + \frac{\partial\tilde{w}}{\partial\tilde{z}} = 0, \tag{4.19}$$

$$\frac{\partial\tilde{u}}{\partial t} + \frac{\partial}{\partial\tilde{x}}(\tilde{\mathcal{F}}_{u,x}) + \frac{\partial}{\partial\tilde{z}}(\tilde{\mathcal{F}}_{u,z}) + \frac{g}{\xi}\frac{\partial\tilde{\zeta}}{\partial\tilde{x}} - \frac{\tilde{F}_x}{\xi} = 0, \tag{4.20}$$

$$\frac{\partial\tilde{v}}{\partial t} + \frac{\partial}{\partial\tilde{x}}(\tilde{\mathcal{F}}_{v,x}) + \frac{\partial}{\partial\tilde{z}}(\tilde{\mathcal{F}}_{v,z}) - \frac{\tilde{F}_y}{\xi} = 0, \tag{4.21}$$

where the fluxes $\tilde{\mathcal{F}}$ are given by

$$\begin{aligned} \tilde{\mathcal{F}}_{u,x} &= \xi\tilde{u}^2, \\ \tilde{\mathcal{F}}_{u,z} &= \xi\tilde{u}\tilde{w} - \xi^2 A_\mathrm{v}\frac{\partial\tilde{u}}{\partial\tilde{z}}, \\ \tilde{\mathcal{F}}_{v,x} &= \xi\tilde{v}\tilde{u}, \\ \tilde{\mathcal{F}}_{v,z} &= \xi\tilde{v}\tilde{w} - \xi^2 A_\mathrm{v}\frac{\partial\tilde{v}}{\partial\tilde{z}}. \end{aligned} \tag{4.22}$$

with corresponding transformed boundary conditions given by

$$\begin{aligned} \tilde{w} &= 0, & \xi^2 A_\mathrm{v}\frac{\partial\tilde{\mathbf{u}}_\mathrm{h}}{\partial\tilde{z}} &= \frac{\boldsymbol{\tau}_\mathrm{wind}}{\rho}, & &\text{at} \quad \tilde{z} = 0, \\ \tilde{w} &= 0, & \frac{\boldsymbol{\tau}}{\rho} \equiv \xi^2 A_\mathrm{v}\frac{\partial\tilde{\mathbf{u}}_\mathrm{h}}{\partial\tilde{z}} &= \xi S\tilde{\mathbf{u}}_\mathrm{h}, & &\text{at} \quad \tilde{z} = -H. \end{aligned} \tag{4.23}$$

Note that $\eta = 0$ at $\tilde{z} = 0$ and $\eta = \xi\frac{\partial h}{\partial x}$ at $\tilde{z} = -H$.

4.3.2 Discretization

Hydrodynamics

The transformed hydrodynamic model problem is discretized using a finite difference method on a staggered grid, shown in Figure 4.4, where discrete horizontal velocities $\tilde{\mathbf{u}}_{\mathrm{h},i,j} = (\tilde{u}_{i,j}, \tilde{v}_{i,j})^T$ are defined at points $[\tilde{x}_i, \tilde{z}_j] = [(i-1)\Delta\tilde{x}, (j-\frac{1}{2})\Delta\tilde{z} - H]$ for $[1 \leq i \leq I, 1 \leq j \leq J]$ and discrete vertical velocities $\tilde{w}_{i,j}$ are defined at points $[\tilde{x}_i, \tilde{z}_j] = [(i-\frac{1}{2})\Delta\tilde{x}, j\Delta\tilde{z} - H]$ for $[1 \leq i \leq I, 1 \leq j \leq J+1]$. Here, $\Delta\tilde{x}$ and $\Delta\tilde{z}$ are the uniform step sizes in $\tilde{x}$- and $\tilde{z}$-direction and I and J are the number of discrete points in $\tilde{x}-$ and $\tilde{z}$-direction respectively. The spatial discretization of the hydrodynamics is given in Appendix A. The corresponding temporal integration is performed by forward Euler, in which the surface elevation is iteratively solved such that the continuity equation and the vertical velocity boundary conditions are fulfilled, as well as the conservation of ζ over the domain. For the hydrodynamic time integration, we use an adaptive step size Δt_{hyd}, such that $\Delta t_{\mathrm{hyd}} \leq 0.35/(\tilde{u}\tilde{\xi}/\Delta\tilde{x} + \tilde{w}\tilde{\xi}/\Delta\tilde{z})$ in each morphodynamic time step.

Sediment transport

The instantaneous discrete sediment flux in the x-direction is given by

$$q_{\mathrm{b},x,i} = \alpha_{\mathrm{b}} |\boldsymbol{\tau}_{\mathrm{cw},i}|^{\beta_{\mathrm{b}}} \left(\frac{\tau_{\mathrm{cw},x,i}}{|\boldsymbol{\tau}_{\mathrm{cw},i}|} - \lambda \frac{h_i - h_{i-1}}{\Delta x} \right), \tag{4.24}$$

where $\boldsymbol{\tau}_{\mathrm{cw},i}$ includes the spatially varying wave induced shear stress. The wind wave (64 points) and tidally averaged (typically 30,000 points) sediment flux is then used for the seabed evolution. To separately investigate the influence of the flow-induced and the slope-induced sediment transport on the sand wave evolution we write $q_{\mathrm{b},x,i} = q_{\mathrm{b},x,i,\mathrm{fe}} + q_{\mathrm{b},x,i,\mathrm{se}}$ with

$$q_{\mathrm{b},x,i,\mathrm{fe}} = \alpha_{\mathrm{b}} |\boldsymbol{\tau}_{\mathrm{cw},i}|^{\beta_{\mathrm{b}}} \frac{\tau_{\mathrm{cw},x,i}}{|\boldsymbol{\tau}_{\mathrm{cw},i}|} \qquad \text{and} \qquad q_{\mathrm{b},x,i,\mathrm{se}} = -\lambda \alpha_{\mathrm{b}} |\boldsymbol{\tau}_{\mathrm{cw},i}|^{\beta_{\mathrm{b}}} \frac{h_i - h_{i-1}}{\Delta x}, \tag{4.25}$$

respectively.

4.3.3 Bed evolution

The bed evolution equation (4.14) is discretized by using a semi-implicit scheme

$$(1-p)\frac{h_i^{n+1} - h_i^n}{\Delta t_{\mathrm{mor}}} = -\left[\frac{\langle q_{\mathrm{b},x,i+1,\mathrm{fe}}^n \rangle - \langle q_{\mathrm{b},x,i,\mathrm{fe}}^n \rangle}{\Delta x} - \alpha_{\mathrm{b}}\lambda \frac{\langle |\boldsymbol{\tau}_{\mathrm{cw},i+1}^n|^{\beta_{\mathrm{b}}} \rangle \left[\frac{h_{i+1}^n - h_i^n}{2\Delta x} + \frac{h_{i+1}^{n+1} - h_i^{n+1}}{2\Delta x} \right] - \langle |\boldsymbol{\tau}_{\mathrm{cw},i}^n|^{\beta_{\mathrm{b}}} \rangle \left[\frac{h_i^n - h_{i-1}^n}{2\Delta x} + \frac{h_i^{n+1} - h_{i-1}^{n+1}}{2\Delta x} \right]}{\Delta x} \right], \tag{4.26}$$

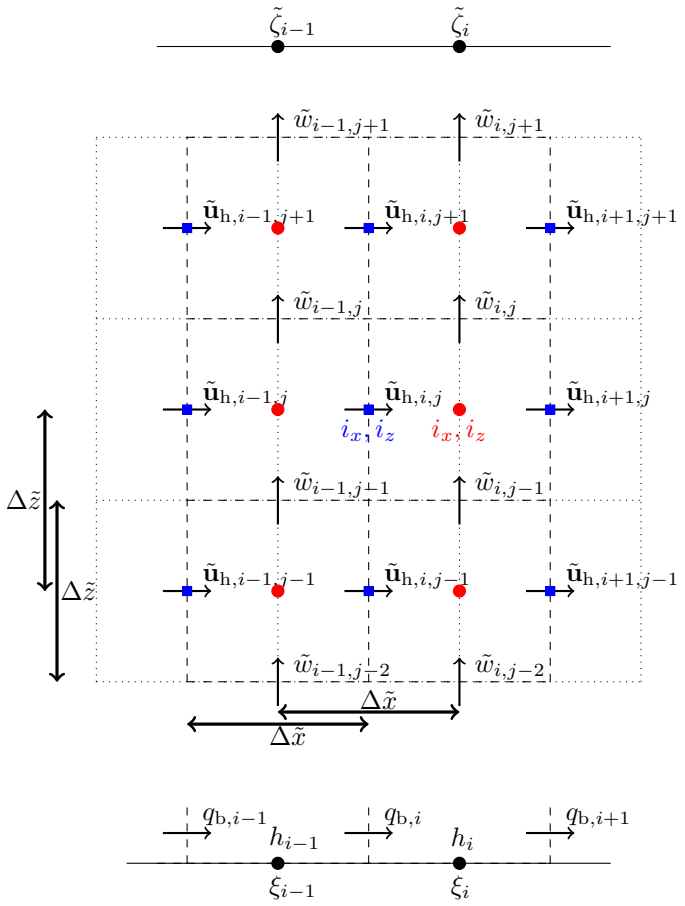

Figure 4.4: The unknowns $\tilde{\mathbf{u}}_{\mathrm{h}} = (\tilde{u}, \tilde{v})^T$ and $\tilde{w}$ are discretized in the model domain using a staggered grid. The red circles indicate locations were the discrete continuity equations are evaluated and the blue squares indicate the locations were the discrete momentum equations are evaluated. The grid spacing is equidistant with $\Delta\tilde{x}$ and $\Delta\tilde{z}$ spacing in the horizontal and vertical direction, respectively.

Table 4.1: The parameter settings used for the various model runs.

Description	Symbol	Typical value	Unit
Tidal velocity amplitude	U_{M2}	0.5	m/s
Tidal angular frequency	σ_{t}	$1.41 \cdot 10^{-4}$	rad/s
Vertical eddy viscosity	A_{v}	0.04	m^2/s
Slip parameter	S	0.01	m/s
Bed porosity	p	0.4	-
Gravitational acceleration	g	9.81	$\mathrm{m/s}^2$
Water density	ρ	1020	$\mathrm{kg/m}^3$
Air density	ρ_{a}	1.225	$\mathrm{kg/m}^3$
Wave friction factor	f_{w}	0.1	-
Mean water depth	H	30	m
Bed load coefficient	α_{b}	$1.56 \cdot 10^{-5}$	$\mathrm{m}^{\beta_{\mathrm{b}}+2}\mathrm{s}^{2\beta_{\mathrm{b}}-1}\mathrm{kg}^{-\beta_{\mathrm{b}}}$
Bed load exponent	β_{b}	1.5	-
Slope correction parameter	λ	1.5	-

where time is discretized by $t_n = n\Delta t_{\mathrm{mor}}$, and the two terms in the bed load transport formula (4.24) are treated separately. The bed shear stress is explicit in this scheme whereas the seabed gradient is discretized using an implicit Crank-Nicolson type of approach. This implicit scheme provides stability of the slope effect for larger morphodynamic time steps compared to those in a fully explicit scheme. The morphodynamic time step Δt_{mor} typically ranges from a week to a month. Finally, the conservative flux formulation in equation (4.26) guarantees conservation of sediment.

4.4 Results

We first compare the nonlinear sand wave model with the linear stability analysis for small-amplitude sand waves (section 4.4.1). Next, we investigate the evolution of sand waves towards equilibrium for different storm conditions on a limited domain size (section 4.4.2). Then we show how our model performs on a much longer domain with a random initial perturbation, such that the domain length is less restrictive for the sand wave wavelength and variations in the sand wave pattern appear (section 4.4.3). Finally we show the effect of intermittent storm occurrence on sand wave dynamics (section 4.4.4). The used parameter settings, chosen to be consistent with Campmans et al. (2017), are shown in Table 4.1, and an overview of simulations for the different storm processes is shown in Table 4.2. For clarity, we restrict to symmetrical tidal conditions, with asymmetries occurring due to wind forcing. The number of discrete points in the computations in the horizontal is $I = 64$ for the limited domain size and $I = 512$ for the longer domain size, in the vertical $J = 20$ points are used.

Table 4.2: Overview of simulations, forcing conditions per run and the sand wave height and migration rates at the end of the simulations. *The migration rate corresponding with the linear line plotted in the corresponding figure. **The net long term migration rate.

Figure	μ [-]	L [m]	H_{w0} [m]	T [s]	θ_{wave0} [°]	$\lvert\mathbf{U}_{wind}\rvert$ [m/s]	θ_{wind} [°]	h_{cr} [m]	h_{tr} [m]	h_{tot} [m]	c_{mig} [m/yr]
4.6(a)	-	350	-	-	-	-	-	15.3	-8.5	23.7	0
4.6(b)	-	350	2	7	0	-	-	7.4	-10.1	17.5	0
4.6(c)	-	350	-	-	-	10	0	12.0	-8.1	20.1	14.5
4.6(d)	-	350	2	7	0	10	0	6.1	-6.5	12.6	34.3
4.7/4.8(a)	-	350	-	-	-	10	0	12.0	-8.1	20.1	14.5
4.7/4.8(b)	-	350	-	-	-	10	30	12.6	-8.1	20.6	11.8
4.7/4.8(c)	-	350	-	-	-	10	60	13.7	-8.4	22.1	6.1
4.7/4.8(d)	-	350	-	-	-	10	90	14.3	-8.7	22.9	0
	-	350	2	7	0	-	-	7.4	-10.1	17.5	0
Section 4.4.2	-	350	2	7	30	-	-	7.3	-10.1	17.4	0
(text only)	-	350	2	7	70	-	-	7.3	-9.6	16.9	0
	-	350	2	7	80	-	-	8.4	-8.9	17.4	0
4.9(a)	-	4000	-	-	-	-	-	25.6	-9.5	34.0	∼0
4.9(b)	-	4000	2	7	0	-	-	15.1	-9.6	24.7	∼0
4.9(c)	-	4000	-	-	-	10	0	25.2	-8.8	33.9	19*
4.9(d)	-	4000	2	7	0	10	0	14.6	-9.5	24.1	52*
4.6/4.10(a)	0	350	-	-	-	-	-	15.3	-8.5	23.7	0
4.10(b)	1/52	350	2/-	7/-	0/-	10/-	0/-	14.9	-9.0	23.9	0.3**
4.10(c)	1/12	350	2/-	7/-	0/-	10/-	0/-	13.9	-9.6	23.5	1.3**
4.10(d)	1/6	350	2/-	7/-	0/-	10/-	0/-	12.8	-9.8	22.5	2.8**
4.10(e)	1/2	350	2/-	7/-	0/-	10/-	0/-	9.4	-8.8	18.1	11.3**
4.10(f)	1	350	2	7	0	10	0	6.1	-6.5	12.6	34.3

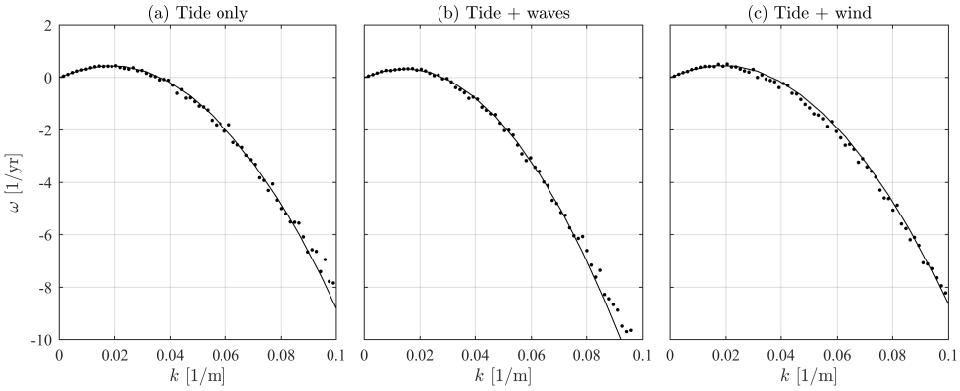

Figure 4.5: Comparison of our nonlinear model results (dotted) for small-amplitudes with the linear stability model results (solid). Here the growth rate ω is plotted as function of the topographic wavenumber, for three conditions: (a) Tide only, (b) Tide + waves and (c) Tide + wind.

4.4.1 Comparison with linear stability analysis

Our nonlinear sand wave model and the linear study by Campmans et al. (2017) are both based on the same model formulation. Hence, in the linear regime both linear stability analysis and our nonlinear sand wave model should give the same solution. Linear stability analysis predicts exponential growth/decay and migration of sinusoidal bed shapes according to $h(x,t) = \hat{h}_{\text{init}} \exp(\omega t) \cos(k[x - c_{\text{mig}} t])$ with growth rate ω and migration rate c_{mig}, which are both functions of topographic wavenumber k and other model parameters. Therefore, to make the model results comparable we have run the nonlinear model with a small-amplitude white-noise seabed perturbation and using Fourier analysis we have computed the corresponding growth rate per wavenumber. The growth rates from both the linear stability analysis and the nonlinear model are shown in Figure 4.5 for three different conditions: tide only, tide+waves and tide+wind. Both models produce the same small-amplitude growth behavior, i.e. the FGM properties for tide only are a wavelength of 335 m and growth rate of 0.44 1/yr, for tide+waves a wavelength of 419 m and growth rate of 0.33 1/yr and for tide+wind a wavelength of 335 m and a growth rate of 0.45 1/yr.

4.4.2 Equilibrium sand waves with different forcing conditions

On a periodic domain of 350 m length we investigate the evolution of a 1 m amplitude sinusoidal seabed perturbation, the wavelength of which corresponds with the length of the domain. By choosing the domain length to be equal to the wavelength of the bed form, this property cannot be varied whereas others, such as shape, height and migration can be investigated. The chosen domain length is a typical wavelength observed in the field and corresponds approximately to the FGM wavelength resulting from linear stability analysis for the three conditions: tide only, tide+waves and

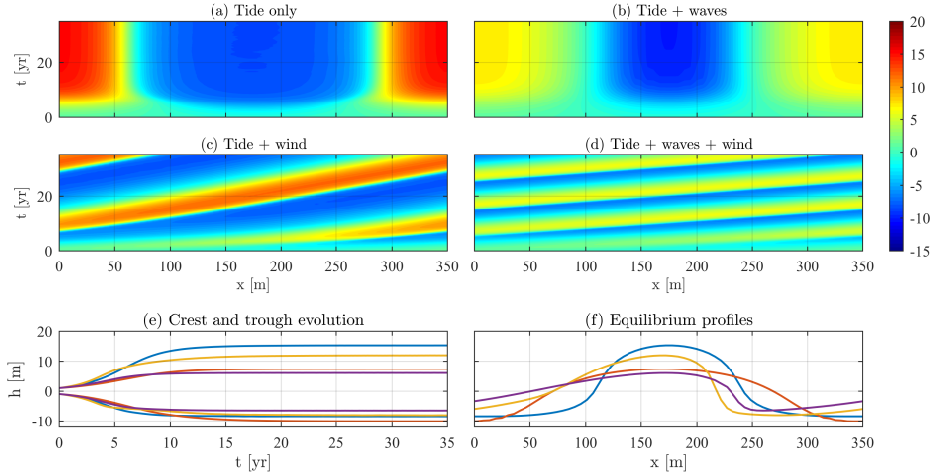

Figure 4.6: The seabed evolution in time and space for four different forcing conditions: (a) tide only, (b) tide+waves, (c) tide+wind and (d) tide+waves+wind. (e) The crest and trough elevation evolution and (f) equilibrium profiles for four different forcing conditions: (blue) tide only, (red) tide+waves, (yellow) tide+wind and (purple) tide+waves+wind. The profiles have been shifted horizontally such that the crest locations coincide. The parameter settings and forcing conditions are shown in Table 4.1 and 4.2, respectively.

tide+wind (see Figure 4.5).

Wave and wind influence

Figure 4.6 shows the time-evolution of the bed perturbation towards its fully grown state, for four different conditions: (a) tide only, (b) tide+waves, (c) tide+wind and (d), tide+waves+wind. Here tide is a 0.5 m/s depth-averaged symmetrical M2 constituent, waves have 2 m height and 7 s period and wind velocity is 10 m/s, all parallel to the x-directions ($\theta_{\text{waves0}} = \theta_{\text{wind}} = 0°$). The lower panels of Figure 4.6 show the evolution of the crest and trough elevation and the resulting (near) equilibrium profiles.

In each of the model runs, the seabed perturbation starts to grow in amplitude. Initially the growth speed increases with increasing amplitude, but after a while the growth speed slows down and the sand waves asymptotically approach their fully grown states. If wind waves are included the final height is smaller. Both in the tide-only simulations and if waves are included, horizontal symmetry is preserved due to the symmetrical forcing. When adding wind-driven flow, the symmetry is broken, which leads to horizontal asymmetry and migration. The inverse of the slope $\mathrm{d}t/\mathrm{d}x$ of the crest/trough lines in the x-t diagram indicates migration speed. The steady migration rates towards the end of the simulations are given in Table 4.2. Initially, for small heights, the migration rate is relatively fast and then decreases with increasing sand wave height, the values in the steady regime being 14.5 and 34.3 m/yr. Also

for wind, the final sand wave height is less than in the tide only situation. If, in addition to the tidal flow, both wind waves and wind-driven flow are present, the final sand wave height decreases even further. In that case, the migration rate of the fully grown sand waves increases as compared with the tide-only and the tide+wind cases. Note that the wave enhancement of the migration rate is twofold: (1) Linear stability analysis already showed that waves enhance migration for small amplitudes and (2) we now find that the reduction of the sand wave height due to waves also accompanies an increase in migration speed.

Influence of wind direction

In the previous section we have seen that wind-driven flow in the direction of the tidal flow, causes sand wave migration and decreases sand wave height. In this section we investigate the influence of the angle of the wind with respect to the tidal current. In Figure 4.7 the seabed evolution towards equilibrium profiles is shown for four simulations where a 10 m/s wind directed in four different directions with respect to the tidal flow: $\theta_{\text{wind}} = 0°, 30°, 60°$ and $90°$. The model run with $\theta_{\text{wind}} = 0°$ was already shown in the previous section, and is shown here again as reference. The migration rate is shown in Figure 4.8. Once the sand wave profile is approximately in equilibrium the entire profile migrates at the same speed, which is 14.5 m/yr, 11.8 m/yr, 6.1 m/yr and 0 m/yr for (a)-(d) respectively. For increasing wind angle the sand wave height increases, the migration rate decreases and also bed form asymmetry decreases. The decrease in migration rate is twofold, firstly the wind-driven flow component in the migration direction gets smaller as the wind angle increases and secondly, in section 4.4.2, we have seen that the migration rate decreases with increasing sand wave height. For wind perpendicular to the tidal flow direction the wind-driven flow does not break the symmetry in the x-direction and therefore the bed form does not migrate. While the seabed profile is developing the migration rates of crest and trough are different because the profiles are becoming horizontally asymmetric. Here we should mention that the forcing conditions are no longer symmetrical in the y-direction, meaning that sand wave orientation in principle no longer has to be perpendicular to the x-direction. However, here we still assume the sand wave profile to be uniform in y-direction. The values of the migration rates found in equilibrium, roughly satisfy a cosine relationship, i.e. $c_{mig,eq}(\theta_{\text{wind}}) \approx c_{\text{mig,eq}}(0°) \cos\theta_{\text{wind}}$.

Influence of wave direction

The influence of wave direction has been investigated for four wave propagation directions $\theta_{\text{wave0}} = 0°, 30°, 70°$ and $80°$, respectively. Simulations, not shown here, indicate that the evolution of the seabed is insensitive to small wave angles. For larger wave angles the crests become slightly higher, the troughs turn out to be wider and shallower and the sand wave height slightly increases.

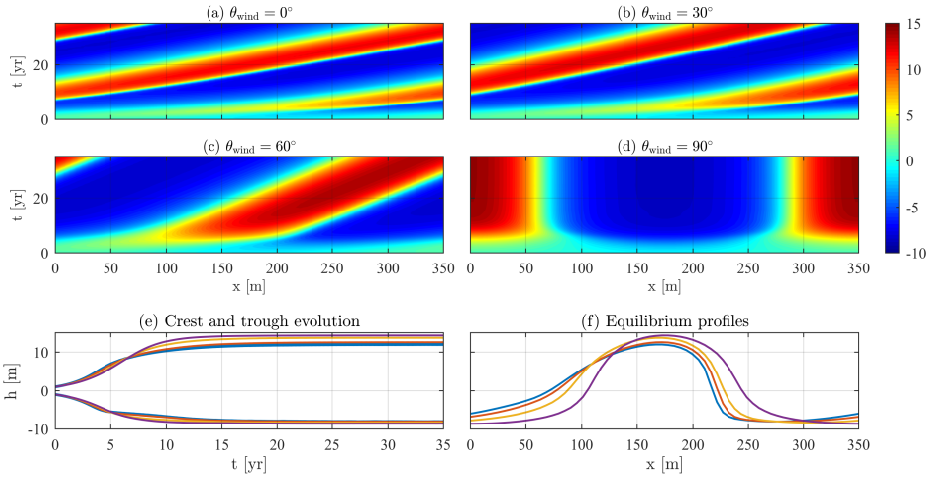

Figure 4.7: Same as Fig. 4.6, but now for four wind angles in the tide+wind case: (blue) $\theta_{\text{wind}} = 0°$, (red) $\theta_{\text{wind}} = 30°$, (yellow) $\theta_{\text{wind}} = 60°$ and (purple) $\theta_{\text{wind}} = 90°$.

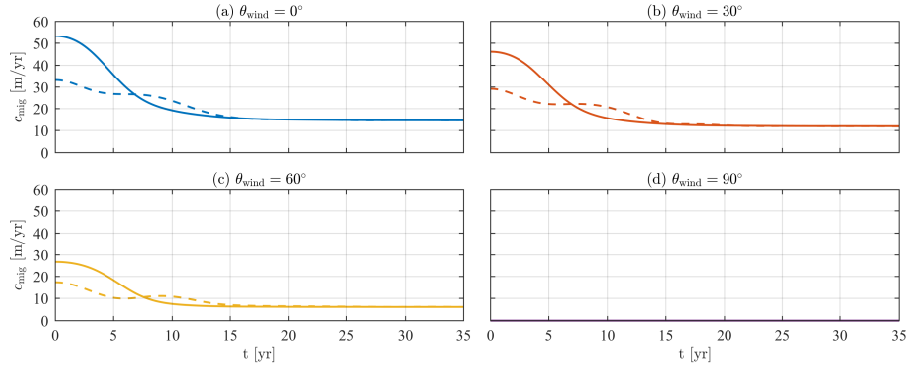

Figure 4.8: The migration rate of sand wave crest (solid) and trough (dashed) for four different wind angles: $\theta_{\text{wind}} = 0°$, 30°, 60° and 90°. The parameter settings and forcing conditions are shown in Table 4.1 and 4.2, respectively.

4.4.3 Sand wave evolution on a long domain

In the previous sections we have investigated the influence of waves and wind on a domain with a length corresponding with the wavelength of typical observed sand waves. Due to this choice sand waves were unable to freely modify their wavelengths. By increasing the domain length to 4 km, sand waves of 350 m are now more free to modify their wavelength as they evolve, without changing the periodic boundary conditions of our model. The model is run with four forcing conditions: (a) tide only, (b) tide+waves, (c) tide+wind, and (d) tide+waves+wind (see Table 4.2). The initial bed profile for each of the four runs is identical: the sum of sinusoidal perturbations of all possible spatial frequencies with an equally small amplitude and a random phase shift, such that all possible modes are equally present at the start of the simulation.

The time-evolution of the sand wave profiles and height is shown in Figure 4.9. Initially, the modes with large wave numbers rapidly decay, whereas those with lower wave numbers develop into a dynamic sand wave field. In a time period of about 5-15 years in each of the model runs a sand wave pattern has developed which shows similarities with observed sand wave fields. The semi-random initial topography enables showing how variations in the sand wave field could develop. Initially the FGM, predicted by linear stability analysis (Campmans et al., 2017), with a wavelength of around 330-420 m dominates other modes. However, as time progresses the dominant wavelength increases towards roughly 600-1000 m. It should be noticed that the sand wave profiles after 20 years, shown in Figure 4.9(f), are not yet in equilibrium. On time scales much longer than those plotted here, the system seems to evolve to a single bed form with a wavelength equal to the domain size. This will be further discussed in Section 4.5.

In these simulations we see variations in the sand wave field, where sand waves of different wavelengths are interacting with each other, causing variations in sand wave migration. The migration rate of a relatively small sand wave indicated with the gray dash dotted line in Figure 4.9(c) corresponds to a migration rate of -8 m/yr, while another sand wave (black dash dotted) migrates at 19 m/yr. Even in the symmetrically forced model runs, shown in Figure 4.9(a-b), minor migration rates in various directions can be observed due to the pattern interactions. In the model runs with wind-driven flow, large migration rates can be observed, with substantial variations in migration speed for the individual sand waves, especially when sand waves overtake each other. These sand wave interactions can result in significant seabed level changes within a relatively short timespan.

4.4.4 Effects of intermittent storms

In the previous sections we have investigated the effect of constant wind and wave conditions on sand wave dynamics. However, in reality storms occur intermittently. In this section we investigate the effect of a synthetic regular intermittent storm climate. Two conditions, fair-weather and a storm condition, are alternated on a yearly periodic basis. The fair-weather coincides with the tide only situation. The storm condition consist of 2 m high waves of 7 s period propagating parallel to the x-axis and

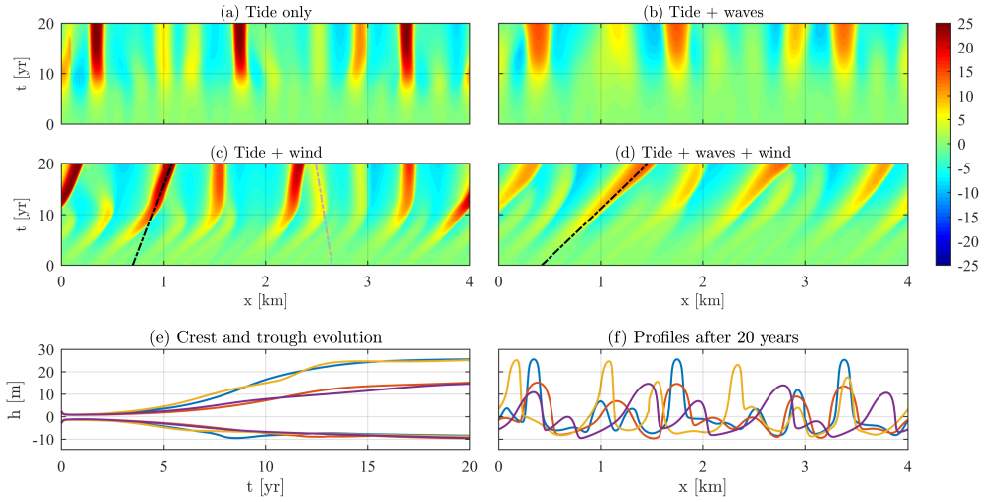

Figure 4.9: The evolution of the seabed for four different forcing conditions: (a) tide only, (b) tide+waves, (c) tide+wind and (d) tide+waves+wind. The crest and trough elevation evolution (e) and the profiles after 20 years (f) are shown in the lower two panels, in which the four different forcing conditions are: (blue) tide only, (red) tide+waves, (yellow) tide+wind and (purple) tide+waves+wind. The parameter settings and forcing conditions are shown in Table 4.1 and 4.2, respectively. The dash dotted lines correspond to a constant migration speed indicated in Table 4.2. The gray dash dotted line (c) corresponds to a migration rate opposite to the general trend.

10 m/s wind parallel to the x-axis. In Figure 4.10 the sand wave evolution is plotted for constant fair-weather, constant storm and alternating storm and fair-weather conditions. Four storm duration intervals are shown, 1 week storm ($\mu = 1/52$), 1 month ($\mu = 1/12$), 2 months storm ($\mu = 1/6$) and 6 months storm ($\mu = 1/2$). Where μ is the ratio of the storm duration over the overall time period. The intermittent storm sequences of 1 week, 1 month and 2 month storm conditions show migration rates of 0.3, 1.3 and 2.8 m/yr respectively, which are comparable to those reported in literature (e.g., Fenster et al., 1990; Van Dijk and Kleinhans, 2005). A clear difference in sand wave crest and trough elevation between constant fair-weather ($\mu = 0$) and constant storm ($\mu = 1$) conditions is observed. For each of the intermittent storm sequences the trough and especially the crest show oscillating elevations, which lie in between those of the constant fair-weather and constant storm conditions. These oscillations result from the continuous adjustment towards equilibrium states that periodically switch from 'high' (tide only, i.e. no waves or wind) to 'low' (tide+waves+wind). Note that the crest and trough elevations of the 6 month simulation are not midway but more towards the constant storm simulation. Figure 4.10(h) shows the maximum crest height and minimum trough depth as function of the storm duration μ. The migration rate that was obtained for the constant storm conditions is 34.3 m/yr, which is large compared to field observations. By including the storms intermittently for 1 and 2 months, the obtained migration speeds are 1.3 and 2.8 m/yr, respectively, which are realistic values. For these storm durations the reduction in crest height is 9% and 16%, respectively. Longer storm periods, i.e. 6 months or constant storm reduce the crest height by 39% and 60% respectively. This shows that even if storm conditions occur for a short period of time their influence is still of importance.

4.5 Discussion

Sand wave height still seems to be overestimated in our model, especially for the tide only situation. Note that we did not calibrate our model against field observations. Calibration with, for instance, the slope correction parameter could result in more realistic sand wave heights. However, our goal is to investigate whether storms could be a mechanism which is responsible for lowering sand wave heights.

The mechanism that is responsible for waves to reduce the sand wave growth rate can be explained by examining the bed load transport terms in equation (4.25). The magnitude of transport is nonlinearly dependent on the shear stress magnitude. This nonlinearity in sediment transport results in a net increase in transport due to increased wave stirring and since the slope induced transport is always directed downslope this term reduces the growth rate.

To clarify the saturation mechanism and the influence of waves and wind on the equilibrium height, we have conducted another set of simulations. Herein, we have computed for sinusoidally shaped initial topographies of various amplitudes, A_{sw}, the rate of change of the crest height $\partial h/\partial t|_{\mathrm{crest}}$ (after spin-up of the flow), divided by amplitude A_{sw}, as a function of the amplitude A_{sw}. Note that the rate of change divided by amplitude is equivalent to the growth rate in linear stability analysis, and

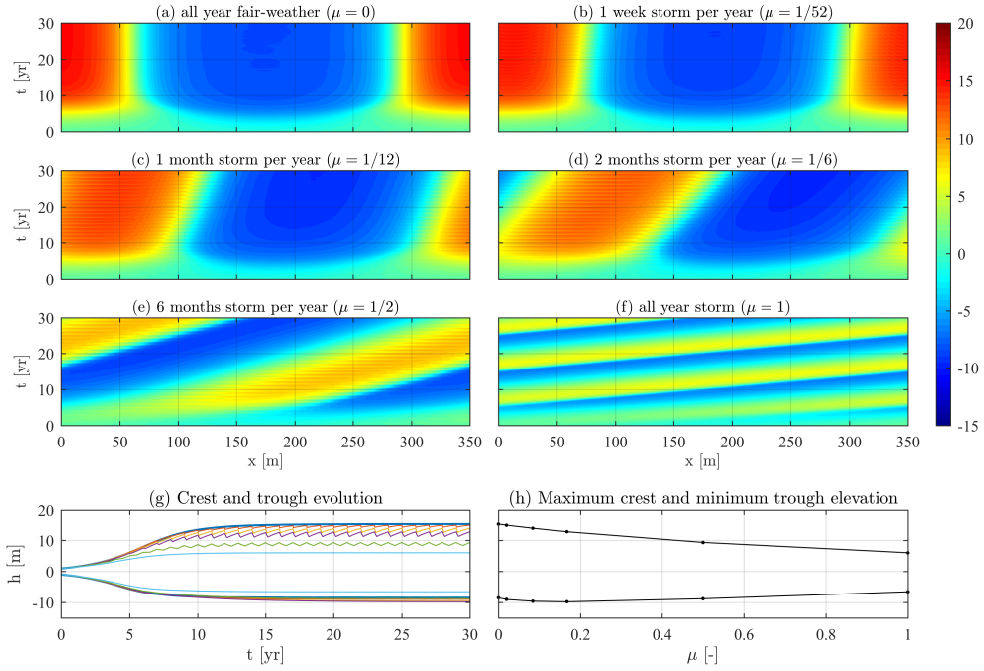

Figure 4.10: The evolution of the seabed for six different storm conditions: (a) all year fair-weather, (b) 1 week storm, (c) 1 month storm, (d) 2 months storm, (e) 6 month storm and (f) all year storm. The evolution of crest and trough elevation (g) is plotted for constant fair-weather conditions (blue), constant storm conditions (light blue) and alternating storm and fair weather conditions: one week per year storm (red), one month per year storm (yellow), two months per year storm (purple) and 6 months per year storm (green). The maximum crest and minimum trough elevation are plotted against the storm ratio in the synthetic storm sequence (h). The parameter settings and forcing conditions are shown in Table 4.1 and 4.2, respectively.

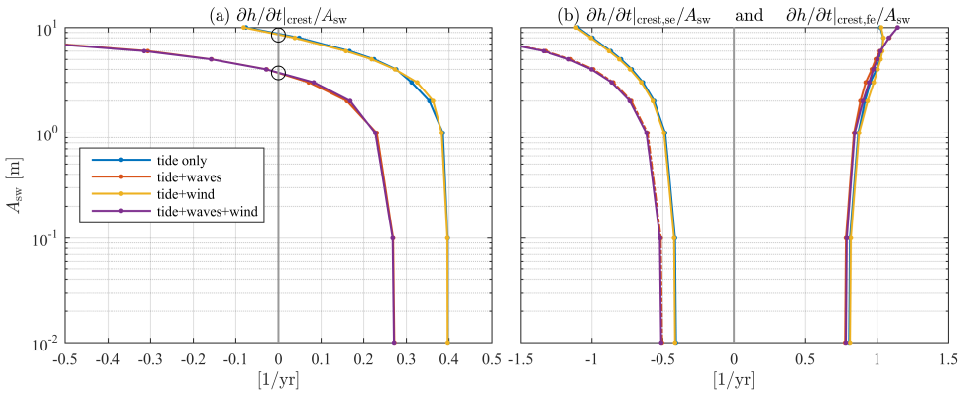

Figure 4.11: The divergence of sediment transport, scaled with the bed form amplitude A_{sw}, evaluated at the crest of sinusoidal bed forms as function of bed form amplitude A_{sw}. The total growth (a) is the sum of the slope-induced and flow-induced contributions (b). Four conditions have been investigated: tide only (blue), tide+waves (red), tide+wind (yellow) and tide+waves+wind (purple). The parameters and forcing conditions as in Figure 4.6. The zero crossings are indicated with a circle.

is thus expected to be constant for small amplitudes, and through nonlinear effects changes for larger amplitudes. Distinguishing the two contributions (flow-induced and slope-induced) introduced in Eq.(4.25), we have compared the four types of forcing conditions: tide only, tide+waves, tide+wind, tide+waves+wind. Importantly, by investigating a sinusoidal sand wave shape for all amplitudes, we avoid indirect effects through the evolution of the sand wave shape (which would be different for each forcing condition, thus obscuring comparison and interpretation). The result, shown in Fig.4.11, demonstrates the following:

- Nonlinear effects amplify the relative contributions due to flow and slope for increasing A_{sw} (otherwise all lines in Figure 4.11 would be vertical).
- This amplification is stronger for the slope-induced than for the flow-induced contribution, which explains the occurrence of an equilibrium. Note that this is not a formal equilibrium, because nonlinear effects tend to change the shape of the bed form.
- Finally, waves enhance the slope-induced contribution, which causes the equilibrium amplitude to shift to a lower value. Note that, restricting to the linear regime (A_{sw} small compared to mean water depth), this enhancement was already identified by Campmans et al. (2017).

Storm events occur randomly and have limited duration, while in our model the storm processes are mostly modeled steady. Therefore, the model results before Section 4.4.4 do not resemble the effect of a single storm event, but rather the theoretical equilibrium state to which the system would tend during a storm. Therefore, to gain

insight in intermittent storm processes, one storm condition has been alternated with fair-weather. Even when storms only occur for a short period of time, they have a relatively large effect on the behavior of sand waves (Figure 4.10). This observation emphasizes the importance of storm effects on sand wave dynamics.

Our model shows, in agreement with linear stability analysis, that wind-driven flow is able to cause sand wave migration. Since the sand wave shape becomes horizontally asymmetric the migration rate is initially different for the crest and trough. As the sand wave height increases the migration rate decreases, which is also obtained from data analysis (Knaapen, 2005) and is observed in modeling other morphological features, such as nearshore sand bars (Garnier et al., 2006). This suggests that migration rates predicted by linear stability analysis are expected to be higher than those of fully grown sand waves. Although sand wave migration speed decreases with increasing height, in long domain simulations with an initial random bed higher sand waves are found to overtake smaller sand waves. This seems counterintuitive. The hydrodynamic conditions around a smaller sand wave close to an approaching higher sand wave are influenced such that the higher sand wave migrates faster than the lower sand wave. Neighboring sand waves thus affect each others growth and migration behavior. Even for symmetrical flow conditions, i.e. tide only and tide+waves, small migration rates can be observed when neighboring sand waves attract or repel each other. For tide+wind conditions, smaller sand waves even migrate in the direction opposing the domain-averaged residual flow, showing that sand waves strongly interact with each other. Finally, note that variations in wind direction and intensity might cause the average migration rate to be significantly smaller than the values obtained here for a single wind condition.

Sand wave models, including the present one, still lack a mechanism that keeps sand waves from tending towards very long wavelengths. This is a fundamental problem in this type of morphodynamic model, as this is also observed for other bed features such as sand banks. We have limited the wavelength artificially by using a limited domain size, in order to investigate the influence of storm effects on sand wave dynamics. Mechanisms that might limit the wavelength may be found in horizontal variations of the tidal wave (we assume horizontal uniformity of the forcing on the length scale of the sand waves). Also interactions with other bed forms such as sand banks or mega ripples might be of importance. Stochastic variations in currents and waves might also affect the preferred wavelength.

4.6 Conclusion

We have developed an idealized nonlinear sand wave model that is able to simulate sand wave evolution from an initial small perturbation towards a fully developed equilibrium state. Using this model we are able to investigate storm effects on sand wave evolution. The modeled equilibrium sand waves in tide+wave+wind conditions become about 15 meter high, 600-1000 m in wavelength, migrate at about 50 m/yr and are formed in roughly 10 years. Our most important results are that wind waves and, to a lesser degree, wind-driven flow tend to decrease sand wave height, and wind-driven

flow causes asymmetry and migration. The wave-induced reduction in sand wave height is explained from the balance between flow-induced and slope-induced sediment transport contributions. Wind waves enhance the slope-induced sediment transport, leading to a reduction in equilibrium height. Waves as modeled here do not induce migration, but enhance sand wave migration due to other processes, such as wind-driven flow or tidal asymmetry (the latter not being included in this contribution). The direction of wind-driven flow affects horizontal asymmetry, height reduction and migration effects. Wind parallel to the tidal current results in the largest asymmetry, migration and height reduction, whereas perpendicular wind results in symmetrical sand waves that do not migrate and causes the smallest reduction in height. The wave angle appears to be of less importance, only for wave angles close to 90 degrees the wave angle seems to have an influence. Finally we show that short periods of storms can already have significant effects on sand wave height, and lead to realistic migration rates.

4.7 Acknowledgments

This work is part of the research programme SMARTSEA with project number 13275, which is (partly) financed by the Netherlands Organisation for Scientific Research (NWO). The numerical code can not be made available at submission (a condition by the funder), but the first author will facilitate code use for verification purposes should anybody seek this. We thank Daniel Calvete Manrique for his support and for facilitating a stay at Universitat Politècnica de Catalunya, Barcelona, Spain. We thank anonymous reviewers for their comments.

4.8 Appendix

4.9 Spatial hydrodynamic discretization

Here we describe how the transformed model equations have been discretized. The transformed continuity equation (4.19) is discretized by

$$\frac{\tilde{u}_{i+1,j} - \tilde{u}_{i,j}}{\Delta\tilde{x}} + \frac{\tilde{w}_{i,j} - \tilde{w}_{i,j-1}}{\Delta\tilde{z}} = 0. \tag{4.27}$$

The transformed momentum equations (4.20) are spatially discretized by

$$\begin{aligned}\frac{\partial\tilde{u}_{i,j}}{\partial t} &+ \frac{\tilde{\mathcal{F}}_{u,x,i+\frac{1}{2},j} - \tilde{\mathcal{F}}_{u,x,i-\frac{1}{2},j}}{\Delta\tilde{x}} + \frac{\tilde{\mathcal{F}}_{u,z,i,j+\frac{1}{2}} - \tilde{\mathcal{F}}_{u,z,i,j-\frac{1}{2}}}{\Delta\tilde{z}} \\ &+ \frac{g}{\xi_{i-\frac{1}{2}}}\frac{\tilde{\zeta}_i - \tilde{\zeta}_{i-1}}{\Delta\tilde{x}} - \frac{\tilde{F}_x}{\xi_{i-\frac{1}{2}}} = 0,\end{aligned} \tag{4.28}$$

$$\frac{\partial \tilde{v}_{i,j}}{\partial t} + \frac{\tilde{\mathcal{F}}_{v,x,i+\frac{1}{2},j} - \tilde{\mathcal{F}}_{v,x,i-\frac{1}{2},j}}{\Delta \tilde{x}} + \frac{\tilde{\mathcal{F}}_{v,z,i,j+\frac{1}{2}} - \tilde{\mathcal{F}}_{v,z,i,j-\frac{1}{2}}}{\Delta \tilde{z}} - \frac{\tilde{F}_y}{\xi_{i-\frac{1}{2}}} = 0. \tag{4.29}$$

Here we use linear interpolation to evaluate $\xi_{i-\frac{1}{2}}$ according to $\xi_{i-\frac{1}{2}} = \frac{1}{2}(\xi_{i-1} + \xi_i)$. The flux terms, as presented in equation (4.22), are discretized by

$$\begin{aligned}
\tilde{\mathcal{F}}_{u,x,i+\frac{1}{2},j} &= \xi_i \tilde{u}^{*2}_{i+\frac{1}{2},j} \\
\tilde{\mathcal{F}}_{v,x,i+\frac{1}{2},j} &= \xi_i \tilde{v}^{*}_{i+\frac{1}{2},j} \tilde{u}^{*}_{i+\frac{1}{2},j} \\
\tilde{\mathcal{F}}_{u,z,i,j+\frac{1}{2}} &= \xi_{i-\frac{1}{2}} \tilde{u}^{*}_{i,j+\frac{1}{2}} \tilde{w}_{i-\frac{1}{2},j} - \xi^2_{i-\frac{1}{2}} A_{\mathrm{v}} \frac{\tilde{u}_{i,j+1} - \tilde{u}_{i,j}}{\Delta \tilde{z}} \\
\tilde{\mathcal{F}}_{v,z,i,j+\frac{1}{2}} &= \xi_{i-\frac{1}{2}} \tilde{v}^{*}_{i,j+\frac{1}{2}} \tilde{w}_{i-\frac{1}{2},j} - \xi^2_{i-\frac{1}{2}} A_{\mathrm{v}} \frac{\tilde{v}_{i,j+1} - \tilde{v}_{i,j}}{\Delta \tilde{z}}.
\end{aligned} \tag{4.30}$$

Here linear interpolation is used to evaluate the vertical velocities that are required in between grid points, $\tilde{w}_{i-\frac{1}{2},j} = \frac{1}{2}\left(\tilde{w}_{i-1,j} + \tilde{w}_{i,j}\right)$. The state variables, $\tilde{\mathbf{u}}^{*}_{\mathrm{h},i,j}$, which are required at the inter-grid points, are computed using linear reconstruction including a so-called limiter function which improves the stability properties of the scheme (Van Leer, 1979). For instance, for the horizontal momentum flux the horizontal velocities on the left and right side of the interface are reconstructed using

$$\begin{aligned}
\tilde{u}^{L}_{i+\frac{1}{2},j} &= \tilde{u}_{i,j} + \frac{1}{2}\phi(r_{i,j})(\tilde{u}_{i+1,j} - \tilde{u}_{i,j}) \\
\tilde{u}^{R}_{i-\frac{1}{2},j} &= \tilde{u}_{i,j} - \frac{1}{2}\phi(r_{i,j})(\tilde{u}_{i+1,j} - \tilde{u}_{i,j}).
\end{aligned} \tag{4.31}$$

Here $\phi(r)$ is a limiter function, for which we choose the symmetric superbee limiter (Roe, 1986), given by

$$\phi(r) = \max(0, \max(\min(1, 2r), \min(2, r))), \tag{4.32}$$

where r is the ratio between the forward and backward difference, e.g. the horizontal difference ratio $r_{i,j}$ in Eq. (4.31) is given by

$$r_{i,j} = \frac{\tilde{u}_{i,j} - \tilde{u}_{i-1,j}}{\tilde{u}_{i+1,j} - \tilde{u}_{i,j}}. \tag{4.33}$$

Finally, the interface states used to evaluate the fluxes are determined by approximately solving the Riemann problem at each of the interface using the two states on either side of the interface, e.g.

$$\tilde{u}^{*}_{i+\frac{1}{2},j} = \begin{cases}
\tilde{u}^{L}_{i+\frac{1}{2},j} & \text{if} \quad \tilde{u}^{L}_{i+\frac{1}{2},j} > \tilde{u}^{R}_{i+\frac{1}{2},j} \quad \text{and} \quad s > 0 \\
\tilde{u}^{R}_{i+\frac{1}{2},j} & \text{if} \quad \tilde{u}^{L}_{i+\frac{1}{2},j} > \tilde{u}^{R}_{i+\frac{1}{2},j} \quad \text{and} \quad s < 0 \\
\tilde{u}^{L}_{i+\frac{1}{2},j} & \text{if} \quad \tilde{u}^{L}_{i+\frac{1}{2},j} < \tilde{u}^{R}_{i+\frac{1}{2},j} \quad \text{and} \quad \tilde{u}^{L}_{i+\frac{1}{2},j} > 0 \\
\tilde{u}^{R}_{i+\frac{1}{2},j} & \text{if} \quad \tilde{u}^{L}_{i+\frac{1}{2},j} < \tilde{u}^{R}_{i+\frac{1}{2},j} \quad \text{and} \quad \tilde{u}^{R}_{i+\frac{1}{2},j} < 0 \\
0 & \text{if} \quad \tilde{u}^{R}_{i+\frac{1}{2},j} > 0 > \tilde{u}^{L}_{i+\frac{1}{2},j}
\end{cases} \tag{4.34}$$

where s is the shock speed given by

$$s = \frac{1}{2}(\tilde{u}^L_{i+\frac{1}{2},j} + \tilde{u}^R_{i+\frac{1}{2},j}). \tag{4.35}$$

The boundary conditions are implemented using ghost cells, given by

$$\begin{aligned}
&\tilde{w}_{i,J} = 0, && \tilde{\mathbf{u}}^G_{\mathrm{h},i,J+1} = \tilde{\mathbf{u}}_{\mathrm{h},i,J} + \frac{\Delta\tilde{z}\boldsymbol{\tau}_{\mathrm{wind}}}{A_{\mathrm{v}}\rho\xi^2_{i-\frac{1}{2}}},\\
&\tilde{w}_{i,0} = 0, && \tilde{\mathbf{u}}^G_{\mathrm{h},i,0} = \tilde{\mathbf{u}}_{\mathrm{h},i,1}\frac{(\xi_{i-1}+\xi_i)A_{\mathrm{v}} - S\Delta\tilde{z}}{(\xi_{i-1}+\xi_i)A_{\mathrm{v}} + S\Delta\tilde{z}},\\
&\tilde{\mathbf{u}}^G_{\mathrm{h},I+1,j} = \tilde{\mathbf{u}}_{\mathrm{h},1,j}, && \tilde{\zeta}^G_0 = \tilde{\zeta}_I,
\end{aligned} \tag{4.36}$$

where ghost values are denoted by superscript ^{G}, and note that we start indexing with 1 for interior cells. The horizontal domain bounds are treated as periodic, i.e. the right most cells are seen as the left neighbors of the left most cell in the domain and vice versa. The discrete bed shear stresses are given by

$$\boldsymbol{\tau}_i = \frac{\rho S}{4}(\xi_{i-1}+\xi_i)(\tilde{\mathbf{u}}^G_{\mathrm{h},i,0} + \tilde{\mathbf{u}}_{\mathrm{h},i,1}). \tag{4.37}$$

Chapter 5

Discussion and Conclusions

5.1 Discussion

5.1.1 Scientific and societal context

Unraveling the dynamics of sand waves is an interesting topic from both an academic and engineering point of view. On the one hand, for academics it is fascinating to explain the mechanisms that form these seemingly simple rhythmic and well organized patterns that develop in a wide range of environmental conditions. On the other hand, various engineering applications actually suffer from the uncertainty posed by sand wave dynamics. This research is part of the SMARTSEA project* which particularly focuses on shipping safety in the North Sea, which is strongly affected by sand wave evolution. Given the present day knowledge on sand wave dynamics, frequent surveying is still required to guarantee shipping safety. Sand wave modeling improves our understanding of sand wave dynamics, improving the predictability and thus reducing the required surveying frequencies. As sand waves are part of a complex system involving a variety of processes at a wide scale of length and time scales, surveying will always be required. The work in this thesis improves the understanding of wave and wind within this complex morphodynamic system. It was found that wind waves reduce sand wave height and wind-driven flow induces migration and sand wave asymmetry. The two newly developed sand wave models may find application towards engineering purposes such as optimizing surveying frequencies required for shipping, and the planning and maintenance of pipelines, cables and wind farms. Finally, the models developed here form the basis for future research.

*The project was funded by NWO/TTW by the maritime TKI call, under project number 13275, entitled "SMARTSEA: Safe navigation by optimizing sea bed monitoring and waterway maintenance using fundamental knowledge of sea bed dynamics"

5.1.2 Idealized process-based modeling approach

In this research on wave and wind effects on sand wave dynamics other processes, which were already investigated by other researchers, were simplified. For example, a single grain size was used, whereas Van Oyen and Blondeaux (2009) investigated sorting effects, a more simplified turbulence model was adopted, constant eddy viscosity as an alternative to spatially and temporally varying eddy viscosity (Blondeaux and Vittori, 2005a,b; Besio et al., 2006; Borsje et al., 2013). These simplifications of course have their effect on the quantitative results, but they yield a more idealized setting which enables a systematic analysis of the processes of interest.

In order to obtain the best possible quantitative sand wave model one would need to include each process with the most accurate model description, termed 'complex models'. However, to understand important mechanisms a simplified version of such model, i.e. an 'idealized model', is much more insightful. This indicates that idealized models and complex models should not compete, but rather supplement each other. Idealized models are used to understand mechanisms and to explore new processes, while complex models are used to improve insights in sand wave dynamics quantitatively or in a more site-specific setting.

Sand waves are predominantly rhythmic features in one spatial direction with their crests orthogonal to the direction of the tidal flow. However, along-crest variations exist which indicates that 3D flow patterns may have their effect on sand wave dynamics. In the linear stability analysis, in Chapters 2 and 3, 3D effects were included. In the nonlinear sand wave model in Chapter 4, we restricted to a 2DV approach due to computational limitations. Because finite-amplitude along-crest variations could affect sand wave dynamics, a 3D nonlinear sand wave model might give insight in these effects. Blondeaux and Vittori (2009) carried out a weakly nonlinear analysis for which they find that 3D topographies similar to observed sand wave fields are formed particularly for nearly circular tidal currents. Moreover, sand waves seem to be well described in a 2DV model setting, but to understand the finite-amplitude behavior of e.g. bifurcations a 3D approach is required.

In Chapters 2 and 4 two sand wave models have been developed. The first model is linearized for small-amplitude bed perturbations and neglects higher-order terms. This allows to exploit the linear superposition principle meaning that harmonic perturbations can be analyzed. Horizontal spatial structures can be described by Fourier components, reducing the three-dimensional system of partial differential equations that describe the flow problem into a one-dimensional system of ordinary differential equations. Similarly the harmonic temporal structure of the tidal flow is treated with a spectral method, including various harmonic frequencies that are generated by the nonlinear advection term. In the second model – the nonlinear model – the spatial structure of the flow is discretized using a finite-difference method, and the temporal structure is threated with numerical integration, using Forward Euler. Van den Berg (2007) (published in Van den Berg et al., 2012) developed a nonlinear sand wave model, based on finite differences in space, and a spectral method in time. In this work the harmonics of the tidal flow, and higher harmonics were truncated, which could affect the nonlinearity of the flow pattern. The method by Van den Berg et al.

(2012) does seem to be computationally faster and allows to solve the 3D flow pattern, which can simulate nonlinear 3D sand wave dynamics. However, this does not include higher harmonics, which were taken into account in our model. Higher harmonics have velocity amplitudes no larger than 15% of that of the principal component, which – through a nonlinear transport formula – can significantly affect the sediment flux.

5.1.3 Dynamics of ultra long wavelengths

The linear stability model, in Chapters 2 and 3, shows that the fastest growing mode has a wavelength close to that of typical sand waves observed in the field. In the linear regime the fastest growing mode is the dominant mode of the system. The nonlinear model results, in Chapter 4, show that indeed the fastest growing mode dominates the initial small-amplitude dynamics. However, for larger amplitudes nonlinear effects start to play a role causing the dominant wavelength in the domain becomes longer than the linearly predicted fastest growing mode. Of course, finite amplitude sand waves may have a different preferred wavelength compared to the initial fastest growing mode. However, on ultra long timescales the wavelength keeps increasing until it is equal to the domain length. This is probably a model artifact, as the domain length should not have any physical meaning. This suggests that some physical processes are missing that avoid sand waves to become longer and longer. As a way to deal with this problem we also performed simulations on a periodic domain with the wavelength determined by linear stability analysis, which restricted us from investigating nonlinear wavelength effects. The fundamental underlying problem occurs also in other morphodynamic systems, e.g. tidal sand banks (Roos and Hulscher, 2006) and river dunes (Paarlberg et al., 2009). Processes that might lead to a finite wavelength are still missing. Below directions are suggested in which a solution to this problem could be found:

- In formulating the sand wave model, assumptions based on observed sand wave length scales of the order of 100 - 1000 m are made, such as horizontal uniform tidal forcing ('local' model). On the length-scale of ultra long sand waves the tidal wave shows horizontal variation, which might lead to a mechanism damping these long waves. The length scale at which the tidal wave varies is long (order of hundreds of kilometers), but could be relevant.

- The sand wave models formulated in this work use periodic boundary conditions, that represent an infinite model domain. In reality of course other, larger-scale bed features and coastlines restrict the model domain, which might interact with the large wavelengths.

- As the slope effect becomes negligible at very large wavelengths, the solution to this problem should be somehow found in the absence, or reversal of the formation process found in tidally averaged circulation cells.

- The rate at which the wavelength increases in the presented nonlinear sand wave model slows down as the wavelength increases. Potentially sand waves indeed

keep increasing their wavelength at an ever slower pace. At ultra long timescales other processes in shallow seas take place such as sea level rise.

- One mechanism that gives rise to a negative growth rate for ultra long bed forms may be found by modeling turbulence using a k-ε model instead of a constant eddy viscosity in combination with including suspended load sediment transport (Borsje et al., 2014). This shows to be a promising direction for future research to explain this mechanism that is introduced by refining the physical processes in the model.

- For river dunes, Warmink et al. (2014) modeled the splitting mechanism by artificially introducing small new dunes on the stoss side of dunes in a parameterized way. A similar parameterized sand wave splitting mechanism may result in quantitatively improved results.

5.1.4 Bed forms in co-existence

Sand waves are rarely observed as the only seabed features. Often they are superimposed onto larger-scale sand banks. Deleu et al. (2004) presented a detailed overview of the variety of bed forms that co-exist on the Westhinder Bank (Southern North Sea). Conversely, smaller-scale mega ripples are often found superimposed onto sand waves (Terwindt, 1971; Van Dijk and Kleinhans, 2005). The interaction among bed forms in coexistence has been studied by e.g. Komarova and Newell (2000), who explained sand banks emerging from nonlinear sand wave - sand wave interaction. Yet, this interaction is not fully understood, and its modeling requires models to allow both morphological features to fit inside the domain. And to investigate two-way coupling mechanisms the formation of both morphological features needs to be properly included. The widely accepted formation process of sand banks is due to horizontal circulation cells (Huthnance, 1982), whereas the formation of sand waves is due to vertical circulation (Hulscher, 1996). The interaction of sand waves with sand banks thus requires a 3D modeling approach.

5.1.5 Wider use of the nonlinear sand wave model

The nonlinear sand wave model developed in Chapter 4 was shown to enable the investigation of finite-amplitude sand wave dynamics. The model was used to investigate the influence of waves and wind on finite-amplitude sand wave dynamics, but other processes and other settings can be investigated as well. Within the presented work, the forcing of the tidal motion has always been symmetrical, but the model is well capable to also force higher harmonics and a residual current, i.e. the flow over a flat bed ('basic flow'). The model might be usable in a river context if the oscillating tidal motion is switched off, a residual current is introduced and the water depth is adjusted. For river dunes the avalanching process and flow separation would have to be included.

Within sand wave context human interventions could be simulated by e.g. looking at sand wave recovery after dredging. For the equilibrium sand wave profile obtained

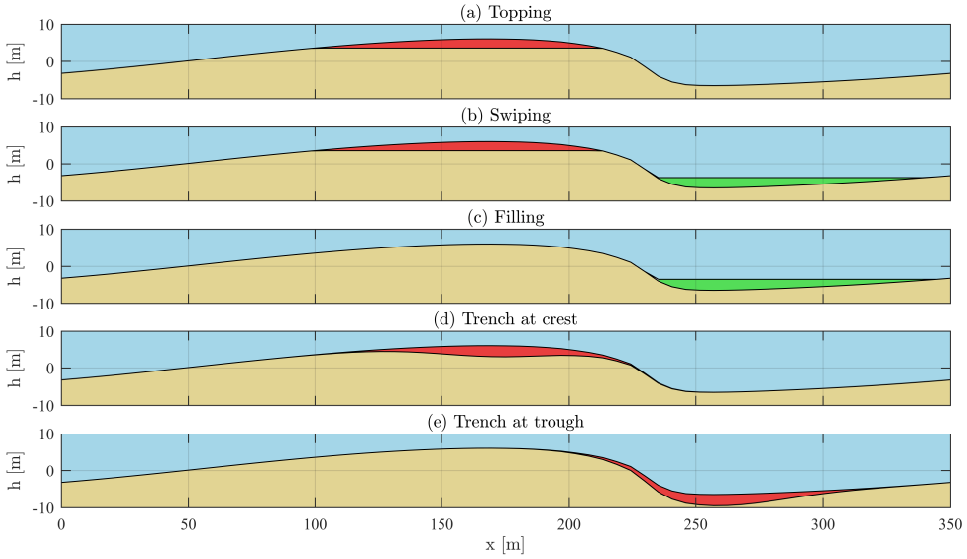

Figure 5.1: The equilibrium sand wave profile, with various dredging interventions: (a) removing the sand from the crest and extract from the system, (b) removing the sand from the crest and place it in the trough, (c) supplement sand into the trough, (d) removing a Gaussian shaped trench from the crest and (e) removing a Gaussian shaped trench from the trough. The colors red indicate removal of sand, green supplementing sand.

in simulations that are shown in Figure 4.6, the effect of possible dredging interventions, shown in Figure 5.1, can be analyzed. Figure 5.2 shows an example of a dredged sand wave and its morphodynamic response. Also different dredging strategies in time can be compared, e.g. frequently dredging small amounts versus larger amounts less frequently.

5.2 Conclusions

The objective of this thesis (Section 1.4) is to investigate the effect of storm-related processes on sand wave dynamics. To investigate these effects we firstly investigated the sand wave dynamics in the stage of formation using linear stability analysis. Once insights had been obtained in the small-amplitude regime, we investigated the effect on finite-amplitude sand wave dynamics by developing a fully non-linear sand wave model. In this section we answer the research questions formulated in Section 1.5.

Q1. What is the effect of storm processes on small-amplitude sand waves?

In Chapter 2, a new linear stability model was developed to systematically analyze the effects of wind waves and wind-driven flow on small-amplitude sand wave dynamics. It was found that wind waves decrease the growth rate significantly, in particular when they propagate parallel to the sand wave crests.

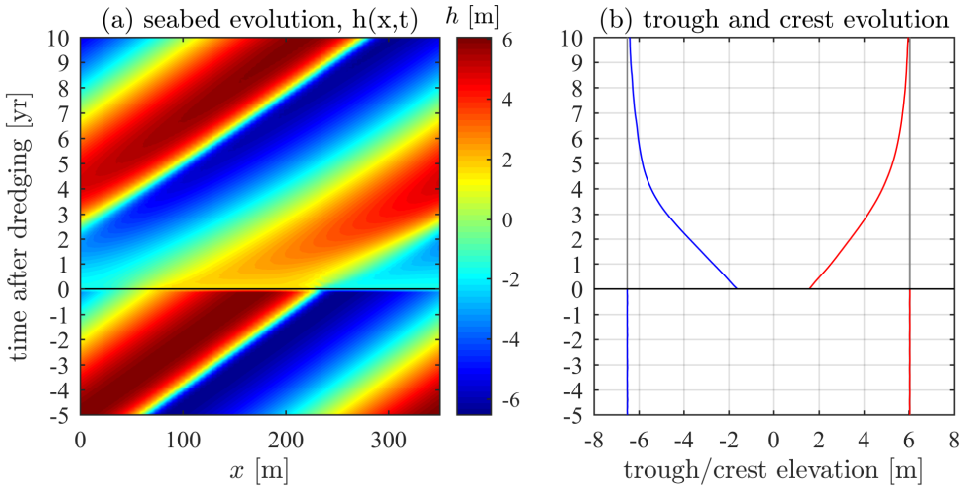

Figure 5.2: (a) The response of a sand wave to a sand conserving dredging intervention at $t = 0$. (b) Evolution in time of trough (blue) and crest (red).

Wind waves increased both the growth mechanism due to the perturbed flow and the decaying mechanism due to slope effects. The decaying mechanism is amplified more effectively, resulting in a net reduction in growth rate. Wind waves (symmetrical in this model) do not induce sand wave migration, but are able to enhance migration due to other mechanisms, such as wind-driven flow, tidal asymmetry, or residual currents. Wind-driven flow can either increase or decrease the growth rate depended on the direction of the wind with respect to the sand wave orientation. In absence of the Coriolis effect wind directed perpendicular to the sand wave crest increases the growth rate and wind parallel to the sand wave crest decreases the growth rate. Wind effects on sand wave dynamics are strongly affected by the Coriolis effect. Firstly, the wind angle at which the maximum growth and migration occurs shifts by including the Coriolis effect. Secondly, the magnitude of the growth and migration effects decrease due to the Coriolis effect. Overall, it is concluded that storms significantly affect sand wave dynamics in their formation stage.

Q2. What is the effect of a site-specific wave and wind climate on sand wave dynamics?

In Chapter 3, the newly developed linear stability model was used in combination with wave and wind measurements to address research question 2. By applying a four dimensional binning procedure, a four dimensional joint probability density function was created for four storm parameters: wind amplitude, wind direction, near-bed wave orbital velocity and wave direction. By applying the linear stability model for each of these combinations of storm parameters settings and multiplying the model results with the probability corresponding

to the storm parameters the effect of various storm conditions was analyzed. The effect of mild, intermediate and extreme storm conditions on sand wave dynamics was analyzed. It was found that mild conditions, although they often occur, hardly affect sand wave dynamics due to the limited effect of mild wave and wind conditions. Intermediate storm conditions have the largest effect on sand wave dynamics since these storm conditions occur regularly while the effect of these conditions on sand wave dynamics is moderate. Although extreme storm conditions hardly occur, they still play a role in sand wave dynamics because their effect is large such that these conditions still contribute. The total wave and wind climate averaged effect on the growth rate is only minor, directly resulting in minor changes in the preferred wavelength and orientation. However, the effect on migration is significant. The dominant south-west wind direction results in a net wave and wind climate averaged migration rate, comparable to typical observed migration rates, to the north-east. Analyzing wave and wind occurrence during summer and winter periods revealed significant seasonal variations in sand wave dynamics. Particularly sand wave migration is larger during winter periods compared to summer. The range of migration rates obtained from wave and wind variations is supported by observational studies, which also find variable migration rates in time.

Q3. What is the effect of storm processes on finite-amplitude sand waves?

In Chapter 4, a new nonlinear sand wave model was developed that is able to simulate sand wave evolution towards a finite-amplitude equilibrium state. Both wind and in particular waves reduce the sand wave equilibrium height. Wind-driven flow causes sand wave migration and horizontal asymmetry of the sand wave profile. Waves and wind combined result in a faster migration rate compared to wind only, while waves alone do not cause migration. Thus wind waves enhance sand wave migration, but do not induce it. The wave angle has only a minor effect on sand wave dynamics, while the direction of wind-driven flow is important for sand wave migration and for horizontal asymmetry. The wave-induced reduction in sand wave height is caused by a faster nonlinear increase in slope effect compared to the nonlinear increase in flow effect. Sand wave migration typically decreases with increasing sand wave height. However, in an irregular sand wave field sand waves with larger crests heights tend to overtake smaller sand waves, which shows complex interactions between neighboring sand waves. Intermittent storm events lead to a dynamic equilibrium, in which sand waves tend to adapt their shape to their equilibrium shape corresponding to the storm condition. However, the adaptation time is much longer than that of a typical storm event. Therefore sand waves, and especially their crests, constantly adapt towards their equilibrium state, but never reach this state. Short storm durations (e.g. 1 week of storm per year) already significantly affect sand wave dynamics.

5.3 Recommendations

We conclude this chapter with the most important recommendations for future research on sand wave research.

Investigate the slope effect of sediment transport on sand wave height. This effect is not as trivial as it may seem. An increasing slope parameter decreases the growth rate, but the preferred wavelength of sand waves increases, as seen from linear stability analysis. Larger wavelength in return results in larger sand wave heights, as shown by the nonlinear sand wave model in Chapter 4. Sand wave height is determined by the nonlinear competition between flow induced transport towards the crest and the downslope effect due to gravity. Only when the growth and the decay mechanisms balance each other an equilibrium state is reached.

Investigate what processes cause sand waves to have a finite wavelength. As pointed out in Section 5.1.3 the processes causing fully grown sand waves to have a finite wavelength remain unclear. To achieve this, physical descriptions may have to be changed to include additional processes or more detailed descriptions of processes that are already included.

Compare modeled storm effects with field data. In Chapter 3 the effect of an actual wave and wind climate on sand wave dynamics was investigated and it was concluded that especially the migration rate is significantly affected. A comparison of the predicted sand wave migration and the actual sand wave migration is still lacking. Comparison with observations may show that wave and wind data can be used as sand wave migration predictor, which would be a valuable result. Chapter 4 shows that sand wave migration reduces with sand wave height, and that sand waves strongly interact with each other. Contrary to small-amplitude (linear) sand wave dynamics in response to storm effects, the sequence in which storms occur does play a role in finite-amplitude (nonlinear) sand wave dynamics. This storm sequence dependency is an interesting topic for future research.

Use the linear sand wave model for engineering applications. The linear sand wave model might, next to the sand wave migration predictor in the previous recommendation, be used for other engineering applications, such as offshore sand mining pits as was done by e.g. Roos and Hulscher (2003). The spatial structures developing from the inherently unstable flat bed can be analyzed for various human seabed interventions.

Use the nonlinear sand wave model for engineering applications. It is interesting to test various practical applications in the nonlinear sand wave model, e.g. sand wave recovery from different dredging interventions. In e.g. the North Sea sand waves are frequently dredged to maintain the least navigable water depth in navigation channels. Insight in sand wave recovery after dredging may lead to more cost efficient maintenance policies.

Using a more refined turbulence model. In this work turbulence is modeled by a constant vertical eddy viscosity in space and time, while in reality turbulent mixing changes both in space and time. For quantitatively improved results one may include a vertical spatial turbulence structure (e.g. Blondeaux and Vittori, 2005a,b; Besio et al., 2006). To simulate turbulent mixing, which is variable in both time and space, a $k - \varepsilon$ model can be used (Borsje et al., 2013).

Including suspended sediment transport. In Chapter 2 the qualitative effect of waves and wind via suspended sediment transport on sand wave formation was investigated. There it was found that waves increase, and wind decreases the growth rate due to suspended load. Borsje et al. (2014) investigated the effect of suspended load in Delft3D, and found that suspension results in a negative growth rate for sand waves. Observations show that in areas where suspended sediment is the dominant transport mode, sand waves are not observed. This may imply that including suspended load does require a more detailed turbulence description. It is therefore recommended to included a refined turbulence model, such as $k - \varepsilon$, to investigate the effect of suspended load on finite-amplitude sand wave dynamics. Suspended sediment may become more important compared to bed load transport during stormy conditions.

Interaction with biology Next to water and sand, there is a whole ecosystem underwater. Various species inhabiting the sea floor are known to affect near-bed hydrodynamics and sand transport, resulting in modified sand wave dynamics (Borsje et al., 2009). Conversely, seabed topography affects biology resulting in a two-way coupling between biology and morphodynamics (Damveld et al., 2017). Better understanding of this coupling may help us improve sand wave modeling.

Along-crest variations In Chapter 4, along-crest uniformity has been assumed as sand waves are predominant rhythmic patterns in one direction. Indeed, the fastest growing mode obtained in Chapter 2 has its crests perpendicular to the tidal current. However, also oblique modes exist with a positive growth rate and observed sand wave fields display along-crest variations. Blondeaux and Vittori (2009) investigated the weakly nonlinear interaction between a triad of harmonic components and found this to cause a three-dimensional seabed pattern similar to observed sand waves. We recommend to further investigate this in the strongly nonlinear regime. This triad interaction was studied earlier by Roos and Blondeaux (2001) for the case of sand ripples. Finally, for tidal sand ridges, models have shown along-crest variations that may be time-dependent (Yuan and de Swart, 2017) or indicative of bank-breaking (van Veelen et al., 2018).

Bibliography

Aliotta, S., Perillo, G.M.E., 1987. A sand wave field in the entrance to Bahía Blanca estuary, Argentina. Marine Geology 76, 1–14.

Barnard, P.L., Hanes, D.M., Rubin, D.M., Kvitek, R.G., 2006. Giant sand waves at the mouth of San Francisco Bay. Eos, Transactions American Geophysical Union 87, 285–289.

Van den Berg, J., 2007. Non-linear sand wave evolution. PhD-Thesis. University of Twente.

Van den Berg, J., Sterlini, F., Hulscher, S.J.M.H., Van Damme, R.M.J., 2012. Non-linear process based modelling of offshore sand waves. Continental Shelf Research 37, 26–35.

Besio, G., Blondeaux, P., Brocchini, M., Hulscher, S.J.M.H., Idier, D., Knaapen, M.A.F., Németh, A.A., Roos, P.C., Vittori, G., 2008. The morphodynamics of tidal sand waves: a model overview. Coastal Engineering 55, 657–670.

Besio, G., Blondeaux, P., Brocchini, M., Vittori, G., 2004. On the modeling of sand wave migration. Journal of Geophysical Research: Oceans (1978–2012) 109.

Besio, G., Blondeaux, P., Frisina, P., 2003. A note on tidally generated sand waves. Journal of Fluid Mechanics 485, 171–190.

Besio, G., Blondeaux, P., Vittori, G., 2006. On the formation of sand waves and sand banks. Journal of Fluid Mechanics 557, 1–27.

Blondeaux, P., 1990. Sand ripples under sea waves part 1. ripple formation. Journal of Fluid Mechanics 218, 1–17.

Blondeaux, P., Vittori, G., 2005a. Flow and sediment transport induced by tide propagation: 1. the flat bottom case. Journal of Geophysical Research: Oceans (1978–2012) 110.

Blondeaux, P., Vittori, G., 2005b. Flow and sediment transport induced by tide propagation: 2. the wavy bottom case. Journal of Geophysical Research: Oceans (1978–2012) 110.

Blondeaux, P., Vittori, G., 2009. Three-dimensional tidal sand waves. Journal of Fluid Mechanics 618, 1–11.

Blondeaux, P., Vittori, G., 2016. A model to predict the migration of sand waves in shallow tidal seas. Continental Shelf Research 112, 31–45.

Blondeaux, P., Vittori, G., Mazzuoli, M., 2016. Pattern formation in a thin layer of sediment. Marine Geology 376, 39–50.

Bokuniewicz, H.J., Gordon, R.B., Kastens, K.A., 1977. Form and migration of sand waves in a large estuary, Long Island Sound. Marine Geology 24, 185–199.

Borsje, B.W., Kranenburg, W.M., Roos, P.C., Matthieu, J., Hulscher, S.J.M.H., 2014. The role of suspended load transport in the occurrence of tidal sand waves. Journal of Geophysical Research: Earth Surface 119, 701–716.

Borsje, B.W., Roos, P.C., Kranenburg, W.M., Hulscher, S.J.M.H., 2013. Modeling tidal sand wave formation in a numerical shallow water model: The role of turbulence formulation. Continental Shelf Research 60, 17–27.

Borsje, B.W., de Vries, M.B., Bouma, T.J., Besio, G., Hulscher, S.J.M.H., Herman, P.M.J., 2009. Modeling bio-geomorphological influences for offshore sandwaves. Continental Shelf Research 29, 1289–1301.

Bowden, K.F., Fairbairn, L.A., Hughes, P., 1959. The distribution of shearing stresses in a tidal current. Geophysical Journal International 2, 288–305.

Buijsman, M.C., Ridderinkhof, H., 2008. Long-term evolution of sand waves in the Marsdiep inlet. i: High-resolution observations. Continental Shelf Research 28, 1190–1201.

Campmans, G.H.P., Roos, P.C., De Vriend, H.J., Hulscher, S.J.M.H., 2017. Modeling the influence of storms on sand wave formation: A linear stability approach. Continental Shelf Research 137, 103–116.

Campmans, G.H.P., Roos, P.C., De Vriend, H.J., Hulscher, S.J.M.H., 2018. The influence of storms on sand wave evolution: a nonlinear idealized modeling approach. Journal of Geophysical Research: Earth Surface .

Damen, J.M., Van Dijk, T.A.G.P., Hulscher, S.J.M.H., 2018. Spatially varying environmental properties controlling observed sand wave morphology. Journal of Geophysical Research: Earth Surface 123, 262–280.

Damveld, J.H., Roos, P.C., Borsje, B.W., Hulscher, S.J.M.H., 2017. Exploring the two-way coupling between sand wave dynamics and benthic species: an idealised modelling approach. 4th International Symposium on Shallow Flows, Eindhoven, Netherlands. .

Deleu, S., Lancker, V.V., den Eynde, D.V., Moerkerke, G., 2004. Morphodynamic evolution of the kink of an offshore tidal sandbank: the westhinder bank (southern north sea). Continental Shelf Research 24, 1587 – 1610.

Dodd, N., Blondeaux, P., Calvete, D., De Swart, H.E., Falqués, A., Hulscher, S.J.M.H., Różyński, G., Vittori, G., 2003. Understanding coastal morphodynamics using stability methods. Journal of Coastal Research , 849–865.

Dorst, L.L., Roos, P.C., Hulscher, S.J.M.H., 2011. Spatial differences in sand wave dynamics between the Amsterdam and the Rotterdam region in the Southern North Sea. Continental Shelf Research 31, 1096–1105.

Dorst, L.L., Roos, P.C., Hulscher, S.J.M.H., 2013. Improving a bathymetric resurvey policy with observed sea floor dynamics. Journal of applied geodesy 7, 51–64.

Dorst, L.L., Roos, P.C., Hulscher, S.J.M.H., Lindenbergh, R.C., 2009. The estimation of sea floor dynamics from bathymetric surveys of a sand wave area. Journal of Applied Geodesy 3, 97–120.

Ernstsen, V.B., Lefebvre, A., Bartholdy, J., Bartholomä, A., Winter, C., 2011. Spatiotemporal height variations of large-scale bedforms in the grådyb tidal inlet channel (denmark): a case study on coastal system impact. Journal of Coastal Research , 746.

Fenster, M.S., Fitzgerald, D.M., Bohlen, W.F., Lewis, R.S., Baldwin, C.T., 1990. Stability of giant sand waves in eastern Long Island Sound, USA. Marine Geology 91, 207–225.

Ferret, Y., Le Bot, S., Tessier, B., Garlan, T., Lafite, R., 2010. Migration and internal architecture of marine dunes in the eastern english channel over 14 and 56 year intervals: the influence of tides and decennial storms. Earth Surface Processes and Landforms 35, 1480–1493.

Garnier, R., Calvete, D., Falqués, A., Caballeria, M., 2006. Generation and nonlinear evolution of shore-oblique/transverse sand bars. Journal of Fluid Mechanics 567, 327–360.

Gerkema, T., 2000. A linear stability analysis of tidally generated sand waves. Journal of Fluid Mechanics 417, 303–322.

Gräwe, U., Burchard, H., Müller, M., Schuttelaars, H.M., 2014. Seasonal variability in M2 and M4 tidal constituents and its implications for the coastal residual sediment transport. Geophysical Research Letters 41, 5563–5570.

Harris, P.T., 1989. Sandwave movement under tidal and wind-driven currents in a shallow marine environment: Adolphus Channel, northeastern Australia. Continental Shelf Research 9, 981–1002.

Harvey, J.G., 1966. Large sand waves in the irish sea. Marine Geology 4, 49–55.

Hommes, S., Hulscher, S.J.M.H., Stolk, A., 2007. Parallel modeling approach to assess morphological impacts of offshore sand extraction. Journal of coastal research 23, 1565–1579.

Houthuys, R., Trentesaux, A., De Wolf, P., 1994. Storm influences on a tidal sandbank's surface (Middelkerke Bank, southern North Sea). Marine Geology 121, 23–41.

Hulscher, S.J.M.H., 1996. Tidal-induced large-scale regular bed form patterns in a three-dimensional shallow water model. Journal of Geophysical Research: Oceans (1978–2012) 101, 20727–20744.

Hulscher, S.J.M.H., Van den Brink, G.M., 2001. Comparison between predicted and observed sand waves and sand banks in the North Sea. Journal of Geophysical Research: Oceans (1978–2012) 106, 9327–9338.

Huthnance, J.M., 1982. On one mechanism forming linear sand banks. Estuarine, Coastal and Shelf Science 14, 79–99.

Idier, D., Ehrhold, A., Garlan, T., 2002. Morphodynamics of an undersea sandwave of the Dover Straits. Comptes Rendus Geoscience 334, 1079–1085.

Jones, N.S., Kain, J.M., Stride, A.H., 1965. The movement of sand waves on Warts Bank, Isle of Man. Marine Geology 3, 329–336.

Katoh, K., Kume, H., Kuroki, K., Hasegawa, J., 1998. The development of sand waves and the maintenance of navigation channels in the Bisanseto Sea. Coastal Engineering Proceedings 1.

Knaapen, M.A.F., 2005. Sandwave migration predictor based on shape information. Journal of Geophysical Research: Earth Surface (2003–2012) 110.

Knaapen, M.A.F., Hulscher, S.J.M.H., 2002. Regeneration of sand waves after dredging. Coastal Engineering 46, 277–289.

Knaapen, M.A.F., Willis, J., Harris, J.H., 2013. Modeling dune dynamics in situations with bimodal sediment distributions. MARID IV , 153–158.

KNMI, n.d. www.knmi.nl.

Komarova, N.L., Newell, A.C., 2000. Nonlinear dynamics of sand banks and sand waves. Journal of Fluid Mechanics 415, 285–321.

Krewinkel, B.C., Straatsma, L., Dusseljee, D., Borsje, B.W., Hulscher, S.J.M.H., 2017. Sand wave migration reversal due to severe wind events. NCK days, Den Helder, Netherlands. , 81–81.

Lanckneus, J., De Moor, G., 1991. Present-day evolution of sandwaves on a sandy shelf bank. Oceanologica Acta 14, 123–123.

Langhorne, D.N., 1982. A study of the dynamics of a marine sandwave. Sedimentology 29, 571–594.

Le Bot, S., Trentesaux, A., Garlan, T., Berne, S., Chamley, H., 2000. Influence des tempêtes sur la mobilité des dunes tidales dans le détroit du Pas-de-Calais. Oceanologica Acta 23, 129–141.

Lesser, G.R., Roelvink, J.A., Van Kester, J.A.T.M., Stelling, G.S., 2004. Development and validation of a three-dimensional morphological model. Coastal engineering 51, 883–915.

Ludwick, J.C., 1971. Migration of tidal sand waves in Chesapeake Bay entrance. Technical Report. DTIC Document.

Maas, L.R.M., Van Haren, J.J.M., 1987. Observations on the vertical structure of tidal and inertial currents in the central north sea. Journal of Marine Research 45, 293–318.

Makin, V.K., Kudryavtsev, V.N., Mastenbroek, C., 1995. Drag of the sea surface. Boundary-Layer Meteorology 73, 159–182.

McCave, I.N., 1971. Sand waves in the North Sea off the coast of Holland. Marine Geology 10, 199–225.

Van de Meene, J.W.H., Boersma, J.R., Terwindt, J.H.J., 1996. Sedimentary structures of combined flow deposits from the shoreface-connected ridges along the central Dutch coast. Marine Geology 131, 151–175.

Mei, C.C., 1989. The applied dynamics of ocean surface waves. volume 2. World Scientific Publishing Co. Pte. Ltd.

Menninga, P.J., 2012. Analysis of variations in characteristics of sand waves observed in the Dutch coastal zone: a field and model study. (Master Thesis), Utrecht University (NL) .

Németh, A., Hulscher, S.J.M.H., De Vriend, H.J., 2003. Offshore sand wave dynamics, engineering problems and future solutions. Pipeline and gas journal 230, 67–69.

Németh, A.A., Hulscher, S.J.M.H., De Vriend, H.J., 2002. Modelling sand wave migration in shallow shelf seas. Continental Shelf Research 22, 2795–2806.

Németh, A.A., Hulscher, S.J.M.H., Van Damme, R.M.J., 2007. Modelling offshore sand wave evolution. Continental Shelf Research 27, 713–728.

Nielsen, P., 1992. Coastal bottom boundary layers and sediment transport. volume 4. World Scientific.

Paarlberg, A.J., Dohmen-Janssen, C.M., Hulscher, S.J., Termes, P., 2009. Modeling river dune evolution using a parameterization of flow separation. Journal of Geophysical Research: Earth Surface 114.

Passchier, S., Kleinhans, M.G., 2005. Observations of sand waves, megaripples, and hummocks in the dutch coastal area and their relation to currents and combined flow conditions. Journal of Geophysical Research: Earth Surface (2003–2012) 110.

Rijkswaterstaat, n.d. live.waterbase.nl.

Roe, P.L., 1986. Characteristic-based schemes for the Euler equations. Annual review of fluid mechanics 18, 337–365.

Roos, P.C., Blondeaux, P., 2001. Sand ripples under sea waves. part 4. tile ripple formation. Journal of fluid mechanics 447, 227–246.

Roos, P.C., Hulscher, S.J.M.H., 2003. Large-scale seabed dynamics in offshore morphology: Modeling human intervention. Reviews of geophysics 41.

Roos, P.C., Hulscher, S.J.M.H., 2006. Nonlinear modeling of tidal sandbanks: wavelength evolution and sand extraction, in: Coastal Engineering 2006: (In 5 Volumes). World Scientific, pp. 2761–2771.

Roos, P.C., Hulscher, S.J.M.H., Van der Meer, F., Van Dijk, T.A.G.P., Wientjes, I.G.M., Van den Berg, J., 2007. Grain size sorting over offshore sandwaves: Observations and modelling .

Santoro, V.C., Amore, E., Cavallaro, L., De Lauro, M., 2004. Evolution of sand waves in the Messina Strait, Italy. Ocean Dynamics 54, 392–398.

Soulsby, R.L., Hamm, L., Klopman, G., Myrhaug, D., Simons, R.R., Thomas, G.P., 1993. Wave-current interaction within and outside the bottom boundary layer. Coastal Engineering 21, 41–69.

Sterlini, F., Hulscher, S.J.M.H., Hanes, D.M., 2009. Simulating and understanding sand wave variation: A case study of the golden gate sand waves. Journal of Geophysical Research: Earth Surface 114.

Sterlini, F.M., 2009. Modelling Sand Wave Variation. University of Twente.

Terwindt, J.H.J., 1971. Sand waves in the Southern Bight of the North Sea. Marine Geology 10, 51–67.

Tonnon, P.K., Van Rijn, L.C., Walstra, D.J.R., 2007. The morphodynamic modelling of tidal sand waves on the shoreface. Coastal Engineering 54, 279–296.

Trowbridge, J.H., 1995. A mechanism for the formation and maintenance of shore-oblique sand ridges on storm-dominated shelves. Journal of Geophysical Research: Oceans 100, 16071–16086.

Van Dijk, T.A.G.P., Kleinhans, M.G., 2005. Processes controlling the dynamics of compound sand waves in the North Sea, Netherlands. Journal of Geophysical Research: Earth Surface (2003–2012) 110.

Van Gerwen, W., Borsje, B.W., Damveld, J.H., Hulscher, S.J.M.H., 2018. Modelling the effect of suspended load transport and tidal asymmetry on the equilibrium tidal sand wave height. Coastal Engineering 136, 56 – 64.

Van Leer, B., 1979. Towards the ultimate conservative difference scheme. v. a second-order sequel to godunovs method. Journal of Computational Physics 32, 101–136.

Van Oyen, T., Blondeaux, P., 2009. Grain sorting effects on the formation of tidal sand waves. Journal of Fluid Mechanics 629, 311–342.

Van Rijn, L.C., 1990. Principles of fluid flow and surface waves in rivers, estuaries, seas and oceans. volume 11. Aqua Publications Amsterdam, The Netherlands.

Van Rijn, L.C., 1993. Principles of sediment transport in rivers, estuaries and coastal seas. volume 1006. Aqua publications Amsterdam.

Van Rijn, L.C., 2007. Unified view of sediment transport by currents and waves. ii: Suspended transport. Journal of Hydraulic Engineering 133, 668–689.

Van Santen, R.B., De Swart, H.E., Van Dijk, T.A.G.P., 2011. Sensitivity of tidal sand wavelength to environmental parameters: A combined data analysis and modelling approach. Continental Shelf Research 31, 966–978.

van Veelen, T.J., Roos, P.C., Hulscher, S.J., 2018. Process-based modelling of bank-breaking mechanisms of tidal sandbanks. Continental Shelf Research .

Van der Veen, H.H., Hulscher, S.J.M.H., Knaapen, M.A.F., 2006. Grain size dependency in the occurrence of sand waves. Ocean Dynamics 56, 228–234.

Warmink, J.J., Dohmen-Janssen, C.M., Lansink, J., Naqshband, S., Duin, O.J., Paarlberg, A.J., Termes, P., Hulscher, S.J., 2014. Understanding river dune splitting through flume experiments and analysis of a dune evolution model. Earth surface processes and landforms 39, 1208–1220.

Weisse, R., Günther, H., 2007. Wave climate and long-term changes for the southern north sea obtained from a high-resolution hindcast 1958–2002. Ocean Dynamics 57, 161–172.

Yuan, B., de Swart, H.E., 2017. Effect of sea level rise and tidal current variation on the long-term evolution of offshore tidal sand ridges. Marine Geology 390, 199 – 213.

Zhou, J.Q., Roos, P.C., Wu, Z.Y., Campmans, G.H.P., Hulscher, S.J.M.H., 2018. Modelling sand wave fields on the Taiwan banks, Northern South China sea: The formation of two-scale sand waves in different periods, in: NCK-Days 2018.

About the author

Geert Campmans was born in Roosendaal, the Netherlands on the 21st of August, 1989. He grew up in Borne, and went to secondary school in Hengelo at the Grundel Lyceum in 2002. In 2008, he started his BSc in Mechanical Engineering. During his Bachelor degree, he was particularly interested in fluid dynamics. Therefore, Geert enrolled in the Engineering Fluid Dynamics group for his MSc Mechanical Engineering in 2011. During his internship he validated a newly developed dense-gas model in a computation fluid dynamics code Eilmer3 at University of Queensland, Brisbane – Australia. His MSc graduation project was an exploratory study of multigrid techniques for hyperbolic systems of equations. Geert received his MSc degree in December 2013.

In March 2014 Geert started his PhD in the Water Engineering and Management group, in the Civil Engineering department. During his PhD he spent two months in the group of Nonlinear Fluid Dynamics at Universitat Politècnica de Catalunya, in Barcelona, where he further improved his nonlinear sand wave model. He supervised two BSc and two MSc graduation projects and supervised tutorials at both BSc and MSc level. At international conferences in Caernarfon, Scheveningen, Eindhoven and Shanghai he presented his research. After finishing his thesis in March 2018 he started working as a PostDoc in the same SMARTSEA project, continuing sand wave research on human interventions such as dredging activities for e.g. navigation channel maintenance and pipeline and cable burial.

Publications

Peer-reviewed journal papers

Campmans, G.H.P., Roos, P.C., De Vriend, H.J., Hulscher, S.J.M.H., 2017. Modeling the influence of storms on sand wave formation: A linear stability approach. *Continental Shelf Research* 137, 103-116. DOI: 10.1016/j.csr.2017.02.002

Campmans, G.H.P., Roos, P.C., Schrijen, E.P.W.J., Hulscher, S.J.M.H. (subm.). Modeling wave and wind climate effects on tidal sand wave dynamics: A North Sea case study

Campmans, G.H.P., Roos, P.C., De Vriend, H.J., Hulscher, S.J.M.H. (2018). The influence of storms on sand wave evolution: a nonlinear idealized modeling approach *Journal of Geophysical Research - Earth Surface*

Roos, P.C., Pitzalis, C., Reef, K.R.G., Lipari, G., **Campmans, G.H.P.**, Hulscher, S.J.M.H. (subm.). Time-dependent linearisation of bottom friction for storm surge modelling

Zhou, Q.J., Roos, P.C., Wu, Z.Y., **Campmans, G.H.P.**, Hulscher, S.J.M.H. (in progress). Modelling sand wave fields on the Taiwan Banks, northern South China Sea: the formation of two-scale sand waves in different periods

Conference papers

Campmans, G.H.P., Roos, P.C., Hulscher, S.J.M.H. (2016). The influence of storms on sand wave dynamics: morphodynamic modeling using a linear stability approach. 18-18. Abstract from NCK-days 2016, Ouddorp, Netherlands.

Campmans, G.H.P., Roos, P.C., Hulscher, S.J.M.H. (2016). Modelling the influence of storm-related processes on sand wave dynamics; a linear stability approach. 25-28. Abstract from Marine and River Dune Dynamics, MARID V, Wales, UK.

Campmans, G.H.P., Roos, P.C., De Vriend, H.J., Hulscher, S.J.M.H. (2016). The influence of storms on sand wave dynamics: from linear to nonlinear modelling. 10-10. Paper presented at 18th Physics of Estuaries and Coastal Seas Conference, PECS 2016, Scheveningen, Netherlands.

Overbeek, S.G., **Campmans, G.H.P.**, Roos, P.C., Hulscher, S.J.M.H. (2016). Influence of a sand wave field on wind wave propagation: A North Sea study. 17-17. Paper presented at 18th Physics of Estuaries and Coastal Seas Conference, PECS 2016, Scheveningen, Netherlands.

Campmans, G.H.P., Roos, P.C., De Vriend, H.J., Hulscher, S.J.M.H. (2017). The

influence of storms on finite amplitude sand wave dynamics: an idealized nonlinear model. 1-3. Abstract from 4th International Symposium on Shallow Flows, ISSF 2017, Eindhoven, Netherlands.

Campmans, G.H.P., Roos, P.C., Bijker, R., Hulscher, S.J.M.H. (2017). Nonlinear modeling of tidal sand waves: Application to a pipeline location in the North Sea. 33-33. Abstract from ECSA Focus Meeting 2017, Shanghai, China.

Roos, P.C., **Campmans, G.H.P.**, & Hulscher, S.J.M.H. (2017). The influence of wave and wind climate on sand wave dynamics: A North Sea case study with a linear stability model. 86-86. Abstract from ECSA Focus Meeting 2017, Shanghai, China.

Zhou, J.Q., Roos, P.C., Wu, Z.Y., **Campmans, G.H.P.**, Hulscher, S.J.M.H. (2018). Modelling sand wave fields on the Taiwan Banks, northern South China Sea: The formation of two-scale sand waves in different periods. Abstract from NCK-days 2018, Haarlem, Netherlands

Oral conference contributions without abstract

Campmans, G.H.P., Modelling the influence of storm-related processes on sand wave dynamics: a linear stability approach. J.M. Burgers Symposium 2016, Lunteren, Netherlands.

Campmans, G.H.P., Modelling the influence of storm effects on finite amplitude sand wave dynamics. J.M. Burgers Symposium 2017, Lunteren, Netherlands.

Campmans, G.H.P., Modeling tidal sand wave recovery after dredging. J.M. Burgers Symposium 2018, Lunteren, Netherlands.